EXPLORATION OF THE TWO-ELECTRON CONTINUUM PROBLEM USING R-MATRIX METHODS

by

KURT WAYNE MEYER

B. S., University of Nebraska, 1988

M. S., George Washington University, 1991

M. S., University of Colorado, 1994

A thesis submitted to the

Faculty of the Graduate School of the

University of Colorado in partial fulfillment

of the requirements for the degree of

Doctor of Philosophy

Department of Physics

1997

This thesis for the Doctor of Philosophy degree by

Kurt Wayne Meyer

has been approved for the

Department of

Physics

by

Chris H. Greene

John Cooper

Date _____

The final copy of this thesis has been examined by the signators, and we find that both the content and the form meet acceptable presentation standards of scholarly work in the above mentioned discipline.

Meyer, Kurt Wayne (Ph. D., Physics)

Exploration of the Two-electron Continuum Problem Using R-Matrix Methods

Thesis directed by Professor Chris H. Greene

If we ever hope to describe complicated physical systems in nature, it is imperative to first understand much simpler systems. In this work, we explore the fundamental problem of two electron escape processes, which is itself a particular case of the more general three-body problem in nonrelativistic quantum mechanics. A large body of experimental and theoretical work performed in the last 80 years provides strong evidence that this theory adequately describes most processes in atomic systems. Our study is also important in the sense that the equation which describes our system of three particles is one of the simplest nonseparable partial differential equations in quantum physics. For any n-particle system (with $n \geq 3$) interacting through position or velocity dependent forces (including classical systems), a nonseparable partial differential equation is required to describe the system and allow for exchange of energy and momentum between the particles.

In this work, we adopt a method (the eigenchannel R-matrix method) with a proven capability to accurately describe single electron escape. We make a major extension of this method to treat escape of two electrons here. We focus on the process of double photoejection of helium and H^-. A single photon is absorbed by the target, transferring enough energy for both electrons to escape. However, one observes that single electron escape occurs most of the time, while double electron escape happens much less frequently. Since the interaction of the electromagnetic field with the atom is described by a single particle operator, double electron escape can only occur due to interactions between the two electrons. One of the major goals of this work is a deeper understanding of the role of interactions between the two electrons in the resulting single or double escape process.

Our initial calculations of helium double photoionization cross sections were in fair agreement with then existing experimental values. However, these calculations also exhibited

an internal inconsistency caused by inaccurate wavefunctions that were used to describe the initial and final states of our system. A subsequent application of the eigenchannel R-matrix approach to a simplified model of electron-hydrogen (and electron-He^+) scattering nevertheless indicated that this method could describe two electron escape processes accurately. To overcome the inconsistency in our original calculations of helium double photoionization, we next implemented the eigenchannel R-matrix method using a finite element basis set. Application of this approach to two electron photoejection in helium and H^- reduced the internal inconsistency by more than an order of magnitude. The newest helium calculations are in good agreement with the most recent theoretical and experimental studies. Furthermore, calculations of partial cross sections for the single escape processes $h\nu$ + He $\rightarrow$ $He^+(n)$ + e^- agree with recent experimental values for $n = 2 - 6$.

DEDICATION

Not in the victory, but the action:

not the goal but the game:

in the deed the glory.

-Hartley Burr Alexander

I would like to dedicate this work to all of the men and women of the past and present who have endured and continue to endure hardships, and who have made and continue to make sacrifices for the sake of creating a better world for the rest of us.

ACKNOWLEDGEMENTS

I would like to acknowledge the National Science Foundation for supporting this research, and also the National Center for Supercomputer Applications for use of their computer resources.

On a more personal note, I would like to acknowledge all those who have had a positive influence on my life. This includes the many classmates and teachers with whom I have had contact over the past 26 years of my formal education. I would also like to thank my current advisor Chris Greene and past advisors for giving me the opportunity to work on interesting problems and the chance to develop my skills and abilities. In addition, I acknowledge several members in the atomic physics community with whom I have had the pleasure of working, especially Igor Bray, James Samson, and Janine Shertzer.

Some of my most productive collaborations have come from within the group. I gratefully acknowledge the support of the group over the years, including postdocs Francis Robicheaux, Jeff Stephens, Gregory Miecznik, John Bohn, and Hugo van der Hart, and fellow graduate students Bob Wood, William Clark, Brett Esry, Jim Burke, and Brian Granger. I would also like to thank Chela Kunasz and Anne Hammond for providing computer support and helping me out on many occasions.

Throughout my life I have been blessed with the support and encouragement of a vast network of aunts and uncles and roughly 80 cousins. I would like to especially mention the more immediate members of my family, including my brothers Jeff and Kevin and sister-in-law Madeline, who have provided me with much helpful advice, encouragement, comraderie, and fun over the years, and my nieces Marie and Megan, and nephew Michael who have been constant reminders of the joys of life. Finally, I would like to thank my

parents for providing my daily source of inspiration. For the often difficult learning experiences on the farm to their constant examples of professionalism, dedication, compassion, and charity, I would like to especially thank my parents for teaching me the most important lessons of life.

CONTENTS

FIGURES

FIGURE

TABLES

TABLE

CHAPTER 1

INTRODUCTION

In this work, we attempt to describe a special case of the three-body problem in the context of nonrelativistic quantum mechanics. The general three-body problem remains one of the longstanding unsolved problems in physics. The n-body problem was first outlined precisely by Newton [1]: For n particles (point masses), each of known mass interacting with each other only through a gravitational force, given the positions and velocities of the particles at any one time, the problem is to calculate the positions and velocities of the particles at any other time. The motion in the n-body problem is described by a set of $3n$ second-order differential equations. Therefore, $6n$ constants of integration are required to describe the complete motion of the system. However, only 10 integrals of motion (as determined by Euler [1]) are known to exist: six constants from the center of mass motion, three constants from conservation of angular momentum, and one constant from conservation of energy. Using the set of 10 integrals of motion, the set of equations describing the motion of the n-body system can be reduced to $6n-10$. By replacing time with another coordinate and using the "elimination of the nodes" as introduced by Jacobi [1], the order of the equations of motion can be reduced to $6n-12$. Therefore, no known solution exists for the general n-body problem for $n > 2$. However, particular solutions (solutions for a special set of initial conditions) of the three-body problem are known.

One of the most well known particular solutions of the classical three-body problem was first given by Lagrange in 1772 [1]. He showed that for special cases the three-body configuration will retain its geometrical form (*e.g.*, three points on the vertices of an equilateral triangle, or three colinear points), although the shape may rotate or change in size

[2]. Another special case of the three-body problem called the circular restricted three-body problem has been extensively studied by Poincaré. For this particular case, two massive particles move in circles about the common center of mass and attract (but are not attracted to) a third particle of negligible mass. This case is immediately applicable to an Earth-Moon-spacecraft system. For the case in which the mass of the third body is small but nonnegligible, the starting point of the problem is to describe the two massive bodies with a two-body solution, then treat the change in motion of this system due to the third body with a perturbative approach. The problem of n point charges interacting only through electrostatic forces can be mapped onto the general n-body problem as proposed by Newton, since the classical form of electrostatic forces is essentially equivalent to that of gravitational forces; the only difference is that electrostatic forces can be both attractive and repulsive. Although the classical three-body problem has received a great amount of attention from astronomers and mathematicians, it remains unsolved three centuries after it was first proposed.

Attempts were made early in this century to describe the three-body problem in atomic and molecular systems using classical and semiclassical ideas. Bohr succeeded in deriving the energy spectrum of hydrogen in 1913; however, his attempt to find a reasonable estimate for the ground state energy of helium was a dismal failure [3]. Another system of early interest was the H_2^+ molecule. The approximate classical analog of this problem was first solved by Euler [4]. He treated the problem of two stationary masses attracting a third light mass. By introducing elliptical coordinates, the system can be separated into three second order differential equations which have elliptic functions as solutions. Sommerfeld later developed a semiclassical theory by generalizing the early ideas of Bohr. He gave Wolfgang Pauli the task of applying these semiclassical rules to describe H_2^+ for his Ph.D. thesis. Pauli concluded (wrongly) that H_2^+ could only be metastable. Despite the recent resurgence in semiclassical methods for treatment of quantum systems, a proper semiclassical

treatment of helium has remained elusive [5]. These early failures of semiclassical methods to accurately describe atomic and molecular systems were extremely important in motivating the development of a new quantum theory.

With the introduction of nonrelativistic quantum mechanics by Schrödinger [6] and Heisenberg [7], the concepts of classical trajectories and orbits all but disappeared; however, notions of energy and angular momentum remained. One of the first issues which arose shortly after quantum mechanics was introduced was the application of this theory to systems of particles [8]. This "new" quantum theory was quickly adopted to address the three-body problem for the cases of the atom, the nucleus, and the molecule [9]. The molecular case is different from the atomic and nuclear cases, as it is a system composed of two heavy particles and one light particle. Thus, this system can be considered a special case of the more general three-body problem. For the molecular three-body problem (*e.g.*, H_2^+), the rapid motion of the electron dominates over the slow motion of the heavy nuclei. This difference in relative speeds allows an approximate separation (using prolate spheroidal coordinates, see Refs. [10] and [11]) of the system into two parts: 1) electronic motion about two fixed centers, and 2) slow nuclear motion in a time averaged field of 1), as first shown by Born and Oppenheimer [12].

For atomic and nuclear systems, the description of the three-body problem is more complicated than that for the molecular case. For these systems, all interparticle forces are comparable. Also, there is no single fast particle to be identified; this precludes the description of motion in a time averaged field. The molecular system can be transformed into the atomic or nuclear system by gradually increasing the mass of the light particle. Upon performing this transformation, two new features of the modified system become apparent. First, the molecular potential no longer acts between the two nuclei, but rather between one heavy particle and the center of mass of the heavy and light particle. Second, as the mass of the light particle is increased, the velocities of the two parts of the system become

comparable to the internuclear motion. Using these types of ideas, Wheeler [9] addressed nuclear structure from a molecular viewpoint, and, in addition calculated the binding energy of ^{3}H.

One problem of early interest in understanding the nature of nuclear forces was the scattering of slow neutrons by deuterons. Early attempts to describe these types of nuclear collisions involving more than two particles [13, 14, 15, 16] used an approximate total wavefunction of the form $\Psi = \sum_i \psi_i f_i$, where ψ_i is a product of the internal wavefunctions of the two colliding nuclei, and f_i is the wavefunction of relative motion. The sum is performed over all pairs of nuclei whose formation is energetically possible. Although this form of the wavefunction is accurate when the two nuclei are widely separated, it does not accurately represent the wavefunction when the two nuclei are interacting with each other. Motz and Schwinger [17] performed a detailed calculation of neutron-deuteron scattering using a variational approach. Kohn [18] later developed a variational approach similar to the Rayleigh-Ritz method and applied it to calculate neutron-protron and neutron-deuteron scattering cross sections.

Another early test of Schrödinger quantum mechanics in addressing three-body systems was an accurate description of the energy levels of helium. Earlier attempts to describe the structure of helium (and heavier atoms) adopted a central field approximation [19, 20, 21]. The basic idea of the central field approximation is that each electron moves in an effective spherically symmetric potential $V(r)$ representing the interaction of the nucleus and the other electrons. Adopting this approximation with the self-consistent field approach, the early attempts were able to give energy values in fairly good agreement with theoretical values. Hylleraas [22] adopted the Rayleigh-Ritz variational method and performed a transformation of the independent electron coordinates r_1 and r_2 ($s = r_1 + r_2$, $t = r_1 - r_2$, and $u = r_{12} \equiv |\vec{r}_1 - \vec{r}_2|$) to obtain a very accurate description of the helium ground state. Today, the structure of the helium atom is considered essentially "solved." For example, the

theoretical and experimental values of the helium ionization energy agree to one part in 10^7 [11].

In contrast to the bound state structure of helium, our effort to understand the helium continuum (the continuum refers to states in which one or both electrons possess enough kinetic energy to escape to infinity) is still a work in progress. Much progress has been made in describing single electron escape processes in atomic physics [23]. Although the cross section profiles of these processes often exhibit a rich and complex set of features, reflecting a diverse range of interactions, theoretical methods exist to reliably reproduce these electron escape cross sections. Scattering processes in which the target absorbs enough energy for two electrons to escape are much more difficult to describe. For single escape, if the energy of the incoming projectile is known, then by energy conservation, the energy of the escaping electron at asymptotic distances is constrained to be the initial target state energy plus the projectile energy less the energy of the remaining fragment. However, for double escape, there are no longer any constraints on the energy distribution between the two escaping electrons (other than the indistinguishable particle requirement that this distribution is symmetric). This added difficulty of not being able to analytically express the asymptotic wavefunction for double escape has been a major barrier in past attempts to properly describe this process.

In this work, we attempt to accurately describe the two electron continuum wavefunction. Theoretical efforts to accurately describe double electron escape have had limited success until recently. These efforts have been enhanced by the availability of efficient modern day computer resources. An "exact" numerical treatment of two escaping electrons out to infinity remains impractical. However, suitable approximations allow an accurate description of many details in these processes. Double electron escape processes can occur in both electron scattering and photoabsorption. In this work, the focus is primarily on double photoejection of H^- and He.

The first quantum mechanical treatment of two electron systems can be traced back

to efforts to describe the energy spectrum of helium. It therefore seems natural to revisit the helium system in addressing the double continuum problem. The Schrödinger equation for helium is one of the simplest nonseparable equations which occurs in atomic physics. As such, this system cannot be described by a separable analytical expression in independent particle coordinates. Helium is an ideal system for studying the effects of electron correlations, since no core electrons are present to modify the electron-nucleus Coulomb interaction. Double electron escape by photoejection is easier to model than escape by electron scattering, due to the absence of long-range forces between the incoming projectile and the target state. The experimental community has also expended much effort in measuring helium photoionization processes. For these reasons, the helium double photoionization process represents an ideal test case for theoretically describing the details of two electron escape.

Past studies of helium have been motivated by efforts to understand the importance of electron-electron correlations in various processes. The importance of these correlations was experimentally probed by Madden and Codling [24]. They observed the autoionization of doubly excited states of helium after photoabsorption in the early 1960's. A few years later, experimental studies of helium photoabsorption were performed at photon energies above the double escape threshold. Carlson [25] first measured the ratio of double to single photoionization cross sections in helium in the photon energy range of 100-600 eV. Later experiments gave results that were inconsistent with the earlier experimental results of Carlson and with each other [26]. Various theoretical attempts to calculate the branching ratio also gave a broad distribution of values [26]. Twenty-five years after the original experiment of Carlson, a quantitatively accurate description of the fundamental two electron process of helium double photoionization in the intermediate energy range (100-600 eV) remained elusive. It was the lack of agreement among then-existing experimental and theoretical values of helium double photoionization cross sections in this energy range which strongly motivated the subject of this dissertation.

In the early 1990's, extensions of close coupling methods which treated the continuum with a discretized representation showed promise in describing two electron escape processes [27]. Most of these methods were developed to describe electron scattering processes. Previous calculations of helium double photoionization used perturbative approaches such as many-body perturbation theory, the Born approximation, or distorted wave Born approximation. One might expect these methods to work well at high energies. For these energies the importance of interactions between electrons as they escape is small in comparison to their large kinetic energies, thereby allowing the $1/r_{12}$ term to be treated perturbatively. However, at lower energies one would expect the $1/r_{12}$ term to significantly influence two electron escape. Therefore, electron correlations cannot be accurately treated perturbatively in this energy range.

In this work, we extend the eigenchannel R-matrix approach to describe two electron photoejection processes. This method treats electron-electron interactions nonperturbatively in the region near the target nucleus (the reaction volume), where these effects are assumed to be important. Outside the reaction volume, the wavefunction is approximated by a separable solution: the outer electron is subject to only a Coulomb potential of charge $Z-1$ (Z being the charge of the nucleus), assuming the inner electron efficiently screens the nucleus. One expects this approximation to break down at energies just above threshold, but it should be valid for energies at least a few eV above threshold.

In Chapter 2 of this work, we attempt to put the double continuum problem into perspective. Early theoretical attempts to describe two electron escape are discussed, in addition to more recent alternatives to the eigenchannel R-matrix approach. We next discuss the dependence of two electron escape on projectile energy, experimental progress in measuring double photoionization processes, and other aspects of the double escape process.

Chapter 3 is devoted to our initial R-matrix treatment of helium double photoionization [28]. The eigenchannel R-matrix method and its extension to describing two electron

escape are discussed in detail. Double photoionization results are presented for energies of 80-280 eV, and the discrepancy between calculations using different forms of the dipole operator is addressed. An application of our approach to a simplified model of electron scattering is also included [29]. This chapter concludes with a discussion of the problems that arise when treating the continuum with a discretized set of states, and outlines systematic techniques used to overcome these problems. In particular, a frame transformation technique is introduced as a procedure for distinguishing between single and double escape cross sections.

In Chapter 4, we combine a finite element basis set with the eigenchannel R-matrix method to describe double photoejection of helium and H^- [30]. This local finite element basis set is adopted to replace the global hydrogenic basis set used in our initial calculations. Application of this new approach greatly reduces discrepancies present in results obtained using our original method. We also use this finite element method to address other details of two electron escape [31]. A discussion of the similarities and differences between helium and H^- targets is included.

CHAPTER 2

TWO ELECTRON ESCAPE: PUTTING THE PROBLEM IN PERSPECTIVE

2.1 Preliminary Theory and Initial Assumptions

The formalism for calculating photoionization cross sections is quite straightforward. The starting point is commonly referred to as Fermi's Golden rule [11]:

$$dW = \frac{2\pi}{\hbar} \left|\langle \psi_f | H_{int.} | \psi_i \rangle\right|^2 \rho_f(E) \delta(E_f - E_i), \tag{1}$$

where dW is the transition rate, $H_{int.}$ is the interaction Hamiltonian between the atom and field, and $\rho_f(E)$ is the density of final states. The full Hamiltonian of the system is given by

$$H = H_{atom} + H_{int.} + H_{radiation}, \tag{2}$$

where the atomic Hamiltonian is

$$H_{atom} = \sum_i \left(\frac{\vec{p}_i^{\,2}}{2m} - \frac{Ze^2}{|\vec{r}_i|} \right) + \sum_{i>j} \frac{e^2}{|\vec{r}_i - \vec{r}_j|}. \tag{3}$$

The classical Hamiltonian (in Gaussian units) describing an atom in an electromagnetic field ($H_{atom} + H_{int.}$) is given by:

$$H = \sum_i \frac{1}{2m_i} \left(\vec{p}_i + \frac{e\vec{A}(\vec{r}_i, t)}{c} \right)^2 + V(\vec{r}_1, \vec{r}_2, \cdots, \vec{r}_N), \tag{4}$$

where V is the electrostatic potential energy of the atom. In this analysis, we neglect the interaction between the nucleus and the radiation field, and we neglect the spin interaction of the electron with the magnetic field, normally expressed as:

$$-\sum_i \vec{\mu}_i \cdot \vec{B}(\vec{r}_i, t). \tag{5}$$

We also neglect reduced mass effects, assuming an infinite mass nucleus is located at the origin of our coordinate system. The interaction Hamiltonian is identified as:

$$H_{int.} = \sum_{i=1}^{N} \left(\frac{e}{2mc} \left[\vec{p}_i \cdot \vec{A}(\vec{r}_i, t) + \vec{A}(\vec{r}_i, t) \cdot \vec{p}_i \right] + \frac{e^2}{2mc^2} \left| \vec{A}(\vec{r}_i, t) \right|^2 \right). \tag{6}$$

For the weak field regime considered here, the $|\vec{A}|^2$ term can be neglected. That is, we neglect two-photon processes. Choosing the Coulomb gauge for $\vec{A}$ ($\nabla \cdot \vec{A} = 0$), $\vec{p}$ and $\vec{A}$ commute. Therefore, $H_{int.}$ can be expressed as a single term. Introducing the vector potential $\vec{A}$ in the form

$$\vec{A}(\vec{r}_i, t) = \sqrt{\frac{2\pi c^2 \hbar}{\omega V}} \hat{\epsilon} \left(a e^{i\vec{k}\cdot\vec{r}_i} + a^\dagger e^{-i\vec{k}\cdot\vec{r}_i} \right) e^{-i\omega t}, \tag{7}$$

where $\vec{k}$ and $\vec{\omega}$ are the wavenumber and angular frequency of the radiation, V is the volume, and $\hat{\epsilon}$ is the polarization vector. The electric dipole approximation can now be used to replace $e^{\pm i\vec{k}\cdot\vec{r}_i}$ by unity, since for the photon energies considered in this work, the radiation wavelength is much larger than atomic dimensions. The interaction Hamiltonian is then given by

$$H_{int.} = \sum_{i=1}^{N} \frac{e}{mc} \sqrt{\frac{2\pi c^2 \hbar}{\omega V}} \left(\hat{\epsilon} \cdot \vec{p}_i \right) \left(a + a^\dagger \right) e^{-i\omega t}. \tag{8}$$

From the Golden rule (Eq. 1), the transition rate is given by

$$W_{1\to 2} = \int dW_{1\to 2} \tag{9}$$

$$= \frac{4\pi^2 e^2}{m^2 \omega V} \left| \langle \psi_2 | \sum_i \hat{\epsilon} \cdot \vec{p}_i | \psi_1 \rangle \right|^2. \tag{10}$$

Dividing the transition rate by the incident flux (c/V), and introducing the fine structure constant $\alpha = e^2/\hbar c$, the cross section σ is given by

$$\sigma_{1\to 2} = \frac{4\pi^2 \hbar \alpha}{m^2 \omega} \left| \langle \psi_2 | \sum_i \hat{\epsilon} \cdot \vec{p}_i | \psi_1 \rangle \right|^2, \tag{11}$$

or in atomic units ($e = \hbar = m = 1$),

$$\sigma_{1\to 2} = \frac{4\pi^2 \alpha}{\omega} \left| \langle \psi_2 | \sum_i \hat{\epsilon} \cdot \vec{p}_i | \psi_1 \rangle \right|^2 (a.u.). \tag{12}$$

Cross sections in this study will be given in units of barns (1 barn = 10^{-28} m^2). Assuming linearly polarized light (the case treated in this work) in the z-direction, and also assuming the total orbital angular momentum of the initial state $|\psi_1\rangle$ is zero, the cross section is given by

$$\sigma_{1\to 2} = \frac{4\pi^2\alpha}{3\omega}\left|\langle\psi_2\|\sum_i \frac{\partial}{\partial z_i}\|\psi_1\rangle\right|^2, \tag{13}$$

where $\langle\psi_2\|\sum_i \frac{\partial}{\partial z_i}\|\psi_1\rangle$ represents a reduced dipole matrix element.

The above form for the cross section is referred to as the velocity form. This equation has corresponding length and acceleration forms (see Appendix A). Using the identity

$$\langle\psi_2|[\vec{r},H]|\psi_1\rangle = \langle\psi_2|\frac{i\hbar}{m}\vec{p}|\psi_1\rangle = (E_2-E_1)\langle\psi_2|\vec{r}|\psi_1\rangle, \tag{14}$$

we can obtain the cross section by evaluating the matrix element $\langle\psi_2|\vec{r}|\psi_1\rangle$. Similarly, one can use the identity:

$$\langle\psi_2|[\vec{p},H]|\psi_1\rangle = (E_2-E_1)\langle\psi_2|\vec{p}|\psi_1\rangle = \langle\psi_2|[\vec{p},V]|\psi_1\rangle = -i\hbar\langle\psi_2|\sum_i \nabla_i|\psi_1\rangle. \tag{15}$$

For a potential of the form $V = -Z\sum_i \frac{e^2}{r_i} + \sum_{i<j}\frac{e^2}{|\vec{r}_i-\vec{r}_j|}$, the matrix element $\langle\psi_2|\sum_i \nabla_i|\psi_1\rangle$ is given by

$$Ze^2\langle\psi_2|\sum_i \frac{\vec{r}_i}{r_i^3}|\psi_1\rangle. \tag{16}$$

There is no net contribution to the above expression from the gradient operator operating on the Coulomb repulsion term, as ∇_i and ∇_j applied to this term give equal and opposite contributions. If the wavefunctions $|\psi_1\rangle$ and $|\psi_2\rangle$ are exact, then all three forms (length, velocity, and acceleration) should give identical results. In this work, we use all three forms as a method for evaluating the accuracy of our wavefunctions. Since the length form is proportional to $\vec{r}$, it samples the large r behavior of the wavefunction. In contrast, the acceleration form is proportional to $1/r^2$, and so samples the wavefunction's small r behavior.

2.2 Simplified Descriptions of Two Electron Escape

The double ionization cross section for a two electron system can be expressed as

$$\sigma^{++}(E) = \frac{4\pi^2\alpha}{(2J_0+1)\omega}\sum_l \int_0^E d\epsilon \int_0^E d\epsilon' \delta(\hbar\omega - E_{D.I.} - \epsilon - \epsilon')|M_{fi}|^2, \tag{17}$$

where (for linearly polarized light in the z-direction)

$$M_{fi} = \int d\vec{r}_1 \int d\vec{r}_2 \psi_f(\vec{r}_1, \vec{r}_2)(\frac{\partial}{\partial z_1} + \frac{\partial}{\partial z_2})\psi_i(\vec{r}_1, \vec{r}_2), \tag{18}$$

J_0 is the total angular momentum of the initial state, $E_{D.I.}$ is the double ionization threshold energy, and ϵ and ϵ' are the energies of the two escaping electrons. Information about the initial and final state is all that is required to calculate this cross section. Also, since the initial state is spatially confined to a small region, a description of the final state wavefunction for only relatively small values of $|\vec{r}_1|$ and $|\vec{r}_2|$ is required to evaluate M_{fi}. However, the asymptotically large r form is required to determine the short-range r behavior of the final state wavefunction. An accurate description of the ground state wavefunction (the Hylleraas approach [22]) has been available for quite some time. The difficulty which remains is an accurate description of the double continuum final state wavefunction.

The simplest treatment of two electron escape adopts the sudden approximation [25]. In this approximation, the "fast" electron is assumed to suddenly escape. The amplitude for the inner electron to escape subsequently is proportional to the projection of a one-electron wavefunction representing the inner electron onto a continuum hydrogenic wavefunction. This approximation was originally applied in the context of beta decay, where the effect of electron excitations was investigated for a sudden change in the charge of a nucleus [32]. This approach is known to give reasonable results for atoms with relatively large values of the nuclear charge Z ($Z \approx 25$, see Ref. [32]).

More sophisticated methods have been applied to describe the probability of a second electron escaping an atom due to the change in the potential from the escape of the first electron; this is known as the "shake-off" mechanism [25]. These methods give

roughly the correct order of magnitude for the double escape cross sections, but tend to underpredict the correct values [25, 33]. Other mechanisms were proposed in an attempt to describe two electron escape. Samson observed empirically that the ratio of double to total ionization was approximately proportional to the cross section for electron impact ionization of an ion [34]. This motivated his development of a classical model which described double photoionization as a two step process (and therefore labeled as a "two-step one" contribution in many body perturbation terminology): first, the photon is absorbed by one electron, and second, the excited electron scatters from the remaining electron as it leaves the ion. This simple description was recently adopted in a semiclassical treatment of helium double photoionization and found to give reasonable results [35]. Many body perturbation treatments [36, 37] identified the contributions to double ionization as falling into three categories: ground-state correlations, shake-off, and two-step one. These last two processes are final state correlation effects. However, it was shown that the relative strengths of these mechanisms depend on the form of the dipole interaction [38, 39]. Consequently, as seen by their dependence on the dipole form, these mechanisms can not be viewed as physical processes; they are only useful for visualizing the process of double photoionization in a qualitative sense.

Early studies [40] illustrated the importance of including an accurate ground state wavefunction in order to get accurate double ionization cross sections. The first attempts to calculate double photoionization normally adopted a final state wavefunction represented as a symmetrized product of uncorrelated Coulomb wavefunctions [40, 41]. Each of these Coulomb functions were for a charge of $Z = 2$. That is, screening between the electrons was ignored. Although these studies obtained results that were in fairly good agreement with existing theory, a notable discrepancy appeared between calculations using various dipole forms.

Further attempts to analytically represent the three-body Coulomb continuum final

state achieved mixed success. Using a product wavefunction consisting of three two-body Coulomb wavefunctions (also known as the Brauner-Briggs-Klar(BBK) wavefunction [42]), Maulbetsch and Briggs [43] were able to accurately reproduce the shape of electron angular distributions in double photoionization, but predicted absolute cross sections that were orders of magnitude too low. Recent attempts to address this normalization problem have been somewhat successful [44].

2.3 Discrete Methods for Treating the Double Continuum

The greatest obstacle to the theoretical description of two electron escape derives from an inadequate understanding of how to impose the proper boundary conditions at infinity. For this reason, methods that aspire to directly represent the two-electron continuum as a channel expansion of an uncountable infinity of states are infeasible. Approximate perturbative methods which treat the double continuum in this manner (*e.g.*, the Born approximation) have been successful in calculating double continuum cross sections at sufficiently high energies (on the order of 1 keV [45]). However, alternate methods are required to describe double escape processes at lower energies.

Methods that use a discrete representation of all possible excitation channels have enjoyed tremendous success at low energies where only single escape is energetically allowed. This includes, for instance, the R-matrix method, variants of the close-coupling method that use pseudostates, and the convergent close-coupling (CCC) approach. In this work, we show that the eigenchannel R-matrix method is capable of describing a class of problems in the two-electron continuum, excluding energies very close to the threshold energy for double escape. Other coupled-channel methods have been similarly extended to treat the double continuum in recent years, notably the intermediate energy R-matrix (IERM) method [46], the CCC method [47], the R-matrix with pseudostates (RMPS) method [48], and the hyperspherical close-coupling (HSCC) method [49]. Although many of these methods have been applied primarily to describe electron scattering rather than photoejection, both processes involve

the same final state dynamics, and are thus closely related. It is important to explore the double escape energy region, in part because of its intrinsic theoretical interest. Yet another reason is that even processes involving single-electron escape could be adversely affected if the double continuum regions are linked in some sense, *e.g.*, through constraints such as the oscillator strength sum rule (often referred to as the Thomas-Reiche-Kuhn sum rule [50]).

A couple of early efforts that demonstrated the promise of discrete methods in describing two electron escape included a pseudostate treatment of electron-hydrogen scattering by Callaway and Oza [51], and a multichannel J-matrix calculation of double photoejection of H^- by Broad and Reinhardt [52]. Both of these pioneering attempts were hindered by the lack of powerful computing resources which are presently available. The first true demonstration of the capability of a discretized method to obtain accurate total double escape cross sections was shown in the CCC treatment of electron-hydrogen scattering by Bray and Stelbovics [27]. They were able to obtain excellent agreement with experiment over the wide energy range 4-500 eV above the ionization threshold. Complementing this effort was the work of Kato and Watanabe [53], which used the hyperspherical close-coupling method to calculate ionization cross sections of electron-hydrogen scattering. They were able to obtain excellent agreement with experimental cross sections for energies as low as 0.1 eV above the ionization threshold. These calculations are quite noteworthy, as efforts to theoretically describe this fundamental process accurately in the previously 50 years were largely unsuccessful.

The CCC method employs a close-coupling representation to solve the momentum-space Lippmann-Schwinger equation that derives from the full three-body Schrödinger equation. A Sturmian basis set is chosen to diagonalize the target Hamiltonian in momentum space. This choice of basis functions eliminates numerical problems associated with convergence and linear dependence. For a fixed energy value, the basis set size is systematically increased until the observable of interest converges. This discrete basis set is increased in

such a way that additional members extend to successively larger radii. Further details of the CCC method can be found in Refs. [45] and [47].

In addition to calculating accurate two-electron continuum cross sections for electron-hydrogen scattering, the CCC approach has produced reliable cross sections for electron-He^+ ionization from threshold to 700 eV [54], for positron-hydrogen scattering [55], and more recently for electron-helium scattering in the frozen core approximation [56]. This approach also determined accurate observables in electron scattering by Na, judging from its close reproduction of spin-resolved measurements; furthermore, it should also be straightforward to apply it to electron scattering by other targets with one valence electron (*e.g.*, Li and K) [57]. In addition to obtaining bound state excitation and ionization cross sections, the CCC formulation was used to calculate spin asymmetries and differential, integral, and total cross sections. This approach has also been recently applied to calculate helium double photoionization cross sections [58]. A summary of applications of the CCC approach is reviewed in Ref. [45]. Although this method has enjoyed great success in describing electron scattering processes, problems with this method in obtaining converged energy distributions have recently surfaced [59]. The origin of these problems is still not fully understood.

The hyperspherical close-coupling (HSCC) approach has been used to describe two electron escape in both electron scattering [53, 60, 61] and photoabsorption processes [62]. This method replaces the independent particle radial coordinates r_1 and r_2 by a pair of collective variables R and α. The hyperradius $R = \sqrt{r_1^2 + r_2^2}$ measures the "size" of the electron system and the hyperangle $\alpha = \tan^{-1}(r_2/r_1)$ describes the degree of electron-electron radial correlations. Reexpressing the two electron atom Schrödinger equation in these coordinates, one can apply the adiabatic approximation in the hyperradius (the only remaining infinite range variable). In the past, this hyperspherical coordinate method had been useful mainly in the qualitative description of electron correlations [63, 64]. However, using the HSCC

method, Tang *et al.* were able to obtain an accurate, high precision description of doubly excited resonances just below the double escape threshold by treating electron-electron interactions accurately out to very large distances (R=170 a.u.) [65].

One of the drawbacks of the hyperspherical coordinate method is the slow convergence in calculating adiabatic potential curves when using the traditional basis set, namely a set of functions of the hyperradius multiplied by adiabatic channel functions (functions of the five angular coordinates $\alpha, \hat{r}_1$, and $\hat{r}_2$, which are solutions of the adiabatic Hamiltonian for the parameter R). Tang *et al.* adopted an alternative numerical method, called the diabatic-by-sector method [66], to solve the hyperspherical close-coupling equations. A two-dimensional independent coordinate matching scheme was adopted [67] to match the inner region wavefunction to the asymptotic solution. Using this HSCC method, Kato and Watanabe were able to reproduce the experimental ionization cross sections for electron-hydrogen scattering down to energies as low as 0.1 a.u. [53]. They were also able to provide numerical evidence of the 1.127 value of the Wannier exponent (defined in Eqs. 19 and 20) and the uniform energy distribution predicted by Wannier theory (for the near-threshold energy range) [61]. Calculations of helium double ionization cross sections were performed for photon energies from threshold to 280 eV [62]. Very good agreement was achieved between the length and acceleration forms of the calculation using a matching radius of R=30 a.u.

A third computational approach, R-matrix theory, was first introduced by Wigner and Eisenbud to study resonance reactions in nuclear physics [68]. The advantage of R-matrix methods over CCC and HSCC type approaches is the fact that R-matrix methods essentially describe the electron scattering/photoabsorption process independent of the projectile energy. Therefore, R-matrix methods are ideally suited to the study of resonance phenomena, where observables can be calculated over a fine energy mesh with little additional computational effort.

In R-matrix theory, configuration space is partitioned into two (or more) regions

by a sphere of radius r=r_0, as shown in Fig. 1. The most complicated physics is included in the finite internal region (region I in Fig. 1), called the reaction volume. In the external region, electron-electron correlation effects are neglected, which is a good approximation for large enough values of r_0. It is the fact that exchange and correlation effects are confined to a small volume that makes the R-matrix method appropriate even in the presence of long-range Coulomb fields. Once the wavefunction is determined both inside and outside the reaction volume, the full solution is obtained by matching the logarithmic derivative of the wavefunction across the surface of the reaction volume and solving the Schrödinger equation in the exterior region.

In this work, we adopt the eigenchannel R-matrix method. We use this method to calculate variationally a particular set of Schrödinger solutions: each solution has a constant normal logarithmic derivative across the surface of the reaction volume. Further details of this method will be discussed in Chapter 3. Other variations of the R-matrix method can be used to obtain identical results for two electron processes, provided an identical basis set is used [69, 70]. Two alternative approaches of R-matrix theory that have recently been applied to address double continuum processes include the intermediate energy R-matrix (IERM) method and the R-matrix with pseudostates (RMPS) method.

The major advancement of the IERM method over previous R-matrix methods was the inclusion of continuum-continuum orbital couplings in the inner region [46]. That is, all electron exchange and correlation effects between both continuum electrons and the core are included in the reaction volume. In their approach, the internal region of configuration space is further divided into a number of subregions to treat inelastic effects. The systematic introduction of continuum pseudostates in the inner region leads to pseudoresonances at intermediate energies. A T-matrix energy averaging scheme [71], which involves continuation to complex energies, is adopted to average out the flux contributions of these pseudoresonances and therefore obtain smooth cross sections.

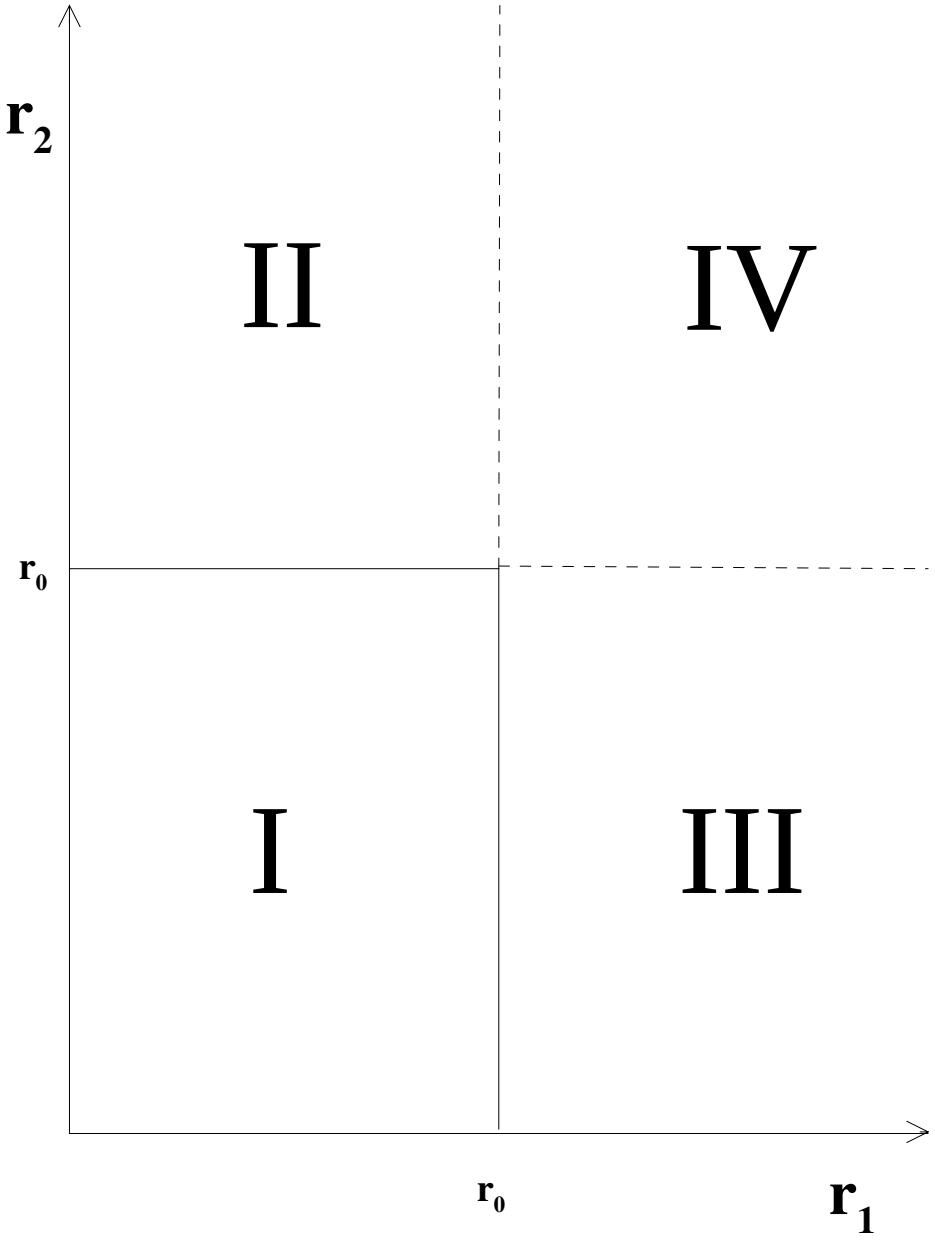

Figure 1. Radial configuration space for two electrons used in R-matrix theory. Region I represents the reaction volume, regions II and III represent single electron escape, and region IV represents the double continuum. This figure is taken from Ref. [28].

The IERM method has been applied to calculate elastic, $1s-2s$, and $1s-2p$ cross sections for electron-hydrogen scattering at intermediate energies [72, 73]. This method has also been applied to calculate electron-hydrogen ionization cross sections for projectile energies up to 50 eV [74]. These calculated values were slightly larger than the experimental values of Shah, Elliot, and Gilbody [75] at higher energies. Recent ionization cross section calculations for a simplified s-wave model of electron-hydrogen scattering (the Temkin-Poet model) in the energy range from threshold to 5 eV above threshold compared favorably with similar CCC and RMPS calculations [76]. By going to a large reaction volume, they were able to represent the energy region above the ionization threshold with a dense set of pseudostates. Converged results were obtained for a reaction volume radius of 150 a.u. Preliminary IERM calculations for the full electron-hydrogen scattering problem using a reaction volume radius of 63 a.u. appear promising; ionization cross sections for the $^1S^e$ partial wave are consistent with the $E^{1.127}$ power law.

The R-matrix with pseudostates method (RMPS) recently developed by Bartschat *et al.* [48] utilizes the Belfast R-matrix codes developed by Burke *et al.* [77]. The motivation for using these existing computer codes, which have been developed over many years, is the desire to extend this method to handle electron scattering processes in the low and intermediate energy range for a general N-electron atom or ion. In this method, both target eigenstates and pseudostates are included in the basis set. The pseudostates consist of a finite expansion of Sturmian orbitals. These two types of basis functions included in the wavefunction expansion are not orthogonal. However, Bartschat *et al.* adopt the Schmidt orthogonalization procedure to generate a new orthogonal basis set. Following an initial application to electron-hydrogen scattering [78], the RMPS method has been applied to study electron scattering by helium [79], beryllium [80], and boron [81]. Ionization cross sections for the simplified s-wave (Temkin-Poet) model of electron-hydrogen scattering have also been calculated using this method [82]. An alternate version has recently been developed

by Gorczyca and Badnell to study photoionization-excitation processes in helium [83].

2.4 Dependence of Double Escape on Projectile Energy

An ideal scattering/photoejection theory should be capable of calculating reliable cross sections independent of the projectile energy. In practice, this ideal theory has not yet been developed. To appreciate the limitations of current numerical methods to calculate double escape cross sections over the entire energy range of an incoming projectile, it is useful to understand the defining features of two electron escape in each energy region. In this work, our focus is on the intermediate energy region, as defined below.

The minimum projectile energy required to produce double photoejection or electron impact ionization processes is called the double escape or ionization threshold (78.98 eV for helium double photoionization, 14.35 eV for H^- double photodetachment). At energies just above threshold, the double escape process is difficult to describe with discrete methods, as interactions between the two escaping electrons are important out to very large distances from the target. Also, the low speeds of near threshold particles translate into long times over which correlations can develop. Much effort has been expended in exploring threshold laws to describe the energy dependence of escape cross sections in the energy region just above threshold. The primary theoretical motivation for studying threshold laws lies in the understanding that the energy dependence is very sensitive to long range interactions in the final state. Therefore, threshold laws provide a diagnostic for characterizing long range interactions (*e.g.*, polarization and dipole forces), a subject of broad interest in atomic physics.

One of the earliest works on this subject was contributed by Wigner [84], who identified several key features of threshold laws. Since threshold laws are only dependent on a single parameter, namely the excess energy E of the final state (for the case of inelastic processes, as considered here), the threshold law is insensitive to the details of the initial preparation of the state. This provides yet another close link between electron scattering

and photoabsorption. For example, the same threshold law which describes the electron-hydrogen scattering ionization cross sections also describes double photodetachment of H^-. Since threshold laws are controlled by long-range interactions, the threshold exponent is independent of the physics within the reaction zone, the region in which the particles are all close together. This enables one to obtain a threshold law without having to solve for the full solution in the reaction zone, where much of the complicated physics occurs. An additional explanation can be given as to why the region in which the outgoing particles have a large separation controls the threshold law. For large separations the potential interaction is small, so small values of E are significant. However, when the particles are close together, large interaction energies are involved. Therefore, small variations in E will have little effect on particles of small separation.

For the three-body Coulomb continuum problem (*e.g.*, electron impact ionization of hydrogen or double photodetachment of H^-), the Wigner threshold law is dependent on the assumption one makes for the final state [85]. If one represents the final state as a product of two one-electron wavefunctions, there are two limiting cases for modeling electron correlations. If one makes the assumption that the slower electron completely screens the nucleus, the final state can be described as a product of a Coulomb function and a plane wave, leading to the threshold law $\sigma \propto E^{3/2}$. However, if the final state is represented as a product of two Coulomb functions, then the threshold law $\sigma \propto E$ results. The real threshold law is expected to lie between these two cases, *i.e.*, $\sigma \propto E^m$, where $1 \leq m \leq 3/2$.

The next major contribution to our understanding of threshold laws was provided by Wannier [86]. Wannier's theory is a classical theory. Since for energies above the double ionization threshold the electrons are characterized by small wavelengths at intermediate distances, he felt a classical treatment was justified for addressing this problem. Wannier recognized the importance of correlations in describing threshold laws and concluded that any representation of the final state as a product of one-electron wavefunctions would be

insufficient for understanding the threshold behavior. He abandoned the independent radial coordinates, replacing them with the hyperspherical coordinates R and α.

A central concept of Wannier theory is the importance of dynamic screening. As previously mentioned, the picture of static screening in which the final state is represented as a separable solution of the Schrödinger equation is insufficient. Rather, a picture of the screening changing as energy is partitioned between the two electrons is a more accurate view. If one particle is slightly closer to the target nucleus than the other particle, the closer particle will contribute more to screening of the outer particle. As a result, the outer particle gains a greater share of the energy, leading to a further enhancement of the unequal screening of the two escaping particles. Wannier reasoned that two electron escape processes would only occur at low energies for tight energy correlations. He restricted double escape processes in configuration space to a small region neighboring the point $\theta_{12} = \pi$ ($\theta_{12} \equiv \cos^{-1}(\hat{r}_1 \cdot \hat{r}_2)$) and $\alpha = \pi/4$. The point $\theta_{12} = \pi$ describes the two electrons as moving in opposite directions from the nucleus, while $\alpha = \pi/4$ corresponds to $r_1 = r_2$, namely, the two electrons escaping such that they remain equal distances away from the nucleus. By analyzing classical trajectories for $L = 0$ in the vicinity of the point $(\theta_{12} = \pi, \alpha = \pi/4)$, Wannier arrived at the following threshold law for double electron escape:

$$\sigma \propto E^m, \tag{19}$$

where

$$m = \frac{1}{4}\sqrt{\frac{100Z - 9}{4Z - 1}} - \frac{1}{4}. \tag{20}$$

For $Z = 1$, $m \cong 1.127$, and for $Z = 2$, $m \cong 1.056$. As $Z \to \infty$, $m \to 1$. Later quantum mechanical treatments of the threshold law [87, 88] reproduced the results of Wannier. (An alternative dipole threshold law has been proposed by Temkin [89]:

$$\sigma \propto [E/(\ln E)^2]\{1 + C\sin[\alpha(R)\ln E + \mu]\}, \tag{21}$$

where $\alpha = \sqrt{b - 1/4}$, b is the dipole moment seen by the outer electron, and C and μ are

constants. However, this threshold law is not generally accepted [90].)

One consequence of the Wannier picture is the prediction concerning the energy distribution between the two escaping electrons. According to Wannier theory, all possible partitions of E into E_1 and E_2 are equally likely near threshold [91]. This result has been experimentally verified in electron impact ionization of helium [92] and double photoionization of helium [93]. Concerning experimental evidence for the Wannier threshold law, these include experiments on electron impact ionization of hydrogen [75, 94], electron impact ionization of helium [92], double photodetachment of H^- [95], and double photoionization of helium [96]. It now appears possible that the Wannier threshold law can be explored by direct numerical calculations [61, 76, 97]. However, accurate calculations for this energy region are not possible for the eigenchannel R-matrix method adopted here for reasons which will be discussed in Chapter 3. One issue that often arises concerning discussions of threshold laws is the energy range over which threshold laws are valid. Although this question does not have a clear answer, one can normally assume that a threshold law is valid up to 1-2 eV above threshold.

The intermediate energy range can be characterized by the following two criteria: 1) the physical processes which occur in the reaction zone are important in describing the two electron escape process, and 2) the electron-electron interactions in the reaction zone are large enough that they can no longer be treated perturbatively. The first criterion eliminates the region just above threshold, as the energy dependence of double escape cross sections depends solely on the longe range forces. The second criterion eliminates the high energy regions, where perturbative methods (*e.g.*, the Born approximation) are sufficient for accurately describing two electron escape processes. In properly describing these processes for intermediate energies, an accurate nonperturbative method for treating the complicated electron-electron interactions in the reaction zone (reaction volume) is essential. This has been the focus of recent numerical discrete methods, discussed in the previous section.

One sensitive probe of the strength of electron-electron interactions is the ratio R of double-and-single photoejection cross sections ($R \equiv \sigma_{2e}/\sigma_{1e}$). Double photoejection could not occur in the absence of electron-electron interactions, at least in first-order perturbation theory for the photon-atom interaction. Since the maximum value of this ratio as well as the maximum value of the double escape cross section occurs in the intermediate energy range (*e.g.*, see Ref. [52]), escape processes in this energy range are a subject of great interest. Previous studies of helium double photoionization for these energies will be discussed in Chapter 3. One issue which arises for processes in this energy range is the size of the reaction volume required to obtain accurate results. Other than the fact that the required reaction volume radius grows as the inverse of the energy excess from threshold [61], there is no clear theoretical value for the required reaction volume radius. In practice, the size of the reaction volume is increased until converged results are obtained.

At high enough (but nonrelativistic) projectile energies perturbative methods can be used to calculate accurate double escape cross sections. Perturbative treatments of electron correlations rely on the assumption that one of the ionized electrons leaves the target area relatively rapidly. For this situation, in which the electron kinetic energies overwhelm the electron-electron interaction potential, the final state correlation effects are minimal. The assumption that the escaping electrons have very different speeds is approximately valid for photon energies much larger than the ionization potential of the target. The well known Born approximation does not formally include exchange or short-range distorting potentials. This method normally gives accurate results for projectile energies above 1 keV. Specific application of the Born approximation to two electron escape include the helium double photoionization calculations of Brown [41] and the electron-hydrogen ionization cross section calculations of Peach, whose values are reported in Ref. [27]. The distorted wave Born approximation (DWBA) improves on the Born approximation by including a short-range potential; that is, plane wave solutions in the Born approximation are replaced by distorted

waves. Further improvements can be attained by including higher order approximations, such as the second-order distorted-wave Born approximation (DW2BA) [98], which unlike the DWBA is able to include the effects of dipole polarization. Many body perturbation theory (MBPT) approaches have also been applied to calculate double photoionization cross sections in helium [33, 36, 37, 99]. The differences between these various many body calculations are due to differences in the choice of basis sets and in the methods used to estimate higher order corrections. Although these methods were applied for photons in the intermediate energy range, it is unclear as to how electron-electron interactions can be accurately treated perturbatively here.

One issue of great interest is the asymptotic (nonrelativistic) energy limit of the ratio of double and single photoejection cross sections. It is known [38] that the energy dependence of both single and double photoejection cross sections goes as $E^{-7/2}$ for high (but nonrelativistic) energies (the decrease in the cross section with energy is actually slower than $E^{-7/2}$ for relativistic energies [100]), and thus the ratio R approaches a constant. Dalgarno and Stewart [101] showed that the value of this constant is solely dependent on the initial state wavefunction. Dalgarno and Sadeghpour calculated the ratio values of 0.0150 for H^-, 0.0167 for He, and 0.0087 for Li^+ [38, 102].

A complete description of double photoejection at high energies is complicated by the importance of the atomic Compton effect [103], namely, $h\nu$+He$\rightarrow$ $h\nu'$+He^{2+} + e^- + e^-. Compton processes result from the presence of the $|\vec{A}|^2$ term (two photon process) in Eq. 6, which we have previously ignored. The Compton effect will become important in photoejection when the energy increase of the electron(s) (the energy $E = (\Delta p)^2/2m$ corresponding to the net momentum transferred (Δp) to the atom by the photons) is greater than the electron escape threshold. For helium, Compton processes are nonnegligable at photon energies greater than roughly 2.5 keV for single photoionization and 4.5 keV for double photoionization. These processes dominate at higher energies, since the single and double

photoionization cross sections fall off as $E^{-7/2}$ while the Compton scattering is roughly independent of energy. A new parameter of interest is then the asymptotic energy limit of the ratio R_C of helium double-and-single ionization by Compton scattering. There was some disagreement between theories in calculating this value. Amusia and Mikhailov [104] calculated a value R_C=0.0168, while three other studies [105, 106, 107] calculated a value of R_C=0.008. Bergstrom, Hino, and Macek calculated a value of R_C=0.016 at 20 keV, but concluded that their value had not yet reached an asymptotic limit [108] (their values of R_C were still decreasing with energy). One recent helium ionization experiment by 57-keV X rays obtained a value R_C=0.0125 [109] while a different experiment with 58-keV X rays measured a value which supports the smaller value of R_C (0.008) [110].

In summary, it is difficult for a single numerical method to accurately predict two electron escape cross sections over the full range of projectile energies. The role of electron correlations in double escape is highly dependent on the excess energy of the electrons, and so is difficult to describe. Discrete methods are primarily limited to the intermediate energy range. Limitations in the size of the reaction volume hinder an accurate treatment of long range correlations, which is required for describing near threshold behavior. Limitations in the size of the basis set hinder an accurate representation of escaping electrons with large excess energy, as the corresponding wavefunctions have small de Broglie wavelengths. The general profile of the double photoejection cross section is characterized by a zero value at threshold, a nearly linear increase for the first few eV above threshold, reaching a peak at intermediate energies before decreasing to zero at high energies, with an energy dependence of $E^{-7/2}$. This profile reflects the physical role of correlations. Double escape just above threshold is limited to a small region of phase space, as there is little excess energy available to partition between two escaping electrons. Likewise, double escape events at high energies are suppressed, as the energetic electrons spend little time near each other, and therefore have little time to interact. The profile of the ratio of double to single photoejection is similar to

the double photoejection cross section, except that the peak is broader and located farther from threshold, and the values fall off much more slowly with energy before eventually reaching a nonzero constant value. It is part of the challenge of discrete numerical methods to calculate the location and value of the peak ratio.

2.5 Experimental Progress in Measuring Double Photoionization Cross Sections

Much progress has been made in developing experimental methods to observe two electron escape processes excited by photoabsorption. In Carlson's original experiment [25], double photoionization events were produced by using low energy x-rays emitted by an x-ray tube. Modern double photoionization experiments are performed at synchrotron light facilities, which provide a high intensity, high energy source of radiation [111]. In typical experiments, the synchrotron radiation is focussed on a small jet of gas. The jet then drifts through an externally applied electric field. A time-of-flight spectrometer is used to distinguish between the singly- and doubly- ionized target residuals [112] (since doubly charged ions experience a greater acceleration in the field than singly charged ions, these ions will reach the detector first). A COLTRIMS (cold target recoil ion momentum spectroscopy) technique has also been very useful in distinguishing between Compton scattering and photoabsorption processes. For Compton processes, the momentum and energy transferred by the photon correspond to the energy and momentum of the emitted electron(s), whereas in photoabsorption the recoiling target ion must compensate for the momentum of the escaping electron(s). By using this technique to distinguish between events with small and large recoil ion momenta, Spielberger *et al.* [113] were able to separate photoabsorption and Compton scattering contributions.

Double photoionization experiments are difficult to perform, since these experiments usually involve the measurement of very small cross sections ($< 10^{-24}$ m^2 for helium).

The cross sections eventually decrease with increasing photon energy, compounding the problem. Consequently, even small sources of error can result in a significant distortion of the measured ratio of double-and-single photoionization [112]. One possible source of error in helium double photoionization experiments is the creation of spurious helium ions due to stray light or electrons. Since photoionization cross sections are much larger at energies just above threshold than at higher energies, even a small amount of stray light can create problems [112]. Another possible source of error is a difference in detection efficiencies of He^+ and He^{++} with the time-of-flight spectrometer and the channel plate, as the doubly and singly charged ions will reach the detector at different speeds. Experimental measurements are also very sensitive to contaminants in the helium gas, because the photoionization cross sections for these contaminants are often much larger than that for helium. Careful analysis of these possible sources of error has allowed recent measurements of the ratio of double-and-single photoionization to be performed with considerably improved accuracy, compared with earlier measurements. In addition, modern experiments have been performed over a much wider range of photon energies (*e.g.*, see Ref. [111]).

2.6 Observables and Targets as Probes of Electron-Electron Correlations

Although much of the current investigation has focussed on calculating a single process (photoabsorption) for a single target (helium ground state) for a single observable (ratio of double to single photoionization cross sections), the work presented here has a much broader context. The close relationship between electron scattering and photoejection has already been portrayed in previous sections. The dependence of two electron escape on the projectile energy has also been discussed. Further information about two electron escape processes can be obtained by calculating various observables. These include not only single, double and total photoionization cross sections, but also partial cross sections (single photoejection plus excitation of the remaining electron), energy distributions, and angular distributions. Exploration of these other observables help to provide a more complete picture

of two electron escape. A wealth of experimental data of observables for electron scattering exists; I will focus primarily on photoabsorption processes here.

A paper summarizing past theoretical and experimental determinations of helium partial cross sections has recently been published [114]. We will compare our calculated values to the experimental results in this paper in Chapter 4. In addition, experimental values exist for the angular distribution of helium photoelectron satellites $He^+ nl$ for n=2-7 over a large photon energy range [115]. Wehlitz *et al.* [93] have measured electron energy distributions in helium double photoionization for excess energies of 5-41 eV. Calculations of energy distributions for helium double photoionization include those of Hino *et al.* [39] using many body perturbation theory, and of Proulx and Shakeshaft [116] over the range of photon energies 89-140 eV. Pont and Shakeshaft explored the dependence of singly differential (in energy) cross sections on excess energy for the equal energy sharing case ($E_1 = E_2 = E/2$) [117]. Theoretical studies of helium double photoionization angular distributions performed by Maulbetsch *et al.* [118] and by Pont and Shakeshaft [119] agree fairly well with the experimental values of Schwarzkopf *et al.* [120]. In principle, our eigenchannel R-matrix method can be used to calculate all of these observables, although the procedure for calculating energy distributions is not necessarily straightforward. The accuracy of our method for the description of the double escape observables like angular distributions remains uncertain.

Further information about two electron escape can also be learned by probing different target states. Other than the isolated work of Teng and Shakeshaft [121], who explored double photoionization of the $He(1s2s^3S)$ metastable state, helium double photoionization studies have focused entirely on the He target ground state. Advances in experimental methods may allow measurements of double photoionization cross sections for the initial state $He(1s2s^3S)$ and other metastable states to be undertaken in the future.

Although this work has concentrated primarily on double photoejection of H^- and He, heavier elements in the helium isoelectronic sequence (Li^+,Be^{++}, C^{4+}, O^{6+}, $\cdots$) can also

be explored. Kornberg and Miraglia [122] have used an approximate analytical final state wavefunction to show that the ratio of double-and-single photoejection scales as a simple function of the nuclear charge Z. Further discussion of this topic is included in Chapter 4. The study of other heliumlike atom target states (Be, Mg, Ca, Sr, Ba, Ra) provide further opportunities for exploration of two electron escape. Accurate treatments of the heavier atoms (Ba, Ra) will require the inclusion of relativistic effects. Further complications arise at relatively high photon energies ($\approx$50 eV above threshold), where excitations of the inner-shell core occur. Experimental double ionization studies of several gases (He, O, N, Ar, and Ne) have been performed [123, 124]. Proper theoretical descriptions of these processes (other than helium) are difficult however, as these targets contain more than two electrons in the outer shell. In general, for both the case of theory and experiment, the study of two electron escape processes for various target species has been quite limited for photoabsorption in comparison to electron scattering.

CHAPTER 3

INITIAL APPROACH: EIGENCHANNEL R-MATRIX CALCULATION WITH A HYDROGENIC BASIS

3.1 Double Photoionization of Helium

The eigenchannel R-matrix method for single photoionization is extended here to describe a class of two electron escape processes. We apply this approach to calculate the double photoionization of helium by single-photon absorption, for photon energies in the range 80-280 eV [28]. Calculations are performed using the length (Eq. 14), velocity (Eq. 13), and acceleration (Eq. 16) forms of the dipole operator; only the velocity and acceleration results are presented here. Pseudoresonances in the double continuum are eliminated by performing a Gailitis average and by averaging the final spectrum over the size of the R-matrix box (Region I of Fig. 1). The ratio of double and single photoionization cross sections, a key parameter for characterizing electron correlations, is compared to existing theoretical and experimental values.

Methods that use a discrete representation of all possible excitation channels have enjoyed tremendous success at low energies where only single escape is energetically allowed [23]. Earlier theoretical attempts (before 1994) to calculate double photoionization relied on perturbative treatments of electron-electron interactions, such as many body perturbation theory. In this study, theoretical calculations of double photoionization cross sections are performed with a *nonperturbative* approach. While this approach also faces difficulties when applied to the escape of two electrons, it is informative to see results from a completely different formulation.

The implementation of our eigenchannel R-matrix approach starts from numerical

(closed-type) solutions of the one-electron radial Schrödinger equation for He^+, calculated inside the reaction volume subject to the boundary condition that the radial wavefunction vanishes at the boundary $r = r_0$. This generates a set of (closed-type) solutions having a discrete energy spectrum (see Fig. 2). In essence, we are limiting the Hilbert space to the set of eigenstates of our target state Hamiltonian in a *shrunken* eigenspace ($0 < r < r_0$). Virtually all methods today utilize some such set of shrunken eigenstates (see section 2.3). The lowest energy states (with principal quantum numbers $n \leq 3$) are very similar to the ordinary physical bound states of He^+, as they vanish at large distances anyway. For high n values, the spacing between energy levels is roughly proportional to n^2, characteristic of the energy spectrum for a square well potential. These solutions are next used to construct a two electron basis set. The two electron trial wavefunction at each final state continuum energy E is written as a linear combination of these basis functions, that now describes a continuum energy state. A variational method described elsewhere [23] is used to solve for the optimal coefficients in the basis set expansion of the trial wavefunction. We neglect exchange and correlation effects outside of the reaction volume.

If only closed-type one-electron orbitals were used to construct two-electron trial functions, no electrons would be able to escape from the reaction volume, since the wavefunction would be exactly zero everywhere on its surface. Accordingly, we also introduce "open-type" orbitals as in Ref. [125], defined as eigenfunctions of the He^+ Hamiltonian with nonzero values at $r = r_0$. These open-type orbitals are typically chosen to have nonvanishing derivatives at $r = r_0$. In this work, the open orbitals were determined by solving for eigenstates at specified energies; namely, the energies midway between the levels of the energy spectrum for the closed-type eigenstates. Each "channel" in our problem is represented by one closed-type state of He^+ for the "inner" electron, multiplied by each member of the complete set of closed-type basis functions for a given outer electron partial wave, and by two open-type basis functions for that partial wave as well. In this study, twenty-two closed-type

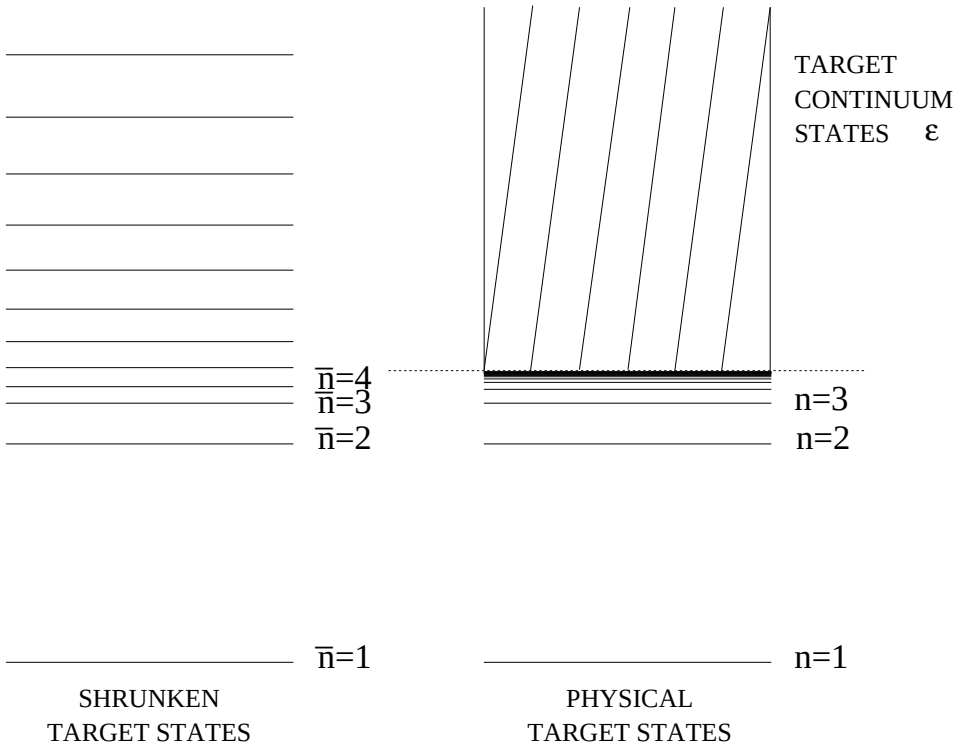

Figure 2. Comparison of the energy spectra of the eigenstates of the physical target state Hamiltonian with the eigenstates of the target state Hamiltonian in a shrunken configuration space. The physical target states consist of a Rydberg series and an infinite set of continuum states of energy ϵ, whereas only discrete states appear for the spectrum in the shrunken space. Note the good correspondence in energies for the lowest few states, as these physical states fit within the shrunken configuration space. This figure is taken from Ref. [31].

basis functions and two open basis functions are included for each channel.

In addressing two electron escape, one might suspect that we need to include products of two open-type orbitals. However, this is not the case. Inclusion of such product type basis functions would require a two-particle matching scheme with a wavefunction representing the motion of the two electrons outside of the reaction volume. The determination of an exact analytical expression for the three-body Coulomb continuum wavefunction remains an unsolved problem [44]. By selecting product basis functions in which the radial coordinate of at least one electron is zero on the surface of the reaction volume, we are able to employ the same one electron matching scheme used for describing single electron escape, provided we represent the wavefunction outside the reaction volume as a separable expression. In this outer region, wavefunctions are approximated by a linear combination of Coulomb functions with unit charge for the outer electron, multiplied by an He^+ eigenstate for the inner electron, followed by antisymmetrization. The channels included in the present photoionization calculations are $ns\epsilon p$, $np\epsilon s$, $np\epsilon d$, and $nd\epsilon p$. That is, we include two partial waves for the initial state and three partial waves for the final state. A numerical test showed that f-waves have a relatively minor effect on both the single- and double-photoionization cross sections. Approximately one thousand total two-electron configurations are used to describe the final states reached in single and double photoionization.

Previous applications of eigenchannel R-matrix methods have treated the escape of a single electron from the reaction volume (regions II and III in Fig. 1). The boundary conditions imposed by these calculations do not allow for the possibility of direct electron escape into the double continuum region of configuration space (region IV in Fig. 1). The eigenchannel R-matrix method is extended in this study to obtain double photoionization cross sections for helium, using a point of view similar to that applied by Robicheaux *et al.* [126] to the double continuum of $H + e^- + e^-$. We achieve this by reinterpreting the meaning of the remaining He^+ bound state electron in our single photoionization treatment,

despite the fact that we actually impose the same (single-escape) boundary conditions. The basic idea is to recognize that if the complete set of He^+ closed-type eigenfunctions in the R-matrix box are used to represent the "inner" electron in a close-coupling expansion, then those eigenfunctions that lie at positive energies (relative to the double escape threshold) must physically represent a (discretized) continuum state of He^+. Therefore, we interpret all flux escaping in such channels with positive energy thresholds as flux that contributes to double photoionization. Similarly, all flux escaping in channels at negative energies is interpreted as contributing to single photoionization, even for those negative energy He^+ box eigenstates which do not coincide with a physical He^+ eigenstate. Physically, this reflects our assumption that most of the photon's energy is absorbed by one of the electrons, leaving the He^+ ion in either a negative energy bound state or a discretized positive energy continuum state. Samson [34] has achieved some success using a model based on this qualitative picture. We will introduce a frame transformation in the next section as an improvement for distinguishing between the contributions to single and double photoionization.

One well-known [71] consequence of using a discrete spectrum of positive energy He^+ "ionization thresholds" is the appearance of pseudoresonances in the double ionization cross section. These pseudoresonances are an artifact of the artificial boundary conditions imposed on the finite reaction volume; they have no real physical meaning. It is desired to average out the effects of these pseudoresonances in the double continuum to obtain a smooth cross section. This can be accomplished by implementing Gailitis [127, 128] and box averaging techniques (the "box" is another term for the reaction volume). The Gailitis technique is useful for averaging over resonances near channel thresholds. The technique is easily implemented in the multichannel quantum defect theory (MQDT) portion of our calculation: we simply treat a weakly closed ionization channel (with $E_i > E$) as though it is open when solving the MQDT equations for the photoionization cross section. (Although closed channels are energetically forbidden at larger radial distances, they are included in our

calculation, as these channels still participate in the short-range physics.) In this analysis, Gailitis averaging is performed from 2 eV below each He^+ threshold all the way up to threshold. This automatically removes all or most of the Rydberg resonances converging to that particular ionization threshold (see Fig. 3). In order to average over box size, the cross sections are calculated for five different box sizes (reaction volume radii) in the range 10-12 atomic units, after which they are simply averaged to obtain the final cross sections reported here. These averaging techniques will be discussed further in the next section.

Calculations of double photoionization cross sections have been performed using the length, velocity, and acceleration dipole forms. The length form calculations give unreasonably high values of double photoionization cross sections for our R-matrix approach, while the results obtained using the velocity and acceleration forms are stable, consistent with each other, and in reasonable agreement with existing calculations. The length form weights the large-r part of the wavefunction the most, which is precisely where our unphysical boundary conditions probably cause our variational solutions to be the least accurate. Consequently, the large errors in the length form calculation might have been expected. However, single ionization calculations using all three dipole forms gave nearly identical results. We only report our velocity and acceleration results here. The averaged double photoionization cross sections obtained with these forms are shown in Fig. 4. There is a discrepancy of roughly 20% between the two calculated curves. The effects of pseudoresonances are barely visible in the small irregularities of the cross section profiles. These irregularities could presumably be eliminated by averaging over more box sizes, or by applying a convolution technique, as is discussed in the next section.

Considerable effort has been expended, both experimentally [34, 96, 129, 130, 131, 132, 133] and theoretically [33, 36, 37, 39, 116] to determine the ratio R of the single and double photoionization cross sections for helium in the intermediate photon energy range. Our calculated values for the ratio R are compared in Fig. 5 to several existing experimental and

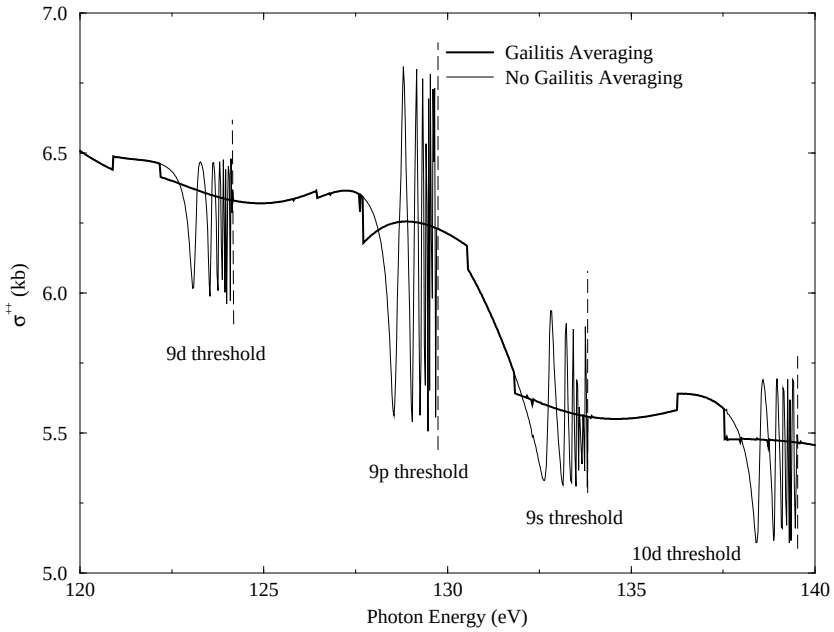

Figure 3. Helium double photoionization cross sections are shown for the case of Gailitis averaging (heavy line) and no Gailitis averaging (light line). In this analysis, Gailitis averaging is performed from 2 eV below each channel threshold up to threshold. The results shown in this figure were calculated with the velocity form of the dipole operator, and a box size of 12 a.u. was used.

theoretical values. The curve generated by Samson's simple classical model agrees well with the available experimental data, even though this model does not account for the symmetry of the final state reached in the photoionization process. The MBPT calculations of Carter and Kelly [36] and of Hino *et al.* [39] represent upper and lower limits on the theoretical values shown in Fig.5. These perturbative treatments of the electron-electron interaction are expected to have some shortcomings in this relatively low photon energy range. Our eigenchannel R-matrix results agree more closely with the results of Hino *et al.*, although the ordering of the velocity and acceleration form curves is reversed in these two sets of calculations. Pan and Kelly [134] have used another MBPT approach to calculate a maximum R value of almost 5%, which is somewhat larger than the maximum value obtained in both of our calculations. Proulx and Shakeshaft's [116] cross section calculations for photon energies in the range 80-140 eV agree well with our velocity form calculations. They also used their method to obtain values of the angular asymmetry parameter β that are in good agreement with experimental measurements, indicating that their adopted analytical form for the final state wavefunction may have some merit. Our results are slightly smaller than the experimental values shown in Fig. 5. This discrepancy is comparable to our theoretical "error bar," which we take to be the difference between our velocity and acceleration form calculations.

It may not be obvious why the present approach of imposing artificial boundary conditions at $r = r_0$ should accurately represent the flux leading to double-ionization. In particular, we initially neglect the wavefunction in region IV of Fig. 1. However, our reinterpretation of positive energy partial cross sections allows the inner electron to eventually escape to infinity through region IV. By describing nonperturbatively the electron correlation and exchange effects within the reaction volume (region I), we attempt to accurately describe the initial outward propagation of the electron pair that is induced by the photon absorption. The electrons are mutually deflected as they escape to infinity beyond the reaction zone, and

this deflection is not properly described by our approach, but we nevertheless expect the amount of flux leading to double escape will not differ widely from our calculated values. However, as we do not accurately describe the physics of the two electron escape beyond the reaction volume, we cannot expect our current approach to give a realistic description of other details of the double photoionization process such as the photoelectron distributions in energy and angle. However, an improved version of the approach discussed in Chapter 4 may be able to accurately provide at least some details of two electron escape processes.

In summary, a new approach was developed to calculate double photoionization cross sections of helium. We extended the R-matrix method by reinterpreting the meaning of discrete He^+ states that have positive energy eigenvalues. Gailitis and box averaging techniques were used to obtain smooth cross sections, minimizing the effects of the artificial pseudoresonances. Although a discrepancy in the ratio of double and single photoionization exists between our calculations and experimental results, this discrepancy was comparable to the uncertainty in our results. We will return to this problem in Chapter 4.

3.2 Simplified Model of Electron Scattering

In order to better test the accuracy of wave functions obtained with our previous approach to helium double photoionization, we applied the eigenchannel R-matrix method to describe electron impact ionization processes, where two electron escape arises from the arrival of an energetic electron rather than a photon. A simplified model of electron scattering, called the Temkin-Poet model, was adopted for two reasons: to simplify the numerical calculations, and to allow a comparison with other highly accurate numerical results obtained with the convergent close-coupling (CCC) approach. Since the CCC method has been successfully applied to many different systems (see section 2.3), comparison of this method with our R-matrix calculations provided a more conclusive test of the accuracy of our method than was possible for the case of helium double photoionization. As illustrated in Fig. 5, there was no consensus in 1994 as to the proper values of the ratio of double and single

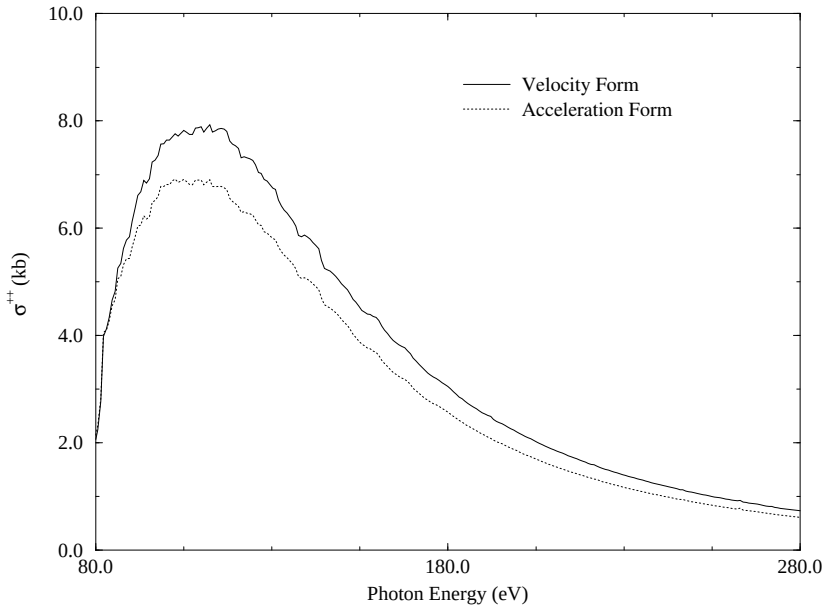

Figure 4. The averaged double photoionization cross section calculated for helium is shown as a function of photon energy. The solid curve represents calculations performed with the velocity dipole form, while the dotted curve represents calculations performed with the acceleration dipole form. This figure is taken from Ref. [28].

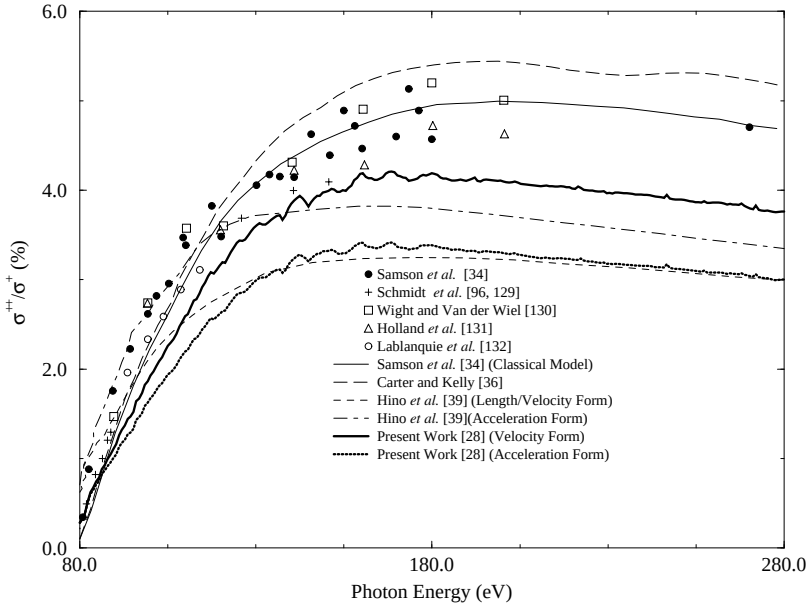

Figure 5. The ratio of double and single photoionization cross sections of helium is shown versus the photon energy (status as of 1994). The individual symbols represent experimental measurements, while the lines represent theoretical calculations. A plot of this ratio for more recent experimental and theoretical values is given in Fig. 16. This figure is taken from Ref. [28].

photoionization for helium in the intermediate photon energy range. Consequently, we were unable to clearly evaluate the accuracy of our method when applied to this particular case of two electron escape. A direct evaluation of our previous results was further complicated by the discrepancy between calculations using the various forms for the dipole operator. Since the final state dynamics in electron impact ionization are very similar to those in helium double photoionization, an application of our method to describe electron scattering provided an equally challenging but more informative test.

3.2.1 Discussion of the Temkin-Poet Model Ionization of hydrogen by electron impact represents one of the simplest two electron escape processes. Accurate calculations of ionization cross sections for this process have only recently been achieved [27]. Earlier attempts to address this problem included the adoption of a simplified model of electron scattering proposed by Temkin in which all non-zero orbital angular momenta are neglected [135]. That is, the hydrogen atom is treated as though it only has s states, and the total angular momentum of the electron-hydrogen system is set to zero. This model was later studied in much greater detail by Poet [136, 137]. We will denote this model as the Temkin-Poet (TP) model. Although the application of this oversimplified model to the real e-H system is quite limited, it does provide a nontrivial test of the accuracy of double continuum wave functions. As an example of its limited applicability, the TP model generates incorrect behavior in the ionization cross section near threshold. A simplified model that provides a more realistic description of threshold behavior was introduced by Peterkop. Peterkop's model [87], which replaces $1/r_{12}$ by $1/(r_1 + r_2)$, does generate the correct threshold law (Wannier exponent) for double escape [88]. However, we do not consider the more realistic Peterkop model in this study, as accurate results are only currently available for comparison with the TP model.

The Schrödinger equation for the TP model can be solved "exactly". Its replacement of the electron-electron interaction term by $1/r_>$ (the first term in the usual multipole

expansion of $1/r_{12}$) leads to a separable partial differential equation. However, the boundary conditions are not separable. Poet used an interpolation technique to obtain bound state excitation cross sections. Calculations of the ionization cross section for the TP model is a nontrivial exercise, as the presence of nonseparable boundary conditions requires numerical solution of an integral equation. Callaway and Oza [138] obtained a rough estimate of the ionization cross section for this model by combining information about the total cross section (given by the optical theorem) with calculated excitation cross sections for the lowest three bound states. Since accurate bound state excitation cross sections are known for the TP model, this model is often used to test other methods [53, 60, 76, 82, 126, 139, 140, 141, 142, 143].

3.2.2 R-matrix Application to Electron Scattering We now apply our R-matrix method to address electron scattering, and compare our results with those obtained using the CCC approach [29]. The CCC method has been previously applied to the TP model for e-H scattering [142]. Extensive data has been tabulated for this case in Ref. [144]. In addition to addressing e-H scattering in the TP model, we also investigate e-He^+ scattering for this simplified model. To the best of our knowledge, results for the TP model of e-He^+ scattering have not previously been reported. Yet the TP model should be even simpler to apply to e-He^+ scattering than to e-H scattering, as the dominant electron-electron correlations are more spatially confined for this case. Nonetheless, the e-He^+ model provides a nontrivial test case for describing two electron escape. Also, the effect of pseudoresonances are more prominent in the e-He^+ system due to the presence of the long-range Coulomb attraction.

To explicitly describe the matching scheme adopted, a particular solution of the spatial part of the two-electron wavefunction can be expressed as

$$\psi_\beta = \mathcal{A} \sum_i \Phi_i(r_<) F_{i\beta}(r_>), \tag{22}$$

with a corresponding normal derivative

$$\frac{\partial \psi_\beta}{\partial r_>} = \mathcal{A} \sum_i \Phi_i(r_<) F'_{i\beta}(r_>). \tag{23}$$

Here β represents an index that distinguishes different independent solutions at the specified energy E, $\mathcal{A}$ is the antisymmetrization operator, i is a channel index, and $r_<$ and $r_>$ represent the radial distances of the "inner" and "outer" electron from the nucleus. (Note that the antisymmetry operator acts on the total wavefunction, with the form of the spatial wavefunction after antisymmetrization given by Eq. 81. For the $S = 0$ singlet case considered here, the spatial wavefunction is symmetric.) Analogous to the case of double photoionization of helium, the spatial part of the wavefunction is represented as a linear combination of two-electron orbitals:

$$\psi = \mathcal{A} \sum_{nn'} C_{nn'} \phi_{ns}(r_1) \phi_{n's}(r_2). \tag{24}$$

In our formulation, one summation (over n) includes only closed-type orbitals (representing the "inner" electron), while the other summation (over n') includes two open-type orbitals in addition to the same number of closed-type orbitals. That is, our two-electron basis consists of configurations that are products of the closed-closed or closed-open type. Therefore, the "inner" electron orbital can always be factored out, reducing Eq. 24 to the form of Eq. 22. Consequently, the matching of the two-electron wave function across the reaction volume is reduced to a matching of the "outer" electron radial wave function only. Antisymmetrization of our wavefunction (see Fig. 1) allows the matching to be imposed either at $r_1 = r_0$ as a function of r_2 (r_1 representing the "outer" electron), or at $r_2 = r_0$ as a function of r_1 (r_2 representing the "outer" electron). The values of $F_{i\beta}(r_>)$ and its derivative are numerically determined inside the reaction volume. Outside the reaction volume, the exact form of $F_{i\beta}(r_>)$ depends on the nature of the scattering target, or more precisely, on the field of the effective charge that the "outer" electron experiences as it leaves the reaction volume. The general asymptotic form for the spatial part of the energy-normalized wave function with an

electron in incoming channel i' is given by

$$\psi_{i'} = \mathcal{A}\sum_i \Phi_i(r_<)\frac{1}{\sqrt{2\pi v_i}}\left[f_i^+(r_>)S_{ii'} - f_i^-(r_>)\delta_{ii'}\right], \tag{25}$$

where $f_i^{\pm}$ are the outgoing and incoming wave solutions for the radial Schrödinger equation of the outer electron in channel i. The factor $1/\sqrt{2\pi v_i}$, where v_i is the speed of the outermost electron, is required to ensure that $|S_{ii'}(E)|^2$ represents the ratio of the outgoing radial probability flux in channel i to incoming radial probability flux in channel i' [23]. For e-He^+ scattering at energies sufficiently high, the "outer" electron can be approximated by a linear combination of unit charge Coulomb functions, as in helium double photoionization:

$$\psi_{i'} = \mathcal{A}\sum_{i=1}^{N} \Phi_i(r_<)[f_i(r_>)\delta_{ii'} - g_i(r_>)K_{ii'}], \;\; r_> > r_0, \tag{26}$$

where $f_i(r_>)$ and $g_i(r_>)$ are the regular and irregular Coulomb functions, and $K_{ii'}$ is the reaction matrix. For the case of e-H scattering in the TP model, however, the "outer" electron does not experience a Coulomb charge. Therefore, the radial solution in each channel is represented by a linear combination of spherical Bessel functions. The coefficients of this linear combination (and therefore the scattering matrix) can then be obtained by matching the wave functions and normal derivatives at the surface of the reaction volume,

There are several other differences in e-H and e-He^+ scattering. The main difference is the deeper Coulombic core of the He^+ target. Consequently, the maximum e-He^+ ionization cross section is more than a factor of ten smaller than the e-H ionization cross section. Since the hydrogen bound wave functions extend roughly twice as far in space as the He^+ bound wave functions, the reaction volume used for e-H scattering is roughly twice as large as that used for e-He^+ scattering. Consequently, for a given r_0 and an identical basis set size, convergence of the basis set begins to deteriorate at a lower energy for e-H scattering. However, the maximum cross section for e-H scattering occurs at a lower energy. Due to the absence of long-range interactions in the TP model of e-H scattering, multichannel quantum defect theory (MQDT) is not needed, as weakly-closed channels generate no

Rydberg manifolds. For the actual case of e-H scattering (in contrast to the TP model), a long-range dipole interaction between the outgoing electron and the degenerate hydrogen (bound state) core is also present. MQDT can be implemented to treat this case and obtain bound state excitation cross sections efficiently [145]. The existence of a long-range Coulomb potential between the outgoing electron and the core motivates our use of MQDT for the case of e-He^+ scattering. The physical scattering matrix S_{ij} can be obtained from Eqs. 17-22 in Ref. [146]. The cross section is given by

$$\sigma_{j\to i} = \frac{\pi}{k_j^2}\frac{2S+1}{4}|S_{ij} - \delta_{ij}|^2, \tag{27}$$

where the indices j and i refer to the incoming and outgoing electron channel states, $k_j = \sqrt{2(E-E_j)}$ denotes the asymptotic wave number of the incoming electron, and S denotes the total spin of the system. (Note that we have ignored the Coulomb phase shift here for the case of e-He^+ elastic scattering. This was done for the present purposes of comparison.)

3.2.3 Averaging Techniques In order to calculate physical cross sections using the R-matrix approach, a method must be adopted to express the physical scattering matrix, with incoming and outgoing electron channels corresponding to the true physical hydrogenic eigenstates, in terms of our calculated "box" scattering matrix, which has incoming and outgoing electron channels corresponding to the "box" hydrogenic eigenstates (sometimes referred to as "pseudostates"). Fig. 6 shows the energies of the lowest closed-type box states of He^+ as functions of box size. These discrete states (which represent the "inner" electron) can have both positive and negative energies, since the radial wave functions are forced to be zero at the surface of the reaction volume instead of at infinity. An energy spectrum of these box states for a single box size is shown in Fig. 2. Imposing boundary conditions at the box radius leads to box state energies that are dependent on the box size (the size of the reaction volume), as shown in Fig. 6.

In the previous application to helium photoionization, the double escape cross sections calculated with the eigenchannel R-matrix approach were obtained simply by summing

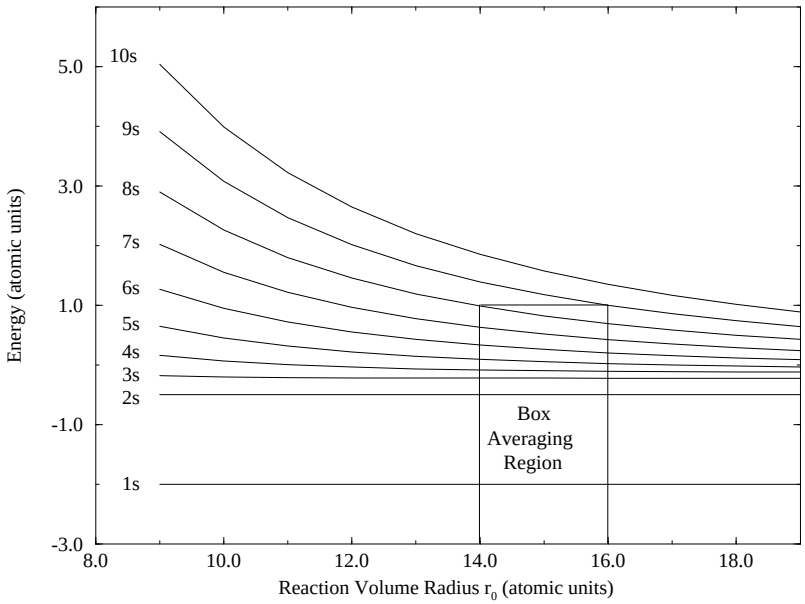

Figure 6. Energy dependence of He^+ box states as a function of box size (size of the reaction volume). This figure is taken from Ref. [29].

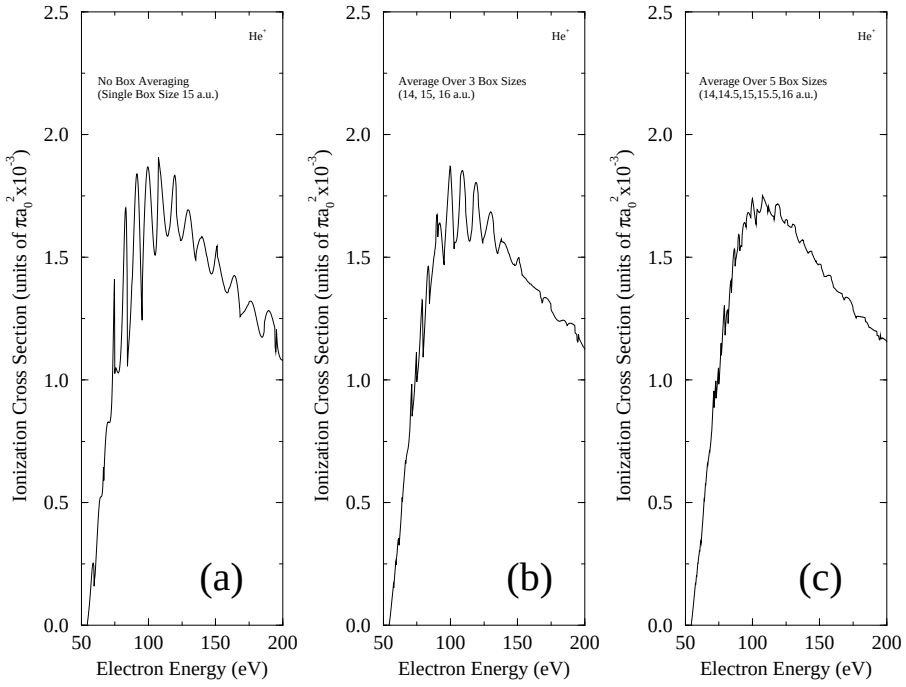

Figure 7. Singlet ionization cross sections for the Temkin-Poet model of electron-He^+ scattering using (a) a single box size, (b) an average over three box sizes, and (c) an average over five box sizes. The frame transformation was also used to obtain these results. This figure is taken from Ref. [29].

over all discrete states with a positive energy. That is, we considered a box channel with an energy just above threshold as contributing entirely to ionization and a channel with an energy just below threshold as contributing entirely to bound state excitation. However, each box channel actually possesses both bound and continuum properties. Since the energies of the box states depend on the size of the reaction volume, the number of ionization channels included changes discontinuously with box size. However, errors associated with our discretization of the continuum should cancel out if the final spectra are averaged over a proper range of box sizes.

To implement box averaging, cross sections are generated with several different box sizes, then simply averaged to obtain the final cross section. This averaging procedure helps to eliminate artificial pseudoresonances that would otherwise appear in the continuum, and produces a much smoother and more realistic ionization cross section. The pseudoresonances that appear in the ionization spectrum have no physical significance. Rather, they are simply an artifact of our discretized continuum. These pseudoresonances are essentially due to probability flux entering the series of Rydberg states attached to each box state in the continuum, occurring near the energies of these box states (see Fig. 3). The range of box sizes over which to average is normally chosen such that a particular box state for the smallest box size has approximately the same energy as the next higher state (next higher principal quantum number) for the largest box size (see Fig. 6). This required range Δr of box sizes actually depends on the energy range, as higher states will have a larger energy spacing $\partial E/\partial n$ for a fixed box size (see Figs. 2 and 6). The range Δr also depends on the average box size for which the calculations are performed. For example, with larger box sizes, the rate of the energy shift with box size $\partial E/\partial r_0$ decreases more slowly for any particular state (see Fig. 6). Since the higher energy levels can be approximated by those of a particle in a one-dimensional square well, the box averaging range Δr will be roughly proportional to the inverse of the square root of the energy of the state being targeted for the averaging. This

result follows from performing a first order Taylor expansion of the energy:

$$E(n_1, r_1) = E(n_0, r_0) + (n_1 - n_0)\frac{\partial E}{\partial n}\bigg|_{n_0} + (r_1 - r_0)\frac{\partial E}{\partial r}\bigg|_{r_0}, \tag{28}$$

where $E(n_0, r_0)$ is the energy of the box state with principal quantum number n_0 and box size r_0, and $E(n_1, r_1)$ is the energy of the box state with principal quantum number $n_1 = n_0 + 1$ and box size r_1. Applying the criterion of equal energies and solving for $\Delta r = r_1 - r_0$ gives the condition for the required range of box sizes:

$$\Delta r \simeq \left(-\frac{\partial r_0}{\partial E}\right)\left(\frac{\partial E}{\partial n_0}\right). \tag{29}$$

For a one-dimensional box of width r_0, $E(n_0, r_0) = C(n_0^2/r_0^2)$ is the energy of the nth state, where C is a constant of proportionality. Applying Eq. 29 for this case, Δr is found to be proportional to the inverse square root of the targeted energy E. By including a sufficient number of box sizes and averaging over the proper range, a smooth and reliable cross section can be obtained.

Other competing factors must be considered to determine the optimal set of box sizes over which to average. First of all, the box needs to be large enough to include significant electron-electron correlations. In practice, this can be tested by varying the box size and observing the stability and convergence of the cross sections. At the same time, convergence with respect to basis set size will deteriorate as the box size is increased. Consequently, the box size must be kept small enough to give accurate cross sections over the desired projectile energy range. Again, this can in practice be easily tested by varying the basis set size until convergence is achieved. The energy range we have targeted here to obtain the most accurate cross sections is near the maximum of the ionization cross section. The range Δr of box sizes was then determined by selecting a box state with this energy and applying the criteria used to obtain Eq. 29. The effect of box averaging is illustrated in Fig. 7. The ionization cross sections are shown for a single box size, an average over three box sizes, and an average over five box sizes. The effect of the pseudoresonances is hardly noticeable for the average

over five box sizes. By averaging over a larger number of box sizes, an even smoother cross section can be obtained.

For e-He^+ scattering, a Gailitis averaging technique is also performed in order to remove the infinite number of Rydberg pseudoresonances near each ionization threshold (see Fig. 3). This technique was used previously to calculate helium double photoionization cross sections. The Rydberg series of pseudoresonances can be interpreted as a set of standing waves. Each such wave is a superposition of outgoing flux and incoming flux that has been reflected by a Coulomb barrier in a closed channel far beyond the surface of the reaction volume. The main idea of Gailitis averaging is to treat the closed channels (channels for which $E_i > E$) lying just below threshold (for our calculations, this procedure was applied to channels from 2 eV below threshold up to threshold) as being open in the multichannel quantum defect theory (MQDT) part of the calculation. As a result, in this energy region there is no probability flux reflected (unphysically) inward. Therefore, the Rydberg series of pseudoresonances is eliminated.

In addition to eliminating pseudoresonances, the box averaging technique roughly averages out errors associated with treating box states as contributing entirely to ionization or to bound state excitation. However, we will now develop an improvement which gives the ionization cross sections to reasonably good accuracy even before any box averaging is performed. This is accomplished with a frame transformation, which is described below.

3.2.4 Frame Transformation A projection technique which relates pseudostate excitation cross sections to the ionization cross section was originally introduced by Gallaher [147], and later adopted by Callaway and Oza [51], and by Bray and Stelbovics [27]. Let $|n\rangle$ represent a physical hydrogenic bound state and $|\overline{n}\rangle$ represent a box hydrogenic state. Gallaher adopted the following formula to calculate the ionization cross section:

$$\sigma_I(E) = \sum_{\overline{n}} \left(1 - \sum_n |\langle n|\overline{n}\rangle|^2\right) \sigma_{\overline{n}}(E), \tag{30}$$

where $\sigma_{\overline{n}}$ are box state excitation cross sections and σ_I is the desired "true" ionization cross section. The quantity in large parentheses in the above formula can be interpreted as the difference between the total cross section and the bound state excitation contributions to the cross section. Alternatively, this formula can be interpreted as the fraction of the $\overline{n}$-th box state which is composed of true continuum wave functions.

The frame transformation method presented here is somewhat similar to Gallaher's method. However, we directly transform the box state scattering matrix amplitudes instead of the box state excitation cross sections. By transforming amplitudes rather than probabilities, our approach is closer in spirit to frame transformation methods, which have been successfully applied to many problems [146, 148, 149]. We first introduce an analog of Gallaher's technique, and then proceed to develop an alternate method to calculate ionization cross sections. We start by defining a relationship between the physical (bound-bound) scattering matrix $S^{phys}_{nn'}$ and the box scattering matrix $S^{box}_{\overline{n}\overline{n}'}$:

$$S^{phys}_{nn'} = \sum_{\overline{n}\overline{n}'} \langle n|\overline{n}\rangle S^{box}_{\overline{n}\overline{n}'} \langle \overline{n}'|n'\rangle. \tag{31}$$

Here n and n' denote physical bound states of the target, whereas $\overline{n}$ and $\overline{n}'$ represent the closed-type box states representing the "inner" electron in the scattering process.

We will only investigate electron scattering from the ground state ($n' = 1$) of the target here. Since the radial wavefunctions of the lowest two physical states (the $1s$ and $2s$ states) fit inside our reaction volume, the scattering matrix elements of interest for calculating the desired bound state excitation cross sections are given by

$$S^{phys}_{n1} = \sum_{\overline{n}} \langle n|\overline{n}\rangle S^{box}_{\overline{n}1}. \tag{32}$$

Here we have used the fact that the closed-type box states form a complete orthonormal basis since they satisfy the same Schrödinger equation and boundary conditions. The elastic scattering cross section and the inelastic cross section $\sigma_{1s\to 2s}$ can be calculated directly from Eq. 27, as the matrix elements S_{11} and S_{21} are nearly identical to $S_{\overline{1}1}$ and $S_{\overline{2}1}$. Ionization

cross sections and excitation cross sections for higher bound states can be calculated by using the frame transformation technique that is described below. Although our physical S-matrix is not exactly unitary (the largest error in unitarity that we have observed is about 0.2%), deviations from unitarity do not significantly affect our results. Assuming unitarity, the ionization cross section is given by

$$\begin{aligned} \sigma_I &= \frac{\pi}{k_1^2}\frac{2S+1}{4}\left(1-\sum_{n=1}^{\infty}|S_{1n}^{phys}|^2\right) \\ &= \frac{\pi}{k_1^2}\frac{2S+1}{4}\left(1-\sum_{n=1}^{\infty}|\sum_{\overline{n}=1}^{\overline{n}_{max}}\langle n|\overline{n}\rangle S_{1\overline{n}}^{box}|^2\right). \end{aligned} \tag{33}$$

Obviously, this infinite sum over n can not be explicitly evaluated numerically, but rather must be truncated at some finite n. Numerical tests have shown that the sum over n converges slowly, thus requiring a relatively large number of terms to approach a converged answer.

Rather than pursuing the approach based on Eq. 33, we develop an alternative expression for the ionization cross section by introducing the *physical* hydrogenic continuum states (Coulomb functions), which are energy normalized over the infinite radial domain $0 \le r < \infty$. We extend the frame transformation (Eq. 31) to relate continuum elements of the physical scattering matrix to our box scattering matrix elements:

$$S_{\epsilon 1}^{phys} = \sum_{\overline{n}}\langle\epsilon|\overline{n}\rangle S_{\overline{n}1}^{box}, \tag{34}$$

where $|\epsilon\rangle$ represents a physical energy-normalized continuum state at energy ϵ for the inner hydrogenic electron. The ionization cross section is then given by

$$\begin{aligned} \sigma_I &= \frac{\pi}{k_1^2}\frac{2S+1}{4}\int_0^E d\epsilon\left|S_{\epsilon 1}^{phys}\right|^2 \\ &= \frac{\pi}{k_1^2}\frac{2S+1}{4}\int_0^E d\epsilon\left|\sum_{\overline{n}}\langle\epsilon|\overline{n}\rangle S_{\overline{n}1}^{box}\right|^2. \end{aligned} \tag{35}$$

The transformation factor $\langle\epsilon|\overline{n}\rangle$ determines the fraction of the box state $\overline{n}$ which will contribute to the ionization cross section at the continuum energy ϵ. A plot of $|\langle\epsilon|\overline{n}\rangle|^2$ as a

function of the inner electron continuum energy ϵ is shown in Fig. 8 for $\overline{n}$=5 and $\overline{n}$=9 (the $\overline{n}$=9 curve has been multiplied by a factor of two so it can be seen on the same graph). These curves were generated for e-He^+ scattering with a box size of $r_0 = 16.5$ atomic units. The profile of the plot is similar to the familiar function $[\sin(x)/x]^2$. In the limit of an infinite reaction volume, the transformation elements approach Dirac delta functions, in which case the physical and box cross sections become identical. For the size of the reaction volume shown, the $\overline{n} = 5$ state has an energy just above the ionization threshold. The maximum of the frame transformation factor occurs at the box state energy of $\overline{n}$. In our previous formulation (and application to helium photoionization), this channel would be interpreted as contributing entirely to ionization. However, from Fig. 8, one observes that a significant portion of the flux in this channel (nearly half) will contribute to the excitation cross sections of high bound states. The zeros of the transformation factor occur precisely at the energies of the other box states, owing to their orthogonality. Apart from a normalization factor, the closed-type box states are proportional (for $r < r_0$) to the physical continuum states, but only at those discrete energies for which the continuum wave function happens to vanish at the surface of the reaction volume.

In practice, the efficiency of our method for calculating the frame transformation matrix is greatly enhanced by employing the identity

$$\langle u_{\overline{n}} | u_\epsilon \rangle = \frac{W(u_\epsilon, u_{\overline{n}})|_{r_0}}{2(\epsilon - \epsilon_{\overline{n}})}. \tag{36}$$

Here $u_{\overline{n}}$ represents the box state radial wave function multiplied by r, u_ϵ represents the continuum hydrogenic radial wave function multiplied by r, $W(u_\epsilon, u_{\overline{n}})|_{r_0}$ is the radial Wronskian evaluated at $r = r_0$, ϵ is the energy of the continuum state, and $\epsilon_{\overline{n}}$ is the energy of the box state. This identity is easily derived by manipulating the box and continuum state radial Schrödinger equations. The greatest changes observed in our cross sections when the frame transformation technique is implemented (in comparison to our previous method) occur for box sizes in which the energy of one box state is very near threshold. For this case,

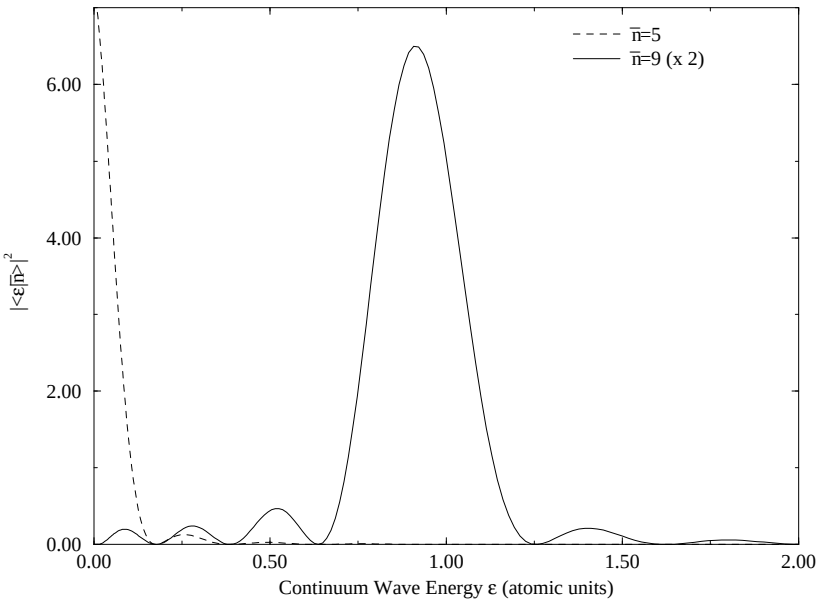

Figure 8. Plot of the square of the transformation factor used in the projection technique as a function of the continuum wave energy. The dashed line corresponds to a box state of $\overline{n} = 5$, while the solid line corresponds to a box state of $\overline{n} = 9$. The $\overline{n} = 9$ state has been multiplied by a factor of 2 so it can be seen more easily on the same graph. This figure is taken from Ref. [29].

the frame transformation gives roughly an equal contribution to the bound state excitation and ionization cross sections for that particular near-threshold channel. An example of this situation is shown in Fig. 9(a), where the ionization cross section for the TP model of electron-He^+ is plotted with and without a frame transformation for box sizes of 16.5 and 17 atomic units. For a box size of 16.5 atomic units, a box state lies just above threshold. If no frame transformation is implemented, this channel would be treated as contributing entirely to the ionization cross section, and as a result the ionization cross section would be overestimated. For a box size of 17 atomic units, the box state now lies just below threshold. Since this channel would be treated as contributing entirely to the bound state excitation cross section, the ionization cross section would be underestimated. When the frame transformation is implemented, the proper ionization and bound state excitation contributions are projected out, giving a nearly identical ionization cross section profile for both box sizes. Use of a frame transformation to calculate results which are independent of box size (along with a convolution technique to be described shortly) provides an efficient alternative to box averaging for obtaining stable cross sections. This technique significantly reduces the number of computations required, since results can now be obtained by simply performing an R-matrix calculation with a single box size.

An energy convolution technique has been introduced to improve the smoothness of cross sections shown in Fig. 9(a). A typical ionization cross section profile for a single box size before the convolution approach is performed is illustrated in Fig. 7(a), with the large oscillations reflecting the presence of pseudoresonances. The convolution function used to obtain the smooth profiles in Fig. 9(a) was a Gaussian function of variable width. We allowed the width of the Gaussian to scale as dE/dn, since this factor describes the energy spacing between pseudoresonances (for our approximation of a particle in a one-dimensional square well, $dE/dn \propto \sqrt{E}$). This approach forces a Gaussian of zero width to be used at threshold, so that the convolved ionization cross section is ensured to vanish at threshold

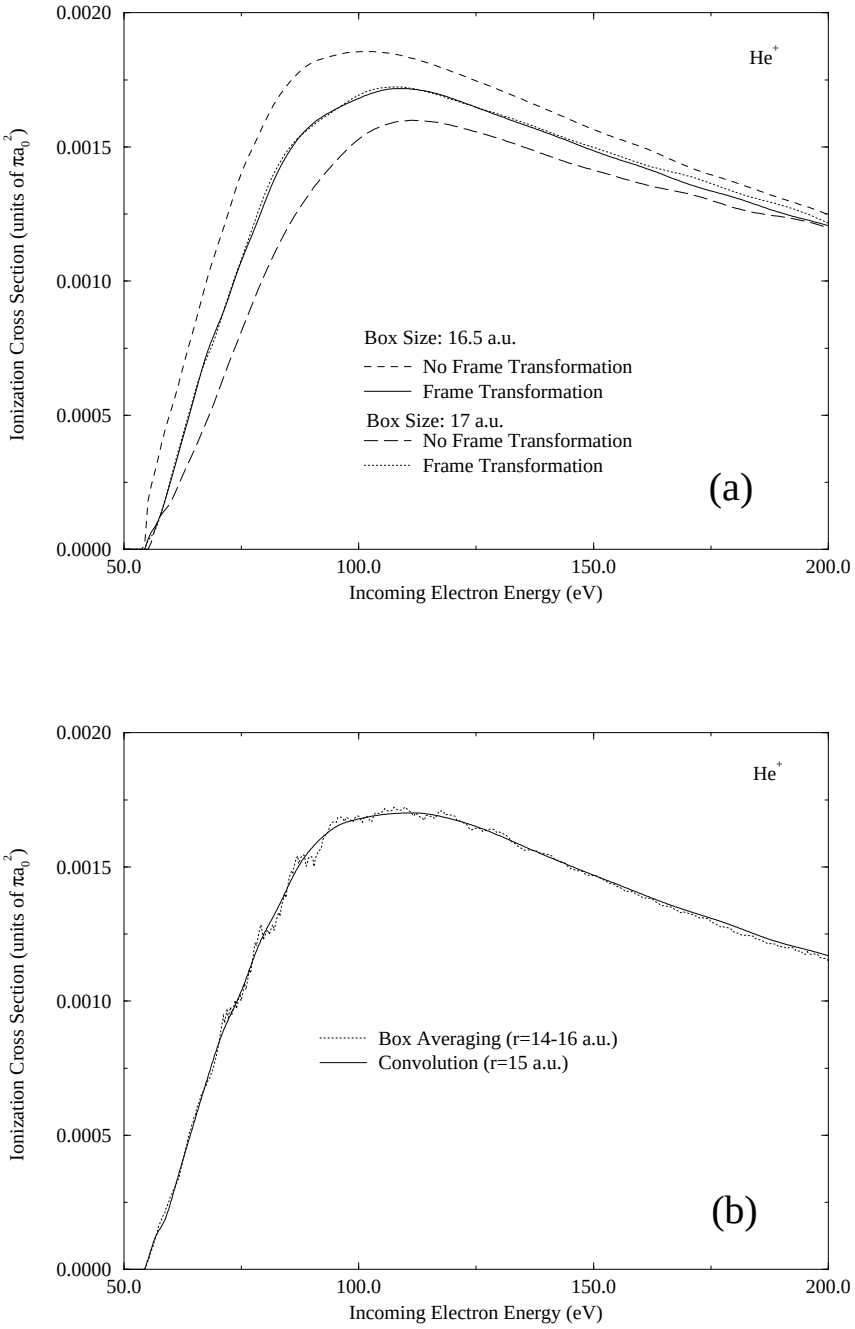

Figure 9. Illustration of the frame transformation and convolution methods to obtain reliable cross sections. Singlet ionization cross sections for the Temkin-Poet model of electron-He^+ scattering (a) using box sizes of 16.5 and 17 a.u.: the dashed and long-dashed lines represent the cross sections obtained without using a frame transformation, while the solid and dotted lines represent the cross sections obtained when a frame transformation is implemented, and (b) using an average of nine box sizes in the range of 14 to 16 atomic units, shown by the dotted line, and a convolution of a single box size of 15 a.u., shown by the solid line. These figures are taken from Ref. [29].

(in contrast to a fixed-width energy convolution). Fig. 9(b) shows a comparison of box averaging of ionization cross sections over nine box sizes from 14 to 16 a.u., and a frame transformation and convolution applied to a single box size of 15 a.u. (at the midpoint of the range of box averaging). The frame transformation/convolution approach generates essentially the same magnitude of the ionization cross section as obtained by box averaging, but with a much smoother profile. Furthermore, the number of required calculations is reduced by a factor of nine (the number of box sizes). Although the convolution approach has been useful in obtaining the results presented here, this technique should be used with prudence, since both physical and unphysical resonances will be broadened or else eliminated altogether. This is not a concern here, as no physical resonances occur above the threshold. More generally, double continuum cross sections obtained with the R-matrix technique may contain both physical and unphysical resonances. For example, double photoionization of a heavier atom such as Ar is known to produce resonances embedded in double continua. Box averaging should be used rather than the convolution approach for such cases in order to ensure that only artificial pseudoresonances are eliminated, with the "true" resonances remaining unaffected.

3.2.5 Application to e-H and e-He^+ Scattering In the current study, up to 46 closed and two open orbitals per channel have been included in an R-matrix calculation of e-H scattering within the TP model. Fig. 10 shows a comparison of the singlet cross sections obtained by the CCC approach and by the eigenchannel R-matrix method for both the elastic and inelastic $1s-2s$ cross sections. The two methods agree to within 3% for these cross sections. The circles in the figure denote "exact" solutions of the TP model which were calculated numerically [138, 141]. The energy range shown for the incoming electron is 10-50 eV for the CCC approach, while results from the ionization threshold (13.60 eV) to 50 eV are shown for the R-matrix approach. A basis set of 30 Sturmian functions was used to generate the CCC results. The R-matrix results were obtained by averaging over

five different box sizes from 24 to 28 atomic units. Although this averaging procedure did not significantly change the results obtained for bound state excitation cross sections, it is required to eliminate artificial pseudoresonances and to obtain a smooth ionization cross section. The frame transformation technique described earlier is not required to generate accurate elastic and $1s-2s$ inelastic cross sections, as the reaction volume is large enough to contain the physical $1s$ and $2s$ wave functions of hydrogen.

Fig. 11 shows a comparison of the elastic and $1s-2s$ inelastic cross sections for the case of singlet e-He^+ scattering in the TP model. A basis set size of 30 Sturmian functions was again used to generate the CCC results. Up to 34 closed and two open orbitals per channel were used to generate the R-matrix results. The R-matrix cross section was averaged over nine different box sizes ranging from 14 to 16 atomic units. Again, the two methods agree to within 3% over most of the energy range.

Figs. 12 and 13 show the TP model singlet ionization cross sections for electron scattering of both hydrogen and He^+ targets. The same basis set sizes and averaging technique used to obtain the bound state excitation cross sections were adopted to obtain the ionization cross sections. In addition, the frame transformation method, as given by Eq. 35, was used to generate the R-matrix results, and a convolution of the box averaged cross section was performed to obtain a smooth profile. The circles in Fig. 12 no longer represent the "exact" solutions of the TP model, but rather a complicated interpolation calculated by Callaway and Oza [138]. These interpolated values agree closely with the CCC results. The agreement between CCC and the R-matrix approach is also fairly good, especially for incoming electron energies larger than 30 eV, where the agreement is better than 10%. However, the R-matrix results are up to 70% smaller than those generated with the CCC approach in the lowest energy range. We have less confidence in our R-matrix treatment at lower energies, since our approximation of neglecting electron-electron correlations outside the reaction volume is expected to break down in this energy range. The CCC approach is

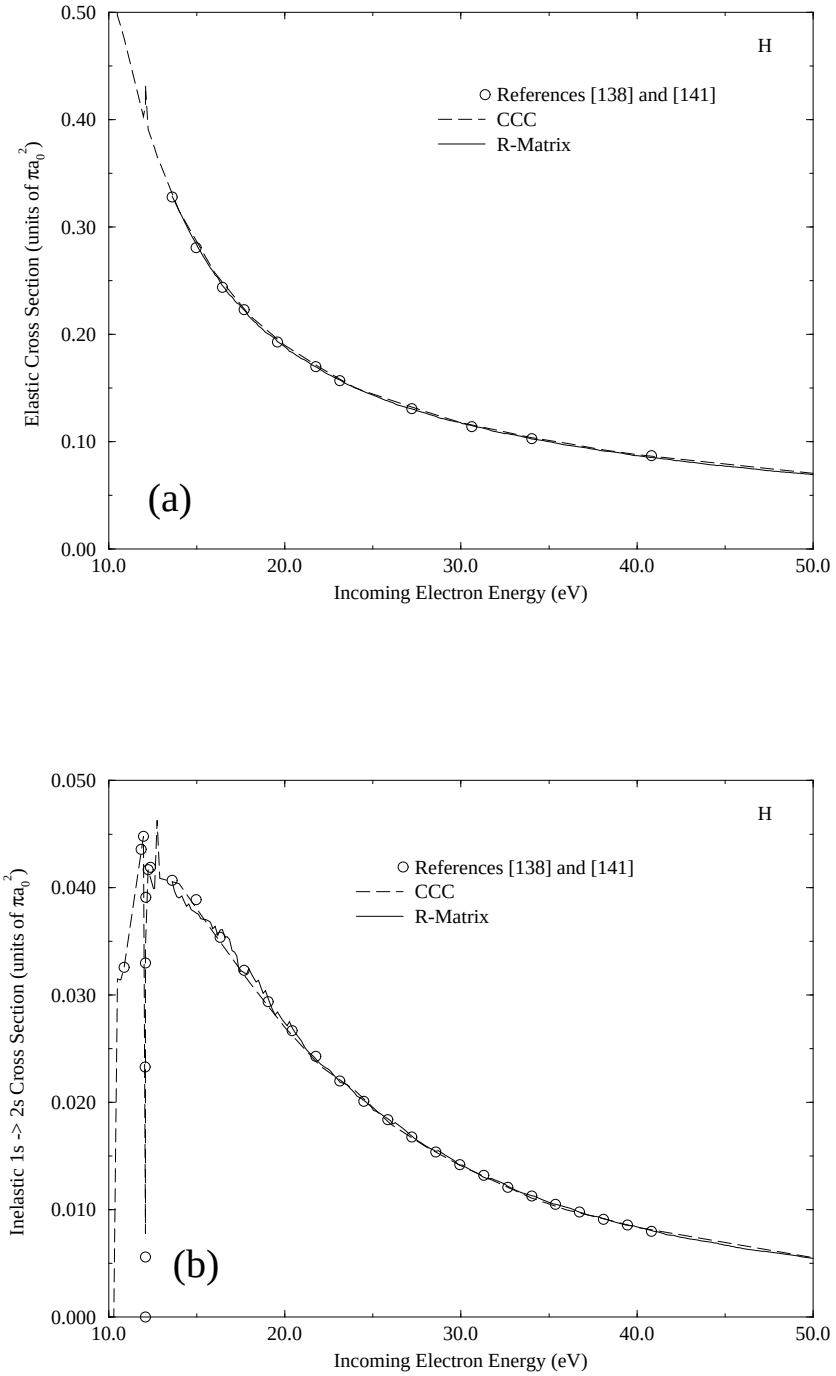

Figure 10. Singlet elastic and inelastic $1s - 2s$ cross sections for the Temkin-Poet model of electron-hydrogen scattering. The values for the exact results, denoted by open circles, are taken from references [138, 141]. The dashed line represents calculations performed with the CCC approach, while the solid line represents calculations performed with the R-matrix technique. These figures are taken from Ref. [29].

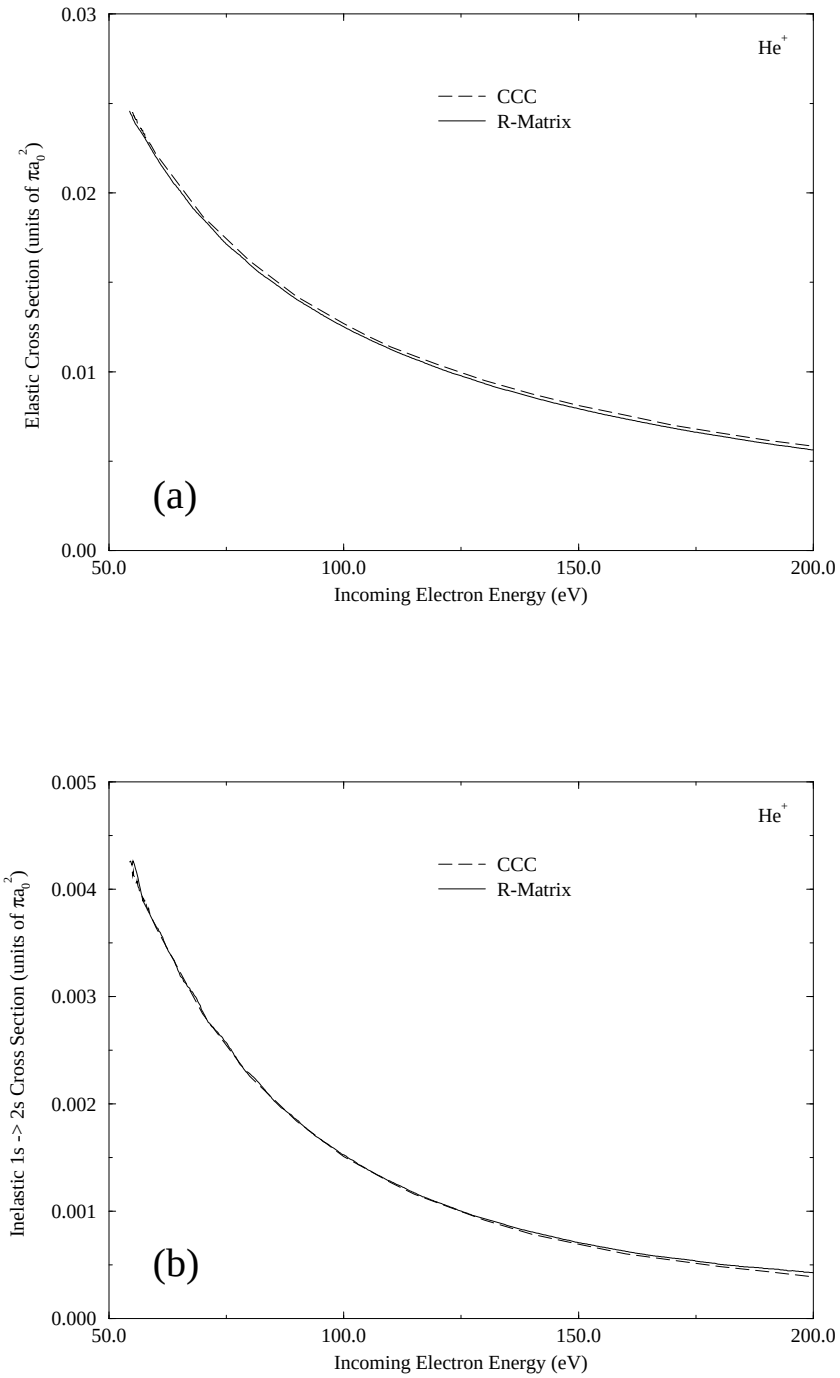

Figure 11. Singlet elastic and inelastic $1s - 2s$ cross sections for the Temkin-Poet model of electron-He^+ scattering. The dashed line represents calculations performed with the CCC approach, while the solid line represents calculations performed with the R-matrix technique. These figures are taken from Ref. [29].

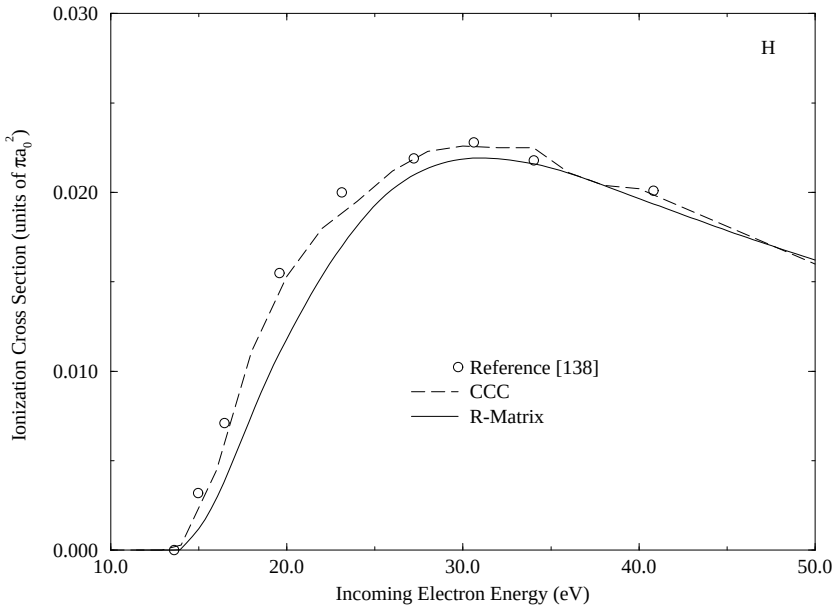

Figure 12. Singlet ionization cross sections for the Temkin-Poet model of electron-hydrogen scattering. The interpolated values, as calculated by Callaway and Oza [138] are denoted by open circles. The dashed line represents calculations performed with the CCC approach, while the solid line represents calculations performed with the R-matrix technique. This figure is taken from Ref. [29].

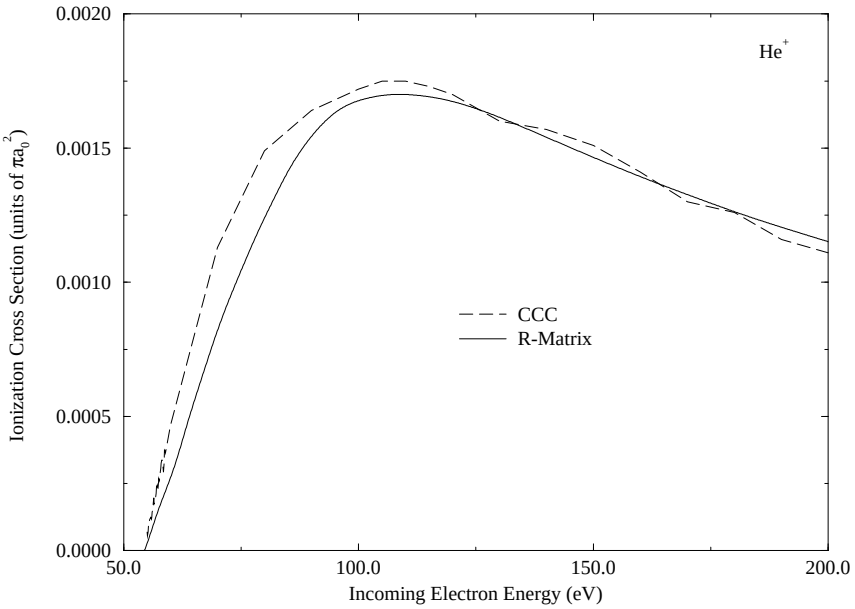

Figure 13. Singlet ionization cross sections for the Temkin-Poet model of electron-He^+ scattering. The dashed line represents calculations performed with the CCC approach, while the solid line represents calculations performed with the R-matrix technique. This figure is taken from Ref. [29].

also not expected to predict accurate ionization cross sections at a few eV above threshold. Application of this method to the real case of e-H scattering from threshold to 500 eV gave results which were up to 30% lower than the experimental values in the threshold region up to 4 eV [27]. More accurate studies of the ionization cross sections for low energies have been discussed in sections 2.3 and 2.4.

Fig. 13 also shows fairly good agreement between the results calculated for e-He^+ ionization in the TP model with the CCC and the R-matrix method over most of the energy range. As with the case for e-H scattering, the R-matrix method significantly underestimates the cross section in the energy range just above threshold. Presumably, better agreement could be achieved at lower energies if a larger reaction volume size was used for the R-matrix method, as the electron-electron correlation effects would then be included over a much greater distance. Exploratory attempts to significantly increase the reaction volume size indicated that this appears to be the case, although the use of a much larger basis set size led to numerical instabilities which did not permit a smooth cross section to be obtained over a very large energy range.

Although the TP model greatly simplifies the calculations required to obtain electron scattering cross sections, the R-matrix approach described here can be applied to more complicated processes, such as the real case of e-H scattering. One reason for adopting the TP model was to reduce the required amount of calculation. In this study, we required roughly a couple of hours on a DEC 5000/240 workstation to obtain cross sections for a single box size. To apply this R-matrix technique to real electron scattering processes, the total number of two-electron orbitals needs to be increased by roughly a factor of five or ten for each total orbital angular momentum of the system. Although the number of calculations required greatly increases due to a larger number of required orbital configurations, the R-matrix technique should be capable of generating accurate cross sections for this case. Furthermore, a significant reduction in required calculations can be accomplished if reliable

results are generated with a frame transformation/convolution approach for a single box size rather than a box averaging technique.

By exploring a simplified model of electron scattering, many of the advantages and limitations of both the CCC approach and the eigenchannel R-matrix technique have become apparent. One of the major problems encountered in extending the eigenchannel R-matrix technique to double continuum processes involves our inability to obtain well-behaved antisymmetric solutions outside the reaction volume in the double continuum region (region IV of Fig. 1). This asymmetry can be seen most clearly in plots of the calculated partial ionization cross section versus the "inner" electron energy ϵ. If antisymmetry was strictly enforced, the partial cross section must be symmetric about the midpoint of the channel energy, since there would be no way of distinguishing between the channel energy ϵ_i of one electron, and the energy $E - \epsilon_i$ of the other electron, where E is the total energy of the system. However, this symmetry is not exhibited by our R-matrix or CCC results.

Neither method is able to provide accurate cross sections at low energies. However, the CCC approach is able to predict better results near threshold. This reflects the limitation of our R-matrix approach to adequately treat electron-electron correlation effects outside the reaction volume. Approximations in our current approach also appear to limit accurate calculations to total cross sections, whereas the CCC method has been used successfully to generate accurate differential cross sections. The limitations associated with basis set size are more apparent for our R-matrix method, as the results shown here are for a smaller energy range than has been previously reported in the CCC calculations.

A simplified model of electron scattering was adopted here in order to compare ionization cross sections obtained with an eigenchannel R-matrix method and the CCC approach. The singlet cross sections for e-H scattering have been explored for an energy range from threshold up to 50 eV, while e-He^+ singlet scattering cross sections have been calculated for an energy range from threshold up to 200 eV. The results obtained by the two different

methods agree well over most of the energy range considered here. However, our R-matrix calculations are found to underestimate the cross section for energies just above threshold. This discrepancy at low energies indicates that our approximation to neglect the electron-electron correlations outside our reaction volume is not adequate for describing the two electron escape process for this energy range. Although the error associated with describing electron impact ionization processes appears to be smaller than the error encountered in describing helium double photoionization, the magnitude of the error associated with our present approach may be too large to resolve the discrepancy between the experimental and theoretical values of helium photoionization shown in Fig. 5. Nevertheless, the agreement with the CCC approach gives us confidence that the eigenchannel R-matrix technique can describe two-electron escape processes in the intermediate energy region, where the maximum ionization cross section occurs, with an error of about 10-15%.

CHAPTER 4

FINITE ELEMENTS: A NEW APPROACH

As has been shown in the previous chapter, an extension of the eigenchannel R-matrix method achieved some success in treating double escape processes. Although this approach seems capable of describing two electron escape processes accurately, some problems arose in its application to helium double photoionization. A discrepancy between the various forms used in calculating dipole matrix elements indicated inaccuracies in the initial and/or final state wave functions. In particular, the discrepancy between the velocity and acceleration forms was roughly 20% (see Fig. 4), and the length form gave results which were nearly an order of magnitude larger than the results obtained for other forms. Interestingly, the convergent close-coupling method of Kheifets and Bray [58] gave unreasonable results in the length form, much like our R-matrix calculations. However, the hyperspherical close-coupling method of Tang and Shimamura [62] was able to obtain good agreement between length and acceleration forms. In an effort to reduce the discrepancy between the various dipole forms, we have combined an eigenchannel R-matrix approach with a finite element method to treat two electron photoejection.

4.1 Method of Finite Elements

The eigenchannel R-matrix method (Chapter 2) and its application to helium double photoionization and electron impact ionization (Chapter 3) have been previously discussed. The major difference between the current approach and our previous application involves our choice for the variational basis set. Instead of forming a two electron *global* basis set consisting of products of one electron hydrogenic orbitals, we adopt a *local* finite element basis set for the present study. Our expectation was that the finite element method

(or other local basis set methods, *e.g.*, B-splines) should be able to better represent the initial and final state wave functions, thereby reducing the discrepancy among the different dipole forms. The suitability of a finite element approach for calculating accurate bound state wave functions has been previously shown [150, 151]. This method has been used to calculate accurate bound state excitation cross sections in elastic scattering [152]. A similar B-spline local basis set has been combined recently with R-matrix theory to address electron scattering of hydrogen [153]. In this work, we report the first application of a finite element basis set to *two electron escape processes*. The finite element set used in our approach consists of a set of six fifth order Hermite interpolating polynomials that are shown in Fig. 14 and described elsewhere [152, 154].

In our original approach, we solved for the radial part of the one-electron hydrogenic orbitals $\phi_k(r)$ subject to "box" boundary conditions, that is, boundary conditions imposed at the surface of the reaction volume. Orbitals that vanished at the outer radius of the R-matrix box were referred to as "closed" orbitals, while "open" orbitals referred to orbitals which were nonzero at the box radius. In our more recent approach, we expand these hydrogenic orbitals with a finite element basis set:

$$\phi_k(r) = \sum_{n=1}^{N} \sum_{i=1}^{6} C_i^n u_i(x_n), \tag{37}$$

where n denotes the sector number, and i denotes one of the six Hermite interpolating polynomials. These six polynomials are defined by enforcing a total of six "boundary" conditions at three points within a sector, namely, the polynomial value and its first derivative at the two endpoints and the center of the sector. Each of the six polynomials will have only one nonzero boundary condition, with this boundary condition chosen to be unity (see Fig. 14). Also, $u_i(x_n)$ is defined to be nonzero only in sector n, and x_n is only defined over the interval [-1,1]. The transformation to the "physical sector" $[r_i, r_{i+1}]$ for a value r $(r_i < r < r_{i+1})$ is then given by

$$r = a_i x_i + b_i, \tag{38}$$

where

$$a_i = \frac{r_{i+1} - r_i}{2}, b_i = \frac{r_{i+1} + r_i}{2}. \tag{39}$$

Although there appears to be $6N$ independent coefficients in Eq. 37, by enforcing boundary conditions at the origin and the box radius r_0, and also by imposing the constraint of a continuous wave function and first derivative across each sector boundary, the number of independent coefficients is reduced to $4N$.

As in our earlier R-matrix calculations, a two-electron wave function is formed by taking products of one electron orbitals:

$$\psi(\vec{r}_1, \vec{r}_2) = \mathcal{A} \sum_{n=1}^{N} \sum_{m=1}^{M} \sum_{i=1}^{6} \sum_{j=1}^{6} C_{ij}^{nm} u_i(x_n) u_j(y_m) \mathcal{Y}_{l_1 l_2}^{LM}(\hat{r}_1, \hat{r}_2), \tag{40}$$

where $\mathcal{A}$ is the antisymmetrization operator (see Appendix B for further details), and $\mathcal{Y}_{l_1 l_2}^{LM}(\hat{r}_1, \hat{r}_2)$ is a coupled spherical harmonic. Our two dimensional sectors are chosen to be rectangular, so that $u_i(x_n)$ and $u_j(y_m)$ are of similar form. Although there are 36 coefficients for each sector, enforcing continuity of the wave function and first derivatives across sector boundaries reduces the number of independent coefficients to 16. To obtain the ground state wave function, we impose the boundary condition that the wave function vanishes on the surface of the reaction volume. This is easy to implement with a Hermite interpolating polynomial basis set, as only one of the six polynomials ($u_5(x)$, as denoted in Fig. 14) is nonzero on the outer boundary. Simply setting the corresponding coefficient of this basis function in the outermost sector to zero ensures that the wave function vanishes at the box radius.

In order to express the final state correctly, our expansion must include basis functions which are nonvanishing on the surface of the reaction volume in order to allow for electron escape. We retain the idea in our original approach of also including closed-open two electron configurations consisting of a product of a closed and an open one-electron hydrogenic orbital. However, the open hydrogenic orbital is now replaced by a single Hermite

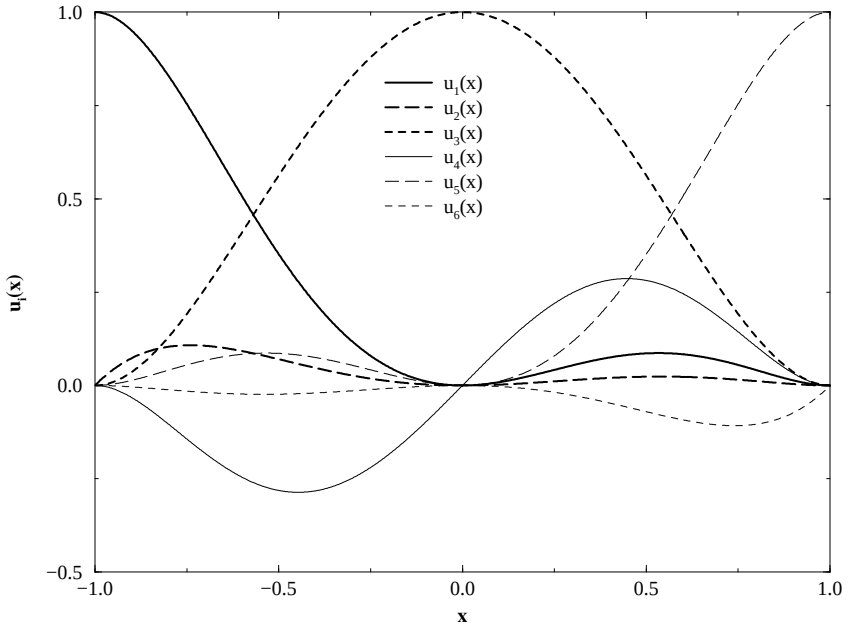

Figure 14. The set of six Hermite interpolating polynomials adopted as the finite element basis set in this study.

interpolating polynomial in the outermost sector which is nonzero at the outer boundary (denoted by $u_5(x)$). In other words, we add basis functions of the form

$$\mathcal{A}\sum_{m=1}^{M}\sum_{j=1}^{6} C_{5j}^{Nm} u_5(x_N) u_j(y_m) \mathcal{Y}_{l_1 l_2}^{LM}(\hat{r}_1, \hat{r}_2) \tag{41}$$

to our expansion in Eq. 40. Retaining the closed-open type of two-electron configurations allows us to use the same criterion as previously to distinguish between single and double photoionization. That is, if the energy of our closed orbital representing the "inner" electron is negative, then we consider it to remain bound (single ionization), whereas a positive closed orbital energy is considered ionized (double ionization). This criterion along with a box averaging technique was used to obtain single and double photoionization cross sections in our original study. An improvement over this approach (the frame transformation, section 3.2.4) has been developed since then. In the context of photoabsorption, each closed orbital will contribute to both the single and double ejection cross section. The contribution of each closed orbital to photoejection of the "inner" electron can be determined by projecting the wave function onto a continuum hydrogenic wave function. That is, analogous to Eq. 34 in the case of electron scattering, for double photoejection processes the "box" dipole matrix $D^{(-)box}$ is related to the physical dipole matrix $D^{(-)phys}$ by

$$D_{\epsilon l,g}^{(-)phys} = \sum_{\overline{n}\overline{l}} \langle \epsilon l | \overline{n}\overline{l} \rangle D_{\overline{n}\overline{l},g}^{(-)box}, \tag{42}$$

where $D_{\overline{n}\overline{l},g}^{(-)box}$ represents the dipole matrix element for excitation of the inner electron from the ground state "g" to the final pseudostate $\overline{n}\overline{l}$, and ϵl denotes the final continuum state hydrogenic wavefunction. Similarly, single photoejection cross sections (with the "inner" electron remaining bound) are obtained by projecting the wave function onto a physical bound state hydrogenic wave function. The double photoejection cross section is given (in a.u.) by

$$\sigma = \frac{4\pi^2\alpha}{\omega} \sum_{l} \int_0^E d\epsilon \left| \sum_{\overline{n}\overline{l}} \langle \epsilon l | \overline{n}\overline{l} \rangle D_{\overline{n}\overline{l},g}^{(-)box} \right|^2, \tag{43}$$

where $D^{(-)box}_{\overline{n}\overline{l},g}$ represents the velocity form of the dipole matrix element for excitation of the inner electron from the ground state "g" to the final pseudostate $\overline{n}\overline{l}$, α is the fine-structure constant, and ω is the photon energy in a.u. (compare to Eq. 12). This frame transformation technique is used to obtain the results shown here.

Upon first glance, it would appear that the finite element basis set has a disadvantage of requiring the solution of a larger number of expansion coefficients than would be required for the hydrogenic basis set used previously, ultimately limiting the number of finite element sectors that could be used. However, since the local basis functions are only defined to be nonzero for a given sector, the Hamiltonian and overlap matrices are sparse. Efficient numerical routines are implemented to take advantage of these sparse, symmetric matrices. A Lanczos algorithm [155] is used to obtain the helium ground state wave function and energy. This iterative numerical method allows one to obtain the lowest eigenvalues for a specified small number of eigenvectors without having to diagonalize the entire matrix. The final state is obtained by solving the usual generalized eigenvalue problem [23]

$$\underline{\Gamma} C = b \underline{\Lambda} C, \tag{44}$$

where

$$\underline{\Gamma} = 2[E\underline{S} - \underline{H} - \underline{L}], \tag{45}$$

$\underline{S}$ is the overlap matrix, $\underline{H}$ is the Hamiltonian matrix, $\underline{L}$ is the Bloch operator, and $\underline{\Lambda}$ is the surface overlap matrix. The matrices in Eq. 44 are partitioned into closed and open basis sets:

$$\begin{bmatrix} \underline{\Gamma}^{cc} & \underline{\Gamma}^{co} \\ \underline{\Gamma}^{oc} & \underline{\Gamma}^{oo} \end{bmatrix} \begin{bmatrix} C^c \\ C^o \end{bmatrix} = b \begin{bmatrix} 0 & 0 \\ 0 & \underline{\Lambda}^{oo} \end{bmatrix} \begin{bmatrix} C^c \\ C^o \end{bmatrix}. \tag{46}$$

This leads to the reduced generalized eigenvalue problem:

$$\underline{\Omega}^{oo} C^o = b \underline{\Lambda}^{oo} C^o, \tag{47}$$

where

$$\underline{\Omega}^{oo} = \underline{\Gamma}^{oo} - \underline{\Gamma}^{oc}(\underline{\Gamma}^{cc})^{-1}\underline{\Gamma}^{co}. \tag{48}$$

Once the open components C^o of the solution eigenvector are obtained by solving Eq. 47, the closed components are given by

$$C^c = -(\underline{\Gamma}^{cc})^{-1}\underline{\Gamma}^{co}C^o. \tag{49}$$

The streamlined eigenchannel treatment [23] involves a transformation which diagonalizes the Hamiltonian matrix. For a closed two-electron basis set which is orthogonal, the closed portion of the overlap matrix is diagonal. Consequently, $\underline{\Gamma}^{cc}$ becomes diagonal after the Hamiltonian is transformed, and so is trivial to invert. As this transformation of the Hamiltonian matrix only needs to be performed once, a great computational improvement is attained over directly solving for the generalized eigenvalue problem at each desired energy.

For our purposes, application of this streamlined transformation is impractical owing to the large dimension of the Hamiltonian and overlap matrices. Rather than solve the original generalized eigenvalue problem (Eq. 44), we would like to solve the reduced eigenvalue problem, given by Eq. 47. Note that $\underline{\Omega}^{oo}$ involves the inverse of $\underline{\Gamma}^{cc}$, which has large dimension, but is sparse. Rather than directly calculating the inverse of this matrix, we use a linear algebraic routine to solve the sparse system of equations

$$\underline{\Gamma}^{cc}\underline{Q}^{co} = \underline{\Gamma}^{co}. \tag{50}$$

The $\underline{\Omega}^{oo}$ matrix is then given by

$$\underline{\Omega}^{oo} = \underline{\Gamma}^{oo} - \underline{\Gamma}^{oc}\underline{Q}^{co}. \tag{51}$$

For our finite element application, the open-open part of the surface overlap matrix is diagonal, and in fact equal to the identity matrix. This reduces the generalized eigenvalue problem given in Eq. 47 to the ordinary eigenvalue problem

$$\underline{\Omega}^{oo}C^o = bC^o. \tag{52}$$

The greatest computational effort required to obtain results with a finite element basis involves solving the system of equations in Eq. 50. Originally, a conjugate gradient method with a diagonal preconditioner was used to solve this system of equations. A generalized minimum residual method iterative method with an incomplete LU factorization (factorization of a matrix into the product of a lower triangular and an upper triangular matrix; see Ref [156] for further details) for preconditioning was later adopted from the sparse linear algebra package (SLAP) to perform this task more efficiently. However, the amount of computational effort required to solve this linear set of equations using these iterative methods increases rapidly with energy. This is due in part to a larger number of channels which are required to be included, and in part due to the need for a greater density of sectors (smaller sector sizes) in order to accurately represent the small wavelength behavior of the wavefunction in some of the channels. Numerically, this translates into a larger number of iterations required to solve for each successive right hand side vector, and also a larger number of right hand side vectors which require a solution. The number of right hand side vectors is simply the total number of energetically allowed channels. Due to the large computational time which was required to calculate cross sections at high energies, practical application of this approach to helium was limited to energies no higher than 100 eV above the double photoionization threshold.

A tremendous increase in the numerical efficiency of our method for solving linear systems of equations was achieved by adopting a complete factorization approach. Not only is the $\underline{\Gamma}^{cc}$ matrix in Eq. 50 a large sparse matrix, but for the appropriate numbering scheme of finite element nodes it also has a banded structure. LAPACK (Linear Algebra Package; see Ref. [157]) routines for banded matrices are used to perform an LU factorization of this matrix. This leads to a numerical method whose time requirements are only weakly dependent on the number of channels included (and thus more nearly energy-independent).

The time requirements for this approach now depend primarily on the number of finite element basis functions included. Applications of this method to helium double photoionization have decreased the computational time required to obtain results by a factor of 30-50 over previous iterative solvers. One drawback of the LAPACK banded factorization routine is the greater memory requirements. Whereas previous routines could use sparse matrix storage routines which only stored nonzero elements (and their indices), all elements within the maximum bandwidth of the banded matrix must be stored in a full matrix in order to use the LAPACK routine. Application of this numerical routine to two-electron escape processes using 18x18 finite element sectors has required memory usage of 750MB. Since this memory requirement exceeds the current capabilities of our "in-house" computer resources, the use of a SGI (Silicon Graphics Incorporated) Power Challenge machine at the National Center for Supercomputer Applications was necessary for performing the calculations presented in the next section.

4.2 Double Photoejection Cross Sections of He and H^-

Although helium double photoionization processes have received a tremendous amount of attention in the past, there has been a surprisingly great amount of disagreement concerning the maximum value of the ratio of double to single ionization, both from experiment and theory, at least in the region of intermediate photon energies. The maximum value of this ratio occurs for photon energies in the range of 150-250 eV. It has been predicted and measured to reach peak values anywhere from 0.030 to 0.055 before slowly falling to an asymptotic value of 0.0167 at high energies [38, 102, 113, 158]. The discrepancies among different approaches to obtain the values for this parameter illustrate the difficulties that have been encountered by theoretical attempts to describe the relatively infrequent occurrence of two electron escape processes in this intermediate energy range.

In contrast to the case for helium, studies of one- and two-electron photoejection from H^- at photon energies above the double escape threshold have been quite sparse. The

determination of H^- photodetachment cross sections has received a significant amount of focus for low photon energies [159], primarily due to its importance in astrophysics. The threshold law for double photodetachment of H^- has been explored both theoretically [160] and experimentally [95], but the applicability of these studies are limited to just the first one or two eV above threshold. Although no experimental values of H^- photoejection at higher energies are known to exist, it should be possible to perform these types of experiments in the near future. To our knowledge, only one theoretical study has been undertaken to address photoejection of H^- at these energies. This sole theoretical study was performed by Broad and Reinhardt over twenty years ago using a multichannel J-matrix technique with an L^2 basis set [52]. Total photodetachment cross sections were reported for photon energies in the range of 1-69 eV. They claimed a convergence of their two electron photoejection cross sections to within 15% and quoted a value for this ratio of roughly 0.04 over this energy range. Results presented in their paper indicated a maximum value for the ratio σ_{2e}/σ_{1e} which lies in the range of 0.055-0.085. Fluctuations in their calculated double photoejection cross sections made it difficult to determine a precise value for the peak ratio. However, we can ascertain an approximate "error bar" of ± 0.020 for these calculations of Broad and Reinhardt.

Like helium, H^- is an ideal system for exploring two electron photoejection, due to its inherent simplicity. There are important differences, however, between double photoionization of helium and double photodetachment of H^-. First, the ratio between the single and double escape threshold energies is much smaller for H^- than for He, since H^- has only a single bound state. Secondly, while a single electron escaping from helium experiences a screened Coulomb potential (to first approximation), this Coulomb potential is absent for a single electron escaping from H^-. Due to the smaller nuclear charge of H^- in comparison to helium, one expects electron interaction effects to play an even greater role in the dynamics of photoejection for this case. Fig. 15 compares the radial ground state wavefunction of

helium and H^-. The broader H^- wavefunction reflects its smaller nuclear charge.

We calculate the ratio of double to single photoejection cross sections of helium and H^- for photon energies of 79-460 eV and 14.35-110 eV [30]. Roughly 180 hours of supercomputer time on a SGI Power Challenge machine was used to perform these cross section calculations. The results presented here were obtained by using three partial waves in the initial state and four partial waves in the final state. This is in contrast to our earlier study of helium photoionization, where two partial waves were used for the initial state and three partial waves were used for the final state. Box averaging was used to obtain the cross section profiles presented here, and a frame transformation was implemented to distinguish between single and double photoejection contributions. A Gailitis averaging technique, as outlined in Chapter 3, was used to obtain results for helium. Our calculated ground state energies of helium and H^- agree well with the "exact" nonrelativistic infinite mass values, which are taken from Reference [161] (see Table 1). Note that the ground state energy of helium in our original calculation using a hydrogenic basis is much less accurate than the value obtained with a finite element basis. Part of this is improvement is due to the inclusion of an additional partial wave in our finite element calculations (see Table 2), but some improvement is also due to our use of a local basis set.

Our results for the ratio of double to single photoionization for helium are compared to recent theoretical and experimental values in Fig. 16. Experimental measurements of this ratio by Dörner *et al.* [26] and Levin *et al.* [158] over the intermediate energy range have similar profiles, but differ in magnitude by 10-20%. Samson's values [162] in Fig. 16 have actually been fitted to a smooth curve, but these smoothed values differ very little from the original experimental values (to within roughly a couple of percent). The error bar associated with Samson's measurements is approximately 5%, while Levin's experimental error bar is comparable to the scatter in his reported values, as seen in Fig. 16. Recent theoretical calculations of the ratio include our previous eigenchannel R-matrix calculations using a

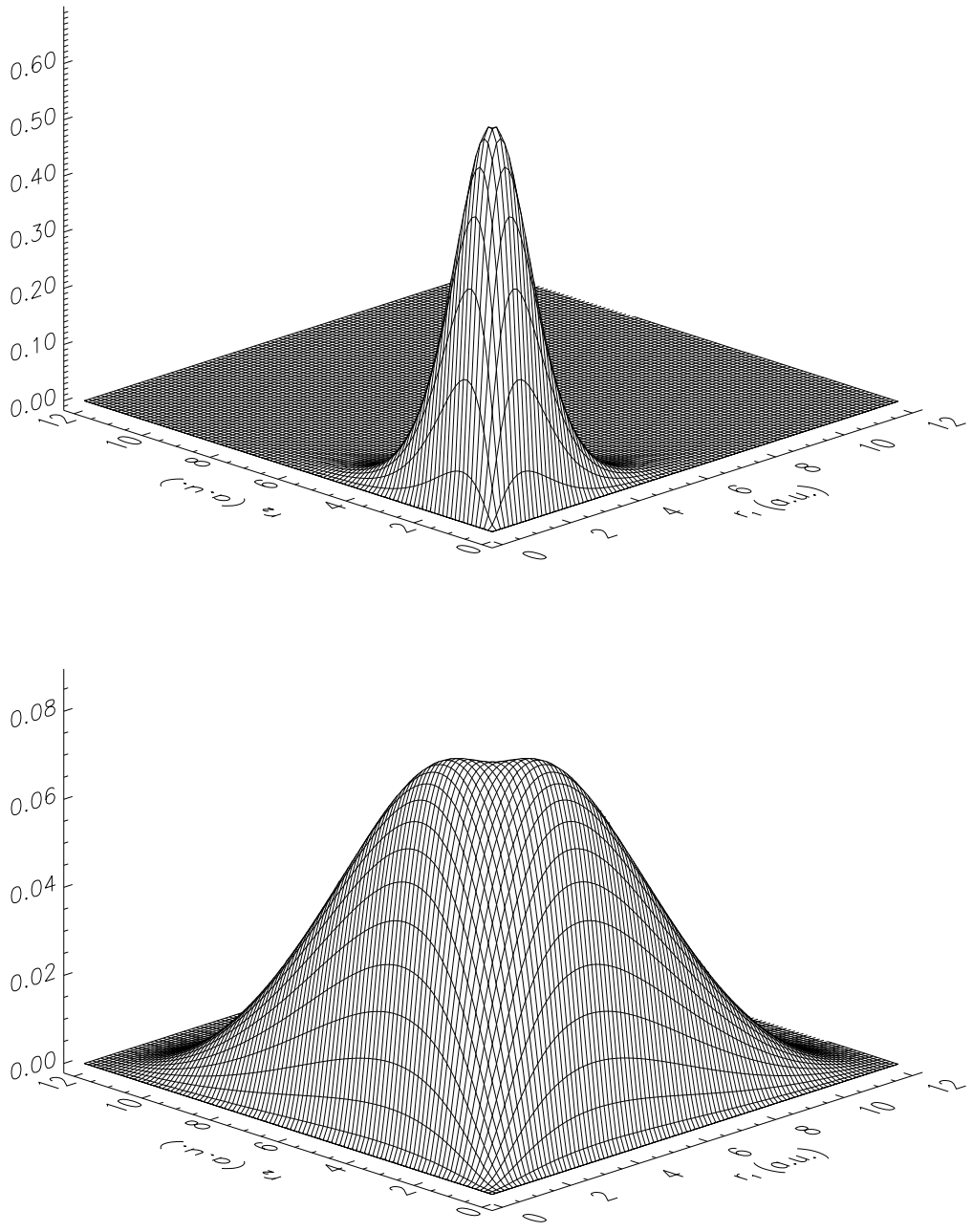

Figure 15. Comparison of the He (top) and H^- (bottom) ground state radial wavefunctions. These are plots of the square of the scaled radial wavefunction ($|r_1 r_2 \Psi(r_1, r_2)|^2$) for the partial wave $l_1 = l_2 = 0$. The He wavefunction extends to approximately 4 a.u., while the H^- wavefunction extends to about 10 a.u. This reflects the weaker binding energy of the two electrons to the nucleus for H^-.

Table 1. Comparison of ground state energies of helium and H^-, calculated with hydrogenic and finite element basis sets. The corresponding ground state wavefunctions were used to obtain the helium and H^- double photoejection results in Chapters 3 and 4. The "exact" nonrelativistic infinite mass values listed in the table were taken from Ref. [161]. Note that the ground state energy of helium in our original calculation using a hydrogenic basis is much less accurate than the value obtained with a finite element basis. Part of this improvement is due to the inclusion of an additional partial wave in our finite element calculations (see Table 2), but some improvement is also due to the use of a local basis set.

	He (a.u.)	H^- (a.u.)
"Exact"	-2.9037	-0.52775
Finite Elements	-2.9028	-0.52744
Hydrogenic Basis	-2.8967	————

Table 2. Dependence of helium and H^- ground state energies on the number of angular configurations included. Finite element values for He were obtained using a reaction volume of 10 a.u., while a reaction volume of 26 a.u. was used for the H^- values. The helium calculations were performed with 12 sectors in each radial coordinate (a linear mesh of 4 sectors from 0-2 a.u. and of 8 sectors from 2-10 a.u.), while 16 sectors (a linear mesh of 4 sectors from 0-2 a.u. and of 12 sectors from 2-26 a.u.) in each radial coordinate were used to obtain the values for H^-.

Num. of Ang. Configs.	He (a.u.)	H^- (a.u.)
1	-2.8790	-0.51448
2	-2.9005	-0.52658
3	-2.9028	-0.52744
4	-2.9033	-0.52762

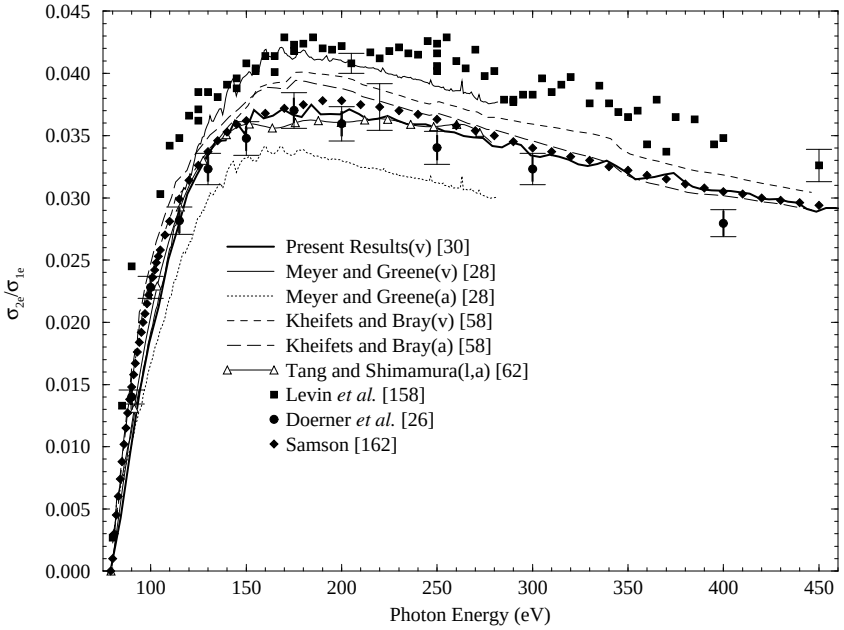

Figure 16. Comparison of the ratio of double to single photoionization for helium with other theoretical and experimental values. Our results in a previous study are shown by the narrow solid and dotted lines. This figure is taken from Ref. [30].

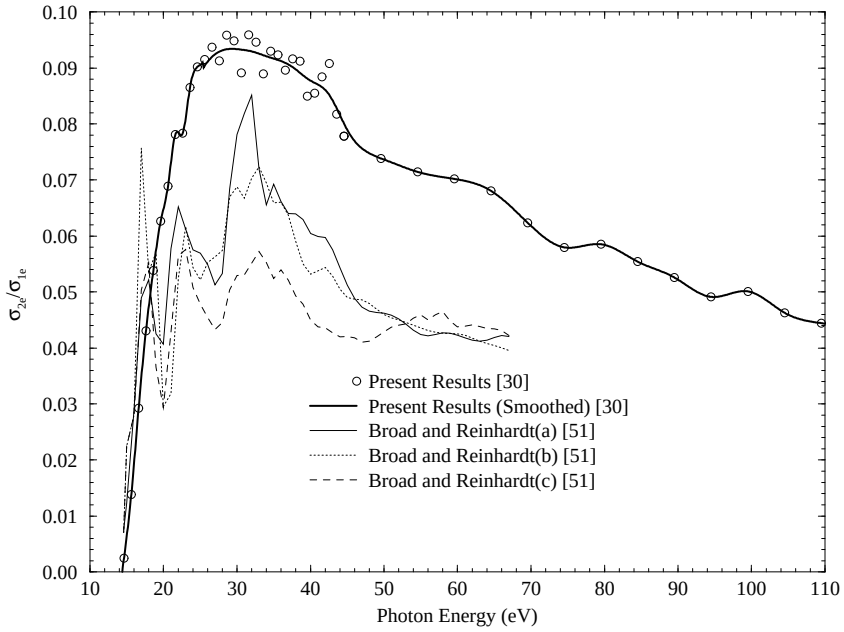

Figure 17. Comparison of the ratio of double to single photodetachment for H^- with previous calculations of Broad and Reinhardt [52]. The results of Broad and Reinhardt were obtained using the final state basis sets: a) $10s, 10p, 6d$, b) $7s, 10p, 6d$, and c) $7s, 10p, 6d, 4f$. This figure is taken from Ref. [30].

hydrogenic basis set [28], the convergent close-coupling calculations of Kheifets and Bray [58], and the hyperspherical close-coupling calculations of Tang and Shimamura [62]. Our finite element results were obtained by box averaging over five box sizes in the range 12-16 a.u. for photon energies of 80-280 eV, while a single box size of 10 a.u. was used to obtain the results for 280-460 eV. A smaller reaction volume can be used at higher energies, as electron-electron interaction effects are more tightly confined near the nucleus. Our calculated values of the ratio are lower than most of the other theoretical and experimental values for the first few eV above threshold. This is not unexpected, as the near threshold region is where our approximation of unequal energy sharing is anticipated to fail. For higher photon energies, our calculated results agree well with the experimental values of Samson and coworkers. Our results are also consistent with the experimental values of Dörner, with the exception of his highest energy measurement.

Fig. 16 shows only our velocity form calculations. Calculations performed using the acceleration form of the dipole operator are nearly identical (agreement to better than 1%) to those of the velocity form over the entire energy range shown here. This is in contrast to our previous results of helium photoionization (shown by the narrow solid and dotted lines in Fig. 16) using a hydrogenic basis set in which the discrepancy between the velocity and acceleration forms was 20-25%. Furthermore, the length form calculations of double ionization cross sections in this previous study were an order of magnitude larger than the calculations in the other forms. For our finite element approach, calculations in the length form agree closely with the other forms up to about 100 eV above the double escape threshold before slowly diverging. At the highest energies shown in Fig. 16, double ionization cross sections calculated with the length form are about 10-15% higher than the values calculated with the other forms. Although the use of a finite element basis set requires a much greater computational effort in comparison to a hydrogenic basis set, this choice of basis set can be systematically improved with less effort. The resulting improved agreement among the

various dipole forms is dramatic, illustrating the usefulness of finite element techniques for addressing such problems.

Our results for the double to single photoejection ratio in H^- are shown in Fig. 17. We averaged our calculation over five box radii in the range 24-32 a.u. for photon energies of 14.35-65 eV, and over two box radii of 24 and 26 a.u. for photon energies of 65-95 eV. The results for 95-110 eV were obtained with a single box radius of 24 a.u. A box of roughly twice the size used in our helium calculations is necessary to accurately describe H^- photodetachment, since hydrogen wavefunctions extend roughly twice as far as those of He^+. We obtain a smooth profile of our ratio by convolving our box averaged values (open circles) with a Gaussian function. The three curves of Broad and Reinhardt [52] in Fig. 17 were obtained with different final state basis sets. Our values for the H^- total photoabsorption cross section agree well with those of Broad and Reinhardt. However, our maximum value of the branching ratio for double photodetachment is significantly larger than their values. The peak value of our ratio of 0.094 ± 0.006 lies in the photon energy range of 25-35 eV. We believe that our new calculations are more accurate than the results of Broad and Reinhardt. Evidence of this is suggested by the smaller amount of scatter among our results in Fig. 17. However, our results are not seriously in disagreement with their calculations, since their calculated values have correspondingly large "theoretical error bars". For this reason, the two calculations appear to be consistent, and the pioneering work of Ref. [52] is impressive in view of the limited computational resources available at that time.

It is interesting to note the differences in two electron escape for helium and H^-. To a first approximation, one might expect the maximum in the ratio of double to single photoejection to scale as a simple function of the nuclear charge [122]. However, H^- is quite different from other heliumlike atoms, and so would not be expected to obey any simple scaling law. Our calculations indicate that the maximum value of the ratio for H^- of 0.094 ± 0.006 is about three times as large as the value for helium of 0.037 ± 0.001. Also, the

peak of the ratio occurs at an energy approximately six times smaller for H^- than for helium, relative to the double escape threshold. This is a reflection of the small electron affinity of H^-, as a smaller required energy for removing one electron in H^- leaves more energy available to remove the remaining electron. The maximum value of the double photoejection cross section for H^- is observed to be about twenty times larger than that for helium, a reflection of helium's deeper Coulombic well.

Another issue of interest is the predicted high energy limit of the branching ratio between double and single photoejection. The value of this limit is predicted to be 0.0150 for H^- and 0.0167 for He [38, 102]. However, our calculations show a much larger value of the *peak* ratio for H^- than for helium. The high energy values for the ratio in H^- and helium does not seem consistent with the idea that electron-electron correlations play a stronger role for smaller nuclear charge. One possible explanation for this apparent inconsistency is the fact that the n=2 partial cross section for H^- is comparable to the n=1 cross section [52], contributing more to the single detachment cross section, and therefore less to the double detachment cross section [163].

One open question concerning double photoejection calculations is the number of angular configurations required to accurately describe the $L = 0$ initial and $L = 1$ final state wavefunctions, such that cross section values are converged. The dependence of ground state energy on the number of angular configurations is shown in Table 1. In our initial calculations, we only included two angular configurations (ss, pp) to describe the initial state, whereas our latest calculations used three angular configurations (ss, pp, dd). From Table 1, we see that a significant improvement in the ground state energy is achieved by increasing the number of angular configurations from two to three, while the improvement in energy is comparatively less when the number of angular configurations is increased from three to four. This trend is similar for helium and H^-.

In contrast to the results found for the initial state, the contribution to the double

photoejection cross section for each final state angular configuration is quite different for the separate cases of helium and H^-. As seen in Fig. 18, the *sp* angular configuration gives the majority of the contribution to the helium double photoejection cross section over the photon energy range shown here, whereas the *df* configuration only gives about 10-15% of the contribution to the cross section. In contrast, the *pd* configuration dominates the double photoejection cross section of H^- in the energy range where the peak in the cross section occurs (see Fig. 19). At higher photon energies, the *df* configuration contributes the largest amount, whereas this configuration contributes the smallest amount for the case of helium. Based on the results shown in Figs. 18 and 19, we have more confidence that our cross section values for helium are converged with respect to the number of angular configurations than for the case of H^-. These figures further illustrate the difference in the double photoejection dynamics for a target in which both electrons are "almost equally" bound (helium) and a target in which there is one strongly bound and one weakly bound electron (H^-).

Preliminary calculations of photoejection processes have been performed for other ions in the helium isoelectronic sequence (Li^+, Be^{++}, C^{4+}, and O^{6+}) in an effort to evaluate the validity of scaling laws given in Ref. [122]. Although the adoption by Ref. [122] of a simple analytical approximation to the final state wavefunction is probably not adequate to determine accurate quantitative results, the derivation of approximate scaling laws is useful for understanding qualitative aspects of two electron escape. Ref. [122] uses two different analytical wavefunctions: one is a product of three two-body continuum wavefunctions, while the other contains products of only two single-center Coulomb wavefunctions. They determined that the threshold region (the region where the Wannier threshold law is valid) extends to energies up to approximately $E = (0.5eV)Z^2$, while the high energy region (the region where the ratio of double to single photoejection is a constant asymptotic value) begins at about $E = (1.0keV)Z^2$. By taking the limit $Z \to \infty$, the following scaling laws for

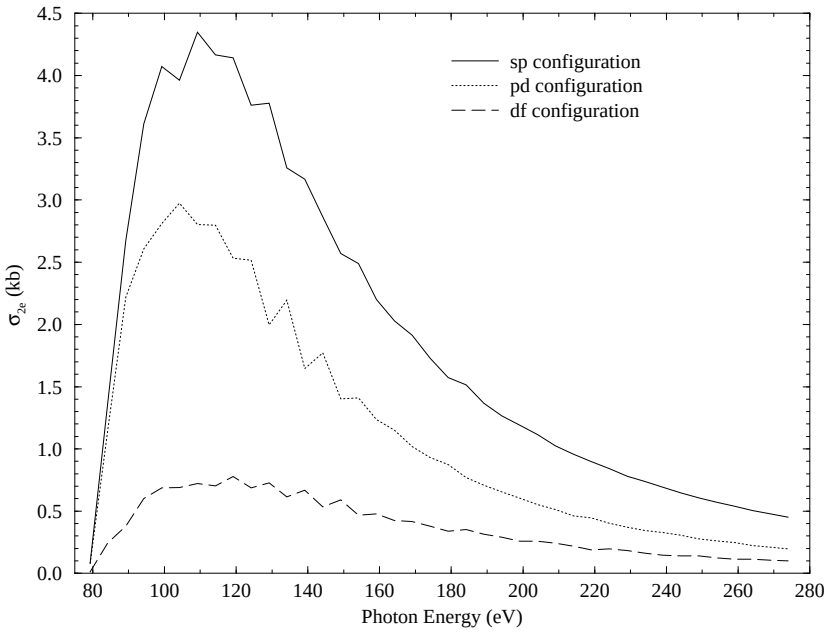

Figure 18. Contributions to the double photoejection cross section of helium for each of the three angular configurations included to describe the final state wavefunction. These values were obtained from averaging over five box sizes in the range 12-16 a.u. The configuration with the lowest individual angular momentum states dominates, whereas the configuration with highest individual angular momentum states contributes the least.

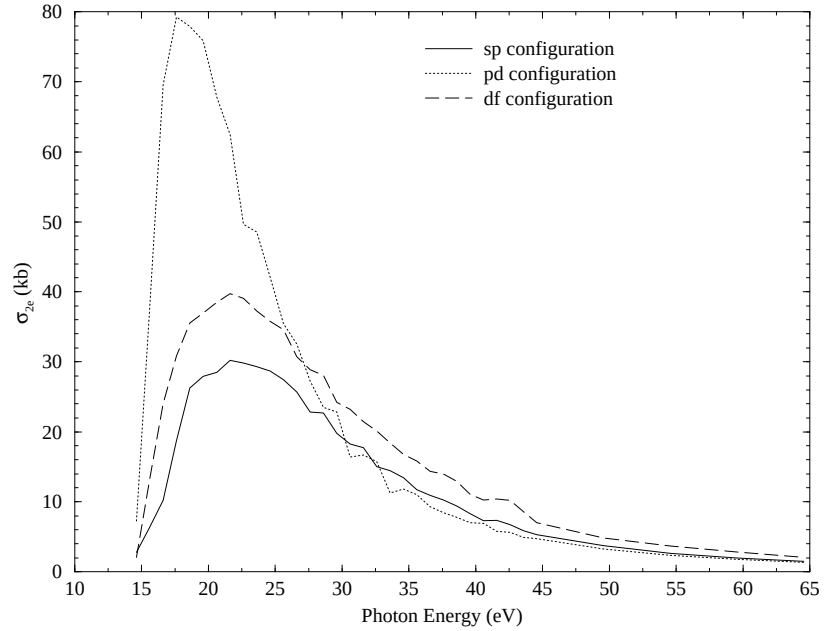

Figure 19. Contributions to the double photoejection cross section of H^- for each of the three angular configurations included to describe the final state. These values were obtained from averaging over five box sizes in the range 24-32 a.u. The *pd* configuration is observed to give the dominant contribution at low energies, whereas the *df* configuration gives the largest contribution at higher energies. This is in contrast to the case for helium (see Fig. 18).

single and double photoejection were determined:

$$\sigma_{1e}(E_f) \approx \sigma_{1e}^{Z=1}(E_f/Z^2)/Z^2, \tag{53}$$

$$\sigma_{2e}(E_f) \approx \sigma_{2e}^{Z=1}(E_f/Z^2)/Z^4, \tag{54}$$

where E_f is the final kinetic energy of the escaping electron(s).

Fig. 20 shows our calculated values of single and double photoejection cross sections for six members of the helium isoelectronic sequence. Our results were scaled according to the relations given in Eqs. 53 and 54. The box sizes used to obtain these results are given in Table 3. Since the radial extent of hydrogenic orbitals scales as $1/Z$, box sizes were also chosen to scale as $1/Z$. The results for H^- and helium have been obtained by box averaging; therefore, the profiles for these curves are smoother than for the heavier ions. Consequently, our results for the heavier ions should be interpreted as only providing approximate values, as spurious effects from pseudoresonances are still present. Evidence of this is apparent in Fig. 20(b), where a smaller relative energy mesh was chosen for C^{4+} calculations than for the other heavier ions. However, fairly accurate ground state energies and good agreement between the forms of the dipole operator give us confidence that our single box size calculations for the heavier ions are accurate to about 10-15%.

As expected, the results for H^- deviate the most from the scaling laws given in Eqs. 53 and 54. Although our single escape cross sections do not scale precisely as $1/Z^2$, the deviation from this scaling law is quite small. The $1/Z^4$ scaling law for double escape seems to be in even better agreement with our calculated values. All of the scaled double photoejection peaks have the same approximate value (within 10-20%), and the peaks occur at roughly the same energy relative to the double escape threshold when it is scaled by $1/Z^2$. A simple "rule of thumb" implied by the results in Fig. 20 is that double escape cross sections for targets with charge Z in the helium isoelectronic sequence (with the exception of H^-) will have a maximum value for photon energies (in eV) of approximately $7Z^2 + E_{D.I.}$, where $E_{D.I.}$ is the double photoionization energy threshold of the target.

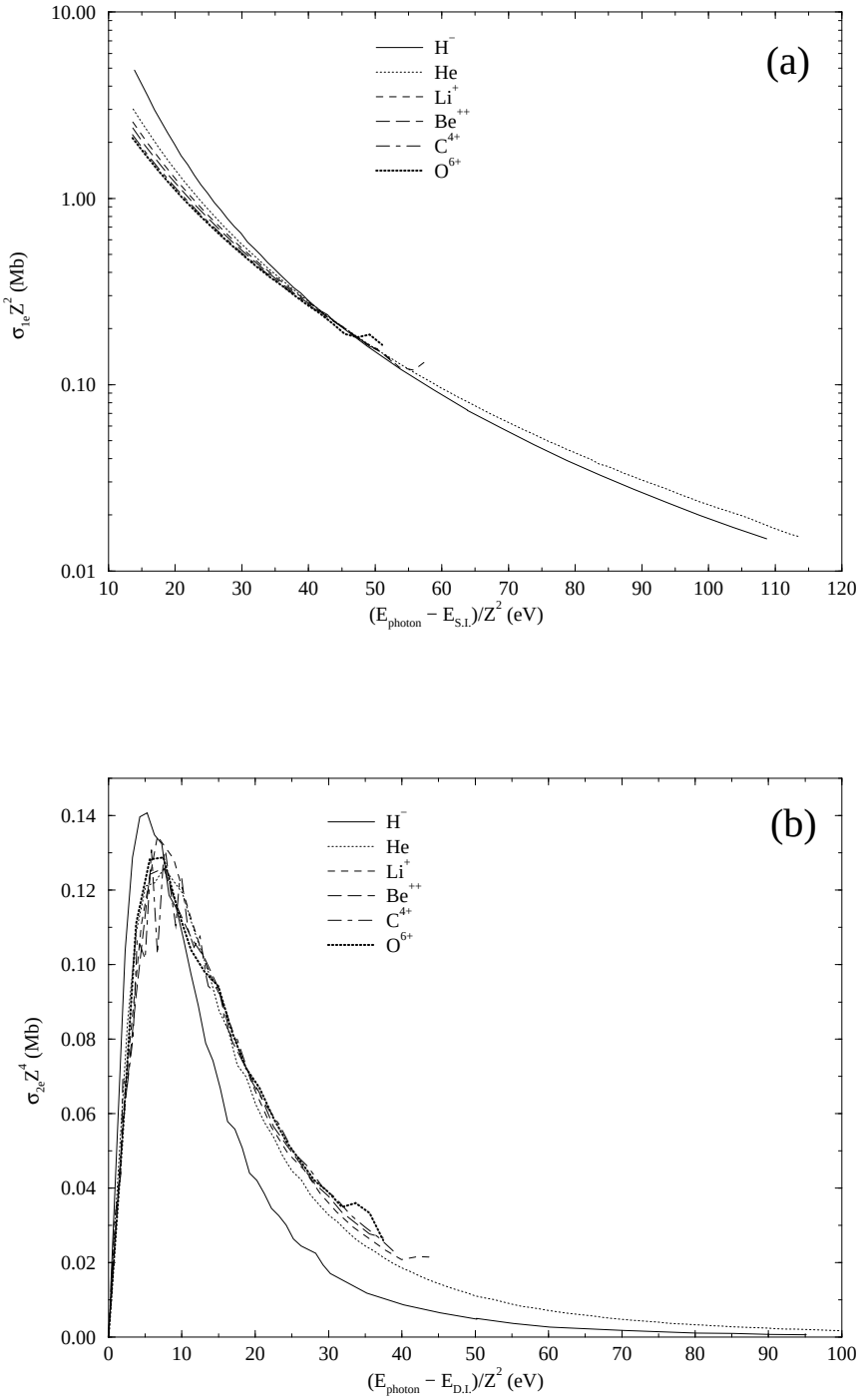

Figure 20. Scaling of six members of the helium isoelectronic sequence. Using the scaling laws reported in Ref. [122], we have plotted (a) single photoejection cross sections scaled by Z^2, and (b) double photoejection cross sections scaled by Z^4. The energy relative to the appropriate threshold is scaled by $1/Z$. The results for H^- and He were obtained by box averaging, while the results for the heavier ions were obtained with a single box size.

Since σ_{2e} scales as $1/Z^4$ and σ_{1e} scales as $1/Z^2$, the ratio R would be expected to scale as $1/Z^2$. However, an ambiguity arises in the energy scaling, as Eq. 53 involves a scaling of the energy relative to the single escape threshold, while Eq. 54 scales the energy relative to the double escape threshold. For this reason, scaled values of the ratio are not plotted here. However, the maximum values of the ratio are listed in Table 3, and do appear to scale roughly as $1/Z^2$ for $Z \geq 2$. For the photon energy ranges considered here, the profiles of R for $Z \geq 3$ did not display a clear peak, but rather long plateau features. Further investigation is required to more fully evaluate the relevance of the scaling laws proposed by Kornberg and Miraglia [122].

The results shown here illustrate the usefulness of finite element methods in describing two electron photoejection processes. In particular, the good agreement achieved between various forms of the dipole operator demonstrates the advantage of finite elements over a hydrogenic basis set. Although only total photoejection cross sections have been calculated with this method here, calculations of other observables will now be explored. In particular, calculations of partial cross sections for the production of excited hydrogenic bound states are performed in the next section. This will provide an alternate test of the importance of electron-electron interactions. The frame transformation will once again play a central role in obtaining these results.

4.3 Other Observables Associated with Two Electron Escape

To fully explore the usefulness of our method in describing two electron escape processes, we now explore other details of the escape process for which electron-electron interactions are important. Previously, our photoabsorption studies have focussed entirely on either total single or double electron escape cross sections. One key issue that tests the generality of our approach is single electron ejection from He or H^- accompanied by excitation of the residual one-electron ion $He^+(n)$ or atom $H(n)$. We will refer to these single escape processes as photoejection-induced excitation (PIE) processes.

Table 3. Six members of the He isoelectronic sequence are listed along with the box sizes used to obtain results for Fig. 20 and this table. Columns 2 and 3 are the experimental single and double ejection thresholds, taken from Ref. [164]. The values in column 4 are based on our numerical calculations. The asymptotic values for the first three members listed were taken from Refs. [38] and [102], while the last three values are based on the simple scaling law $0.0087(3/Z)^2$ in Ref. [122].

	Box Size(a.u.)	S.E.(eV)	D.E.(eV)	Max. Ratio	Asym. Ratio
H^-	24-32	0.755	14.360	0.094 ± 0.006	0.0150
He	12-16	24.587	79.007	0.037 ± 0.001	0.0167
Li^+	10	75.638	198.083	0.020 ± 0.003	0.0087
Be^{++}	7	153.893	371.573	0.011 ± 0.001	0.0049
C^{4+}	4.67	392.077	881.857	0.005 ± 0.001	0.0022
O^{6+}	3.5	739.315	1610.035	0.003 ± 0.001	0.0012

In contrast to the extensive current literature on the ratio of double to single photoejection in characterizing the strength of electron-electron interactions, the role of these interactions in PIE have been much less frequently studied. Wehlitz *et al.* [114] have recently summarized previous experimental and theoretical attempts to determine PIE cross sections in helium. They also published their experimental values for the helium partial cross section branching ratio $\sigma(n)/\sigma(1s)$ (the ratio of the cross section for photoejection plus excitation of an $n \geq 2$ state to the cross section for photoejection with the remaining electron in a $1s$ state) for a wide range of photon energies above the double escape threshold. Previous studies were primarily limited to low n excited states ($n \leq 3$) over a comparatively small energy range.

To calculate partial cross sections [31], we again adopt the frame transformation method developed in the last chapter. We accomplish this by projecting the inner electron pseudostates (calculated for a given box size r_0) onto the infinite-space bound hydrogenic target states. Analogous to Eq. 32 for electron scattering, the box dipole matrix elements $D^{(-)box}$ are related to the physical dipole matrix elements $D^{(-)phys}$ by

$$D^{(-)phys}_{nl,g} = \sum_{\overline{n}\overline{l}} \langle nl|\overline{n}\overline{l}\rangle D^{(-)box}_{\overline{n}\overline{l},g}, \tag{55}$$

where $\overline{n}\overline{l}$ represent final pseudostates corresponding to the inner electron, nl represent the final bound target eigenstates, and g refers to the ground state. This frame transformation technique has been used to obtain the results shown here.

Since the low n target states (n=1-3) fit within our R-matrix box, the energies of the eigenstates $\phi_{\overline{n}}$ of the target state Hamiltonian in the shrunken configuration space correspond closely to the energies of the physical target state for these n values (see Fig. 2). For this reason, the frame transformation technique (Eq. 55) is not necessary for calculating accurate PIE cross sections for these states. For excitation to higher lying n states, the physical target states are represented by the set of pseudostates confined to our R-matrix box. For these high n states, the electron has a high probability to be found outside our reaction volume. Since

this region is where we adopt a simplified assumption of electron-electron interactions, one might suspect that method is incapable of describing excitations to high n states. That is, a plausible expectation is that only a method which accurately represents electron-electron correlations out to large distances (large enough to contain the inner electron wavefunction) should be able to accurately describe excitation to high n states. At the same time, we have shown that our method can accurately describe helium double photoejection. Those studies employed a projection of pseudostates onto the physical continuum eigenstates which extend out to infinity. This gives some indication that our approach may be able to describe excitation to high-lying bound states that extend beyond our R-matrix box.

Our σ_n/σ_{1s} branching ratios are compared with the experimental values of Wehlitz *et al.* [114] in Fig. 21. R-matrix results for photon energies from threshold to 200 eV above threshold were obtained by averaging over five box sizes in the range 12-16 a.u., while results at higher energies were obtained with a single box size of 10 a.u. We can use a smaller reaction volume at higher energies since electron correlations are more tightly confined near the nucleus. Gailitis averaging is again used to average cross sections for the energy range below the pseudostate thresholds. Single photoejection with the remaining electron left in a $1s$ ground state accounts for approximately 90% of the total single ionization cross section in helium. Our ratios for n=2 and n=3 agree well with the experimental values across an energy range from the double escape threshold (78.98 eV) up to 500 eV, except for a small number of our calculated values which lie slightly outside the experimental error bars. Surprisingly, this good agreement also holds for $n = 4 - 6$, although these states do not fit within our R-matrix box. This result implies that long-range correlations between electrons have little influence on the electron energy distribution for PIE processes to high n states. In other words, the "decision" of the inner electron to be excited to a higher n state is made while the electron is still near the nucleus.

Although the experiment of Wehlitz *et al.* was only able to measure cross section

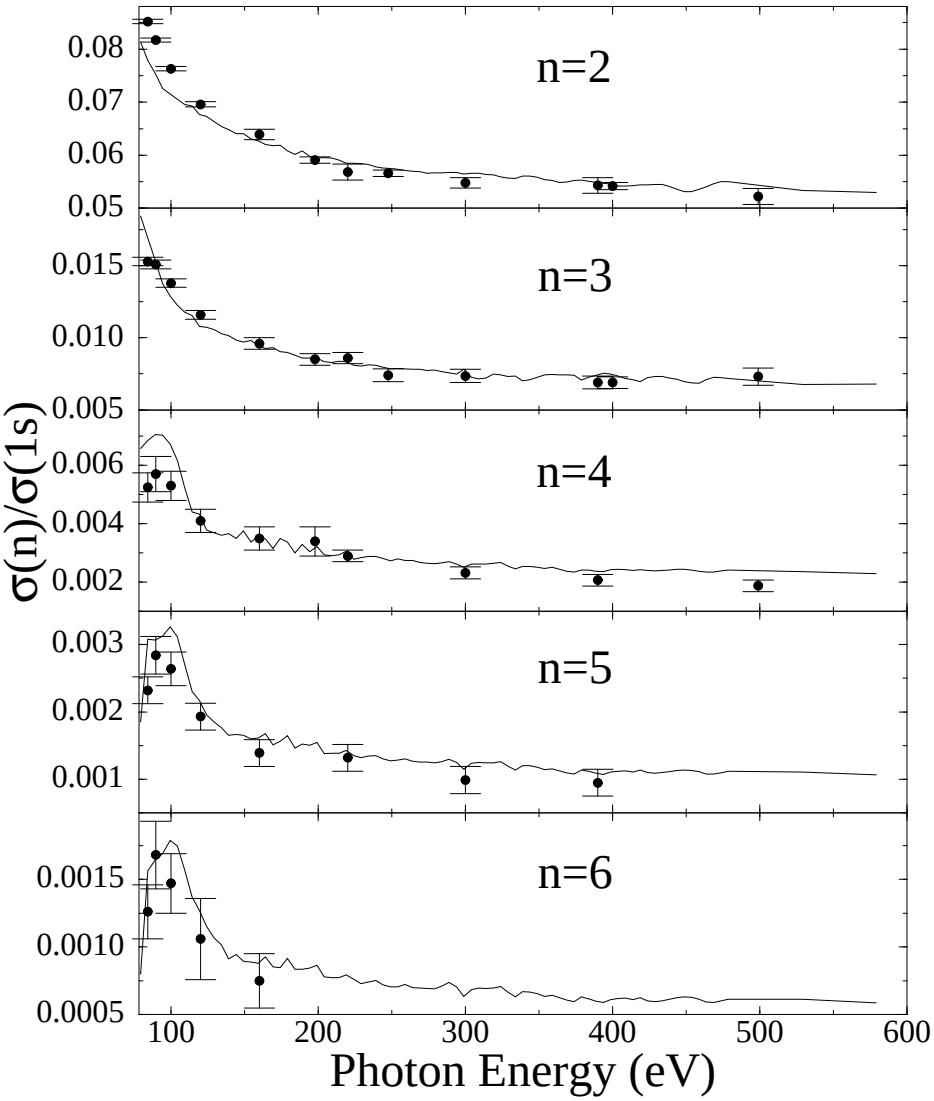

Figure 21. σ_n/σ_{1s} branching ratios of helium photoionization for n=2-6. The curves are our calculated eigenchannel R-matrix values, while the circles are the experimental values of Wehlitz *et al.* [114]. This figure is taken from Ref. [31].

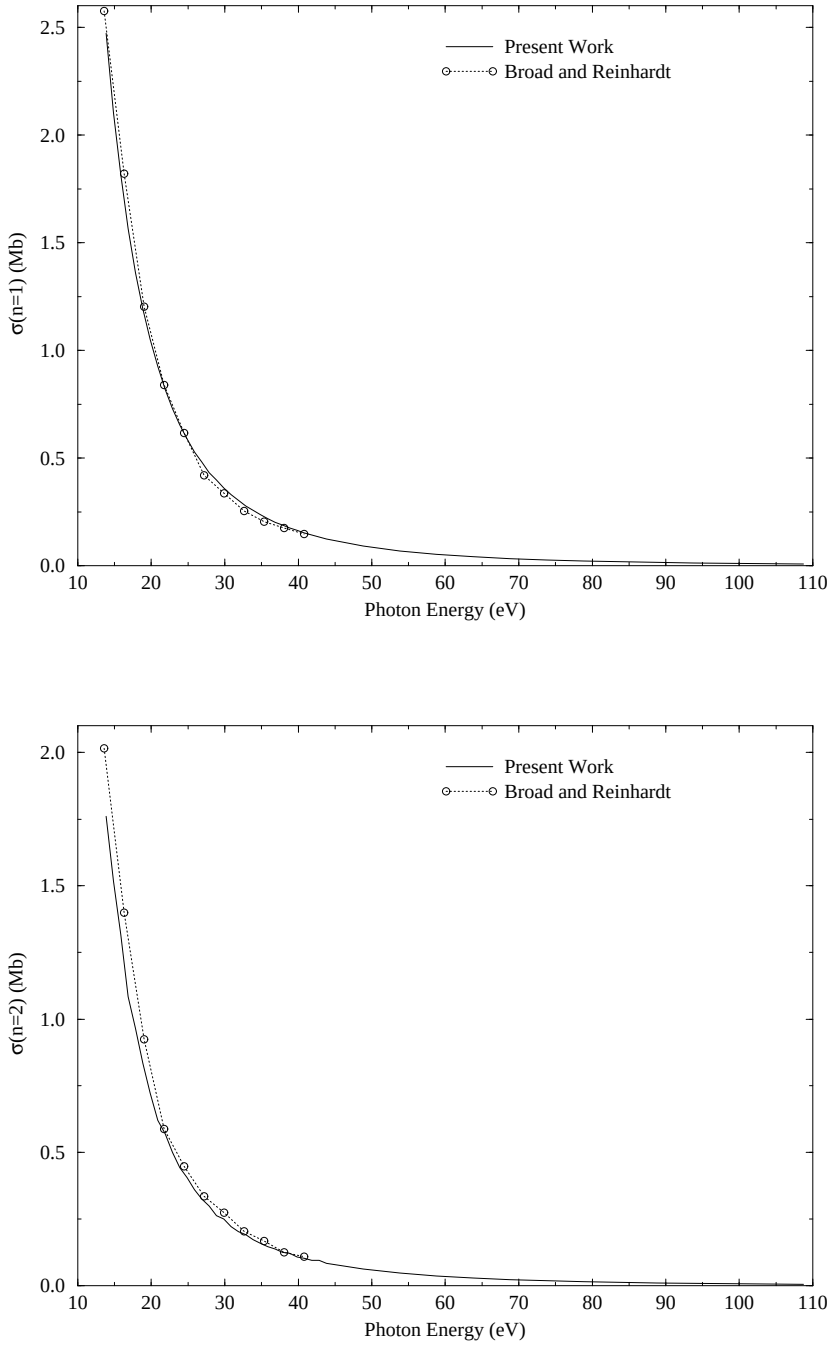

Figure 22. Comparison of our n=1 and n=2 H^- partial cross sections with extrapolated values taken from Fig. 1 of Ref. [52]. Note that unlike the case of photoejection-induced excitation for helium (Fig. 21), where the remaining electron is left in a $1s$ state roughly 90% of the time, the $n = 2$ partial cross section for H^- is comparable in magnitude to the $n = 1$ partial cross section.

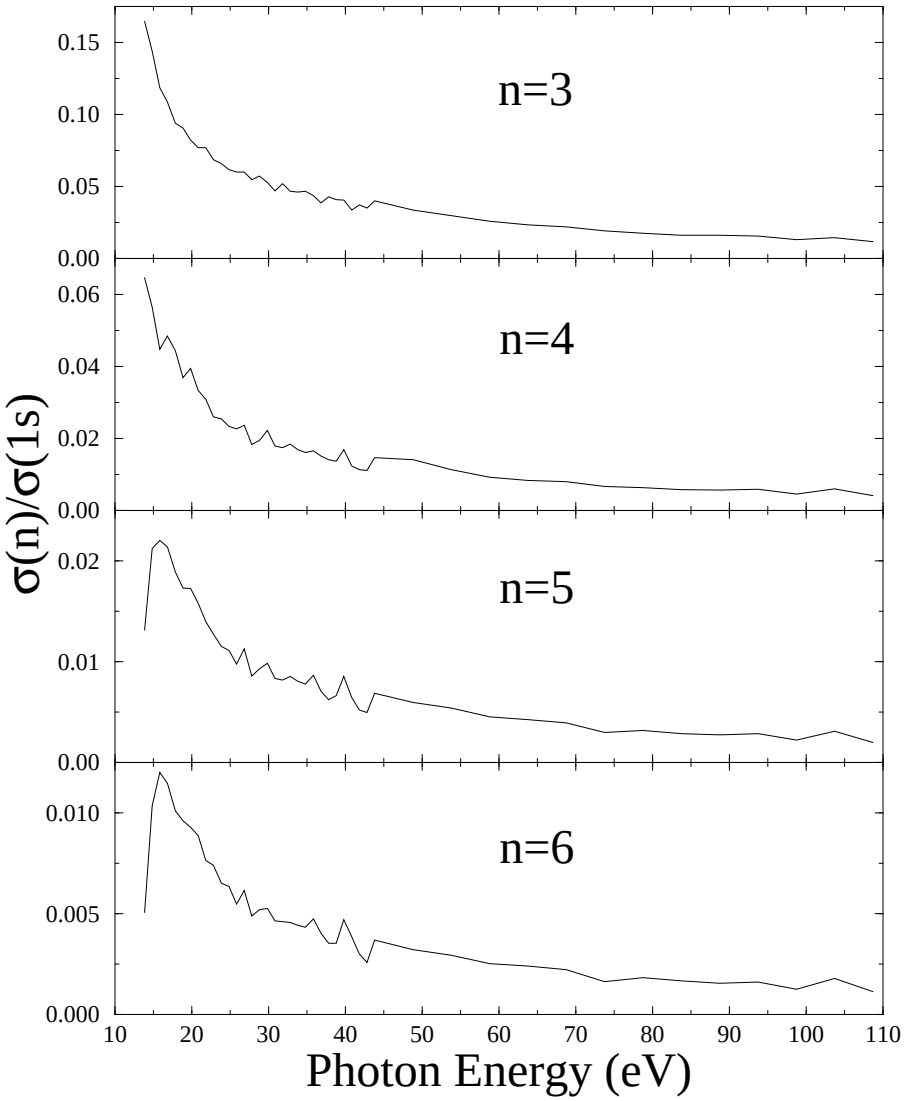

Figure 23. σ_n/σ_{1s} branching ratios of H^- photodetachment for n=3-6. The irregularities in the profiles for the first 30 eV above threshold are a reflection of the denser energy mesh used in this region.

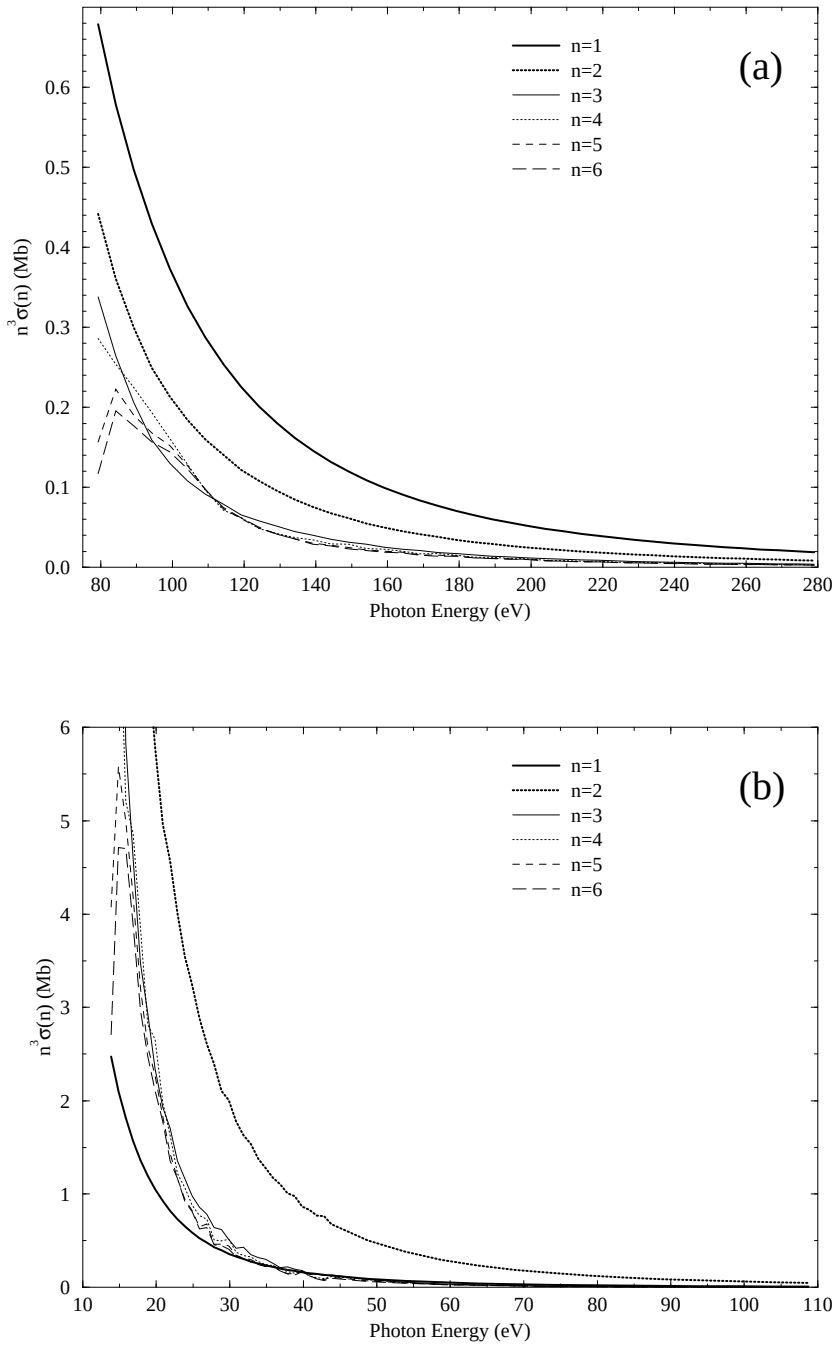

Figure 24. Comparison of our (a) He and (b) H^- partial cross sections with the $1/n^3$ scaling law, reflecting the properties of Rydberg electrons for large n values. This scaling law is observed to be valid for $n \geq 3$, and the agreement with the scaling law improves for larger photon energies.

ratios, they obtained absolute cross sections indirectly by using total cross section measurements from Samson *et al.* [165]. Our $n = 1$ absolute cross sections are within the error bars of Wehlitz *et al.* over the entire energy range calculated. At high (but nonrelativistic) energies, the decrease in the single ionization cross section of heliumlike systems is described by the power law $E^{-7/2}$ [101, 166]. Our calculated partial cross sections decrease at a slightly faster rate at high photon energies, indicating that the limiting $E^{-7/2}$ energy dependence has not yet been reached. Another noticeable feature in our partial cross section ratios is the presence of a peak value at energies of several eV above threshold for $n = 4 - 6$. This feature also appears in the experimental data for these n values. Peaks are observed in our $He^+(n)$ absolute cross sections for $n = 5$ and $n = 6$.

As seen in Figs. 23 and 24, partial cross sections calculated for H^- have features similar to those found in helium. Analogous to the case for calculating total photoejection cross sections, a reaction volume of roughly twice the radius used in our helium calculations is necessary to accurately describe H^- PIE. For the results presented here, our calculations were box averaged over five box sizes in the range 24-32 a.u. for photon energies of 14.35-65 eV, and over two box sizes of 24 and 26 a.u. for photon energies of 65-95 eV. A single box size of 24 a.u. was used to obtain the results for photon energies of 95-110 eV. The occurrence of irregular features in Fig. 23 only for the first 30 eV above threshold reflects the fact that we used a finer energy mesh over this range in comparison to calculations at higher energies. Unlike the case for helium, the $n = 2$ partial cross section for H^- is roughly two-thirds as large as the $n = 1$ cross section. This is mainly a consequence of the comparatively large overlap of the H^- ground state (see Fig. 15) with the $n = 2$ target eigenstates. As seen in Fig. 22, our $n = 1$ and $n = 2$ cross sections are consistent with the theoretical values extracted from the paper of Broad and Reinhardt [52]. Our H^- total photoabsorption cross sections also are found to agree well with the values presented by Broad and Reinhardt. Similar to the case for helium, peaks in the $n = 5$ and $n = 6$ branching ratios and the absolute partial

cross sections occur at photon energies of several eV above the double escape threshold.

One topic of interest is the relationship between partial cross sections for different values of n. Partial cross sections for helium are observed to scale as $1/n^3$ for $n \geq 3$ (see Fig. 24(a)), a reflection of the $1/n^3$ frequency scale of Rydberg electrons to be located near the nucleus. This $1/n^3$ scaling dependence improves for higher photon energies (greater than 100 eV above the double escape threshold). As seen in Fig. 24(b), the partial cross sections for H^- also obey a $1/n^3$ scaling law for $n \geq 3$.

Our present eigenchannel R-matrix approach does not allow for the exchange of angular momentum and energy between the electrons in the region outside of the reaction volume. Consequently, this approach can not hope to represent the details of a scattering process that is sensitive to long range forces other than a screened Columb potential. Our approximate treatment for the wavefunction outside of the reaction volume does not include the effect of long-range multipole interactions between the outer electron and the remaining fragment. The effect of including the long-range dipole interaction can be understood by adopting the form of this interaction as outlined by Gailitis and Damburg [167]. The dipole interaction mixes states with the same specified principal quantum number but different angular momentum values. Our method is capable of predicting the correct cross sections for PIE to the $n = 2$ state, but is not expected to give proper amplitudes of the individual Gailitis-Damburg eigenstates (eigenstates of the dipole operator with basis elements $|2s\epsilon p\rangle, |2p\epsilon s\rangle$, and $|2p\epsilon d\rangle$). A previous study [168] indicated that there are no major difficulties in including the long-range dipole interaction in an eigenchannel R-matrix approach.

In conclusion, we have applied our method to obtain accurate partial cross sections for helium and H^- photoabsorption. By adopting the frame transformation again, we were able to obtain helium partial cross sections which agreed well with experimental data for n values as large as $n = 6$. This result is surprising, as it indicates that long-range correlations are unimportant in determining the energy distribution of the remaining bound state electron

in PIE processes. These long-range correlations may be important in influencing the angular distributions of the remaining electron. Application of our approach to calculate angular distributions has not yet been undertaken. The accurate description of PIE processes has provided another demanding test of the ability of our eigenchannel R-matrix approach to describe processes for which electron-electron interactions are important. PIE and double escape are closely related processes. In fact, these processes are identical for the limiting case of PIE with $n \to \infty$. It is hoped that the results presented here will stimulate further progress in the description of PIE processes, and therefore provide a deeper understanding of the role that electron correlations play in atomic processes.

CHAPTER 5

CONCLUDING REMARKS

In this work, we have extended the eigenchannel R-matrix method to address two electron escape processes. Although double escape is a much more complicated process than single escape, R-matrix methods are still able to describe this process accurately (provided the excess escape energy of the two electrons is larger than a few eV). Our approach indicates that a proper description of electron-electron interactions is only required when the electrons are relatively close ($\approx$10-20 a.u.) to the nucleus in order to accurately treat double escape. This perturbative method represents a vast improvement over nonperturbative methods, which were the only theoretical treatments of double photoejection in the intermediate photon energy range at the time this study was initiated.

Although we have focussed primarily on double photoejection of helium and H^-, this work has much broader applications. Our approach should be applicable to any quantum mechanical three-body system with two escaping particles, provided the solution for the long-range interactions between any two particles is known, and the complicated short-range physics between the particles can be described numerically. Therefore, this work may have implications in several areas of physics, including chemical physics, condensed matter, nuclear physics, and perhaps even elementary particle physics. Although both the classical and quantum mechanical versions of the general three-body problem remain longstanding unsolved problems in the realm of physics, we have shown that with the use of efficient modern computers and some well chosen approximations, one can accurately describe quantum mechanically at least some of the details of two particle escape into the continuum.

We addressed two electron escape here for incident photons in the intermediate

energy range. This range is characterized by incoming energies high enough that the short-range physics is important in influencing the two electron escape process, yet low enough to render perturbative methods inadequate for the determination of double escape cross sections. By adopting a finite element basis set, we were able to address this energy range with an internally-consistent theoretical approach. Furthermore, most of the recent experimental data is consistent with our theoretical results. Applications of our approach to calculate partial cross sections of helium and H^- provided further insight into the nature of electron-electron interactions in electron escape. In particular, our results indicated that long-range correlations have little importance in determining the energy distribution of the remaining bound electron in single photoejection processes, at least in the intermediate photon energy range.

Much progress has been made in the past 5 or so years in describing two electron escape processes. These advances have been aided by rapid improvements in computational resources. On the experimental side, the availability of modern synchrotron light sources with both intense and high energy radiation beams, along with fast-gated coincidence electronics, has allowed new experiments to be performed with unprecedented precision. Following the recent theoretical and experimental progress in this field, attention has begun to turn to the description of more complicated systems. Anticipated double photoejection experiments for H^- and magnesium will provide additional tests of existing theoretical methods. An accurate description of magnesium double photoionization will be further complicated by the possibility of excitation of the core electrons at sufficiently high photon energies. Preliminary calculations [169] have already been performed to address electron correlations in the three-electron system of lithium. Double photoionization processes involving magnesium or lithium represent a further level of complexity for large enough incident photon energies, as the additional electron(s) in these systems can also be excited to higher states. A similarly challenging problem involves a proper theoretical description of H_2 double photoionization, a

process that also results in dissociation of the molecule. It remains to be seen how successfully discrete methods, of the type developed and extended in this dissertation, will be able to describe these phenomena of still greater complexity.

BIBLIOGRAPHY

[1] A.E. Roy, *Orbital Motion* (Adam Hilger, Bristol, 3rd edition, 1988).

[2] J.M.A. Danby, *Fundamental of Celestial Mechanics* (Willmann-Bell, Richmond, VA, 2nd edition, 1988).

[3] J.H. van Vleck, Philos. Mag. **44**, 842 (1922).

[4] M.C. Gutzwiller, *Chaos in Classical and Quantum Mechanics* (Springer, New York, 1990).

[5] D. Wintgen, K. Richter, and G. Tanner, CHAOS **2**, 19 (1992).

[6] E. Schrödinger, Ann. Physik **4**, 79 (1925).

[7] W. Heisenberg, Z. Physik **43**, 172 (1927).

[8] E.H. Kennard, Phys. Rev. **31**, 876 (1928).

[9] J.A. Wheeler, Phys. Rev. **52**, 1083 (1937).

[10] G. Arfken, *Mathematical Methods for Physicists* (Academic Press, New York, 2nd edition, 1970).

[11] B.H. Bransden and C.J. Joachain, *Physics of Atoms and Molecules* (John Wiley & Sons, New York, 1983).

[12] M. Born and J.R. Oppenheimer, Ann. Physik **84**, 457 (1927).

[13] G. Breit and E. Wigner, Phys. Rev. **49**, 519 (1936).

[14] J.A. Wheeler, Phys. Rev. **52**, 1107 (1937).

[15] W. Heisenberg, Z. Physik **120**, 513 (1942).

[16] E.P. Wigner, Phys. Rev. **70**, 15 and 606 (1946).

[17] L. Motz and J. Schwinger, Phys. Rev. **58**, 26 (1940).

[18] W. Kohn, Phys. Rev. **74**, 1763 (1948).

[19] D.R. Hartree, Proc. Camb. Phil. Soc. **24**, 89 (1928).

[20] J.C. Slater, Phys. Rev. **32**, 339 and 349 (1928).

[21] V. Fock, Z. Physik **61**, 126 (1930).

[22] E.A. Hylleraas, Z. Physik **54**, 347 (1929).

[23] M. Aymar, C.H. Greene, and E. Luc-Koenig, Rev. Mod. Phys. **68**, 1015 (1996).

[24] R.P. Madden and K.Codling, Phys. Rev. Lett. **10**, 516 (1963).

[25] T.A. Carlson, Phys. Rev., **156**, 142 (1967).

[26] R. Dörner, T. Vogt, V. Mergel, H. Khemliche, S. Kravis, C.L. Cocke, J. Ullrich, M. Unverzagt, L. Spielberger, M. Damrau, O. Jagutzki, I. Ali, B. Weaver, K. Ullmann, C.C. Hsu, M. Jung, E.P. Kanter, B. Sonntag, M.H. Prior, E. Rotenberg, J. Denlinger, T. Warwick, S.T. Manson, and H. Schmidt-Böcking, Phys. Rev. Lett. **76**, 2654 (1996).

[27] I. Bray and A.T. Stelbovics, Phys. Rev. Lett. **70**, 746 (1993).

[28] K.W. Meyer and C.H. Greene, Phys. Rev. A **50**, R3573 (1994).

[29] K.W. Meyer, C.H. Greene, and I. Bray, Phys. Rev. A **52**, 1334 (1996).

[30] K.W. Meyer, C.H. Greene, and B.D. Esry, Phys. Rev. Lett. **78**, 4902 (1997).

[31] K.W. Meyer, J.L. Bohn, C.H. Greene, and B.D. Esry, Phys. Rev. Lett. (submitted, 1997).

[32] J.S. Levinger, Phys. Rev. **90**, 11 (1953).

[33] M.Y. Amusia, J. Phys. B **8**, 1248 (1975).

[34] J.A.R. Samson, R.J. Bartlett, and Z.X. He, Phys. Rev. A **46**, 7277 (1992).

[35] J.M. Rost, Phys. Rev. A **53**, R640 (1996).

[36] S.L. Carter and H.P. Kelly, Phys. Rev. A **24**, 170 (1981).

[37] T. Ishihara, K. Hino, and J.H. McGuire, Phys. Rev. A **44**, R6980 (1991).

[38] A. Dalgarno and H. Sedeghpour, Phys. Rev. A **46**, R3591 (1992).

[39] K. Hino, T. Ishihara, F. Shimizu, N. Toshima, and J.H. Mcguire, Phys. Rev. A **48**, 1271 (1993).

[40] F.W. Byron and C.J. Joachain, Phys. Rev. **164**, 1 (1967).

[41] R.L. Brown, Phys. Rev. A **1**, 586 (1970).

[42] M. Brauner, J.S. Briggs and H. Klar, J. Phys. B **22**, 2265 (1989).

[43] F. Maulbetsch and J.S. Briggs, J. Phys. B **26**, 1679 (1993).

[44] J. Berakdar and J.S. Briggs, Phys. Rev. Lett. **72**, 3799 (1994).

[45] I. Bray and A.T. Stelbovics, Adv. At. Mol. Phys. **35**, 209 (1995).

[46] P.G. Burke, C.J. Noble, and Penny Scott, Proc. R. Soc. London Ser. A **410**, 289 (1987).

[47] I. Bray and A.T. Stelbovics, Phys. Rev. A **46**, 6995 (1992).

[48] K. Bartschat, E.T. Hudson, M.P. Scott, P.G. Burke, and V.M. Burke, J. Phys. B **29**, 115 (1996).

[49] J.Z. Tang, S. Watanabe, and M. Matsuzawa, Phys. Rev. A **46**, 2437 (1992).

[50] H. Friedrich, in *Theoretical Atomic Physics* (Springer-Verlag, Berlin, 1990).

[51] J. Callaway and D.H. Oza, Phys. Lett. **72A**, 207 (1979).

[52] J.T. Broad and W.P. Reinhardt, Phys. Rev. A **14**, 2159 (1976).

[53] D. Kato and S. Watanabe, Phys. Rev. Lett. **74**, 2443 (1995).

[54] I. Bray, I.E. McCarthy, J. Wigley, and A.T. Stelbovics, J. Phys. B **26**, L831 (1993).

[55] I. Bray and A.T. Stelbovics, Phys. Rev. A **48**, 4787 (1993); **49**, R2224 (1994).

[56] I. Bray, D.V. Fursa, and I.E. McCarthy, J. Phys. B **27**, L421 (1994); D.V. Fursa and I. Bray, Phys Rev. A **52**, 1279 (1995).

[57] I. Bray, Phys. Rev. A **49**, 1066 (1994).

[58] A. Kheifets and I. Bray, Phys. Rev. A **54**, R995 (1996).

[59] I. Bray, Phys. Rev. Lett. **78**, 4721 (1997).

[60] S. Watanabe, Y. Hosoda, and D. Kato, J. Phys. B **26**, L495 (1993).

[61] D. Kato and S. Watanabe, J. Phys. B **29**, L779 (1996).

[62] J.-Z. Tang and I. Shimamura, Phys. Rev. A **52**, R3413 (1995).

[63] U. Fano, Rep. Prog. Phys. **46**, 97 (1983).

[64] C.D. Lin, Phys. Rev. **25**, 76 (1982); **26**, 2305 (1982); **27**, 22 (1983).

[65] J.-Z. Tang, S. Watanabe, M. Matsuzawa, and C.D. Lin, Phys. Rev. Lett. **69**, 1633 (1992).

[66] J.C. Light and R.B. Walker, J. Chem. Phys. **65**, 4272 (1976).

[67] B. Christensen-Dalsgaard, Phys. Rev. A **29**, 2242 (1984).

[68] E.P. Wigner and L. Eisenbud, Phys. Rev. **72**, 29 (1947).

[69] F. Robicheaux, Phys. Rev. A **43**, 5946 (1991) (see Appendix); B.I. Schneider (unpublished).

[70] K. Bartschat and C.H. Greene, J. Phys. B **26**, L109 (1993).

[71] P.G. Burke, K.A. Berrington, and C.V. Sukumar, J. Phys. B **14** 289 (1981).

[72] M.P. Scott, T.T. Scholz, H.R.J. Walters, and P.G. Burke, J. Phys. B **22**, 3055 (1989).

[73] T.T. Scholz, H.R.J. Walters, P.G. Burke, and M.P. Scott, J. Phys. B **24**, 2097 (1991).

[74] T.T. Scholz, H.R.J. Walters, and P.G. Burke, J. Phys. B **23**, L467 (1990).

[75] M.B. Shah, D.S. Elliot, and H.B. Gilbody, J. Phys. B **20**, 3501 (1987).

[76] M.P. Scott, P.G. Burke, K. Bartschat, and I. Bray, J. Phys. B **30**, L309 (1997).

[77] P.G. Burke, V.M. Burke, and K.M. Dunseath, J. Phys. B **27**, 5341 (1994).

[78] K. Bartschat, E.T. Hudson, M.P. Scott, P.G. Burke, and V.M. Burke, J. Phys. B **29**, 2875 (1996).

[79] K. Bartschat, E.T. Hudson, M.P. Scott, P.G. Burke, and V.M. Burke, Phys. Rev. A **54**, R998 (1996).

[80] K. Bartschat, P.G. Burke, and M.P. Scott, J. Phys. B **29**, L769 (1996).

[81] P.J. Marchalant, K. Bartschat, K.A. Berrington, and S. Nakazaki, J. Phys. B **30**, L279 (1997).

[82] K. Bartschat and I. Bray, Phys. Rev. A **54**, R1002 (1996).

[83] T.W. Gorczyca and N.R. Badnell, J. Phys. B (submitted, 1997).

[84] E.P. Wigner, Phys. Rev. **73**, 1002 (1948).

[85] A.R.P. Rau, Comments At. Mol. Phys. **14**, 285 (1984).

[86] G.H. Wannier, Phys. Rev. **90**, 817 (1953).

[87] R. Peterkop, J. Phys. B **4**, 513 (1971).

[88] A.R.P. Rau, Phys. Rev. A **4**, 207 (1971).

[89] A. Temkin, Phys. Rev. Lett. **49**, 365 (1982).

[90] C.H. Greene and A.R.P. Rau, Phys. Rev. A **32**, 1352 (1985).

[91] A.R.P. Rau, J. Phys. B **9**, L283 (1976).

[92] S. Cvejanovič and F.H. Read, J. Phys. B **7**, 1841 (1974).

[93] R. Wehlitz, F. Heiser, O. Hemmers, B. Langer, A. Menzel, and U. Becker, Phys. Rev. Lett. **67**, 3764 (1991).

[94] J.W. McGowan and E.M. Clarke, Phys. Rev. **167**, 43 (1968).

[95] J.B. Donahue, P.A.M. Gram, M.V. Hynes, R.W. Hamm, C.A. Frost, H.C. Bryant, K.B. Butterfield, D.A. Clarke, and W.W. Smith, Phys. Rev. Lett. **48**, 1538 (1982).

[96] H. Kossmann, V. Schmidt, and T. Andersen, Phys. Rev. Lett. **60**, 1266 (1988).

[97] S. Watanabe, D. Kato, and M. Matsuzawa, Comments At. Mol. Phys. **33**, 95 (1996).

[98] D.H. Madison, I. Bray, and I.E. McCarthy, J. Phys. B **24**, 3861 (1991).

[99] K. Hino, T. Ishihara, F. Shimizu, N. Toshima, and J.H. McGuire, Phys. Rev. A **48**, 1271 (1993).

[100] R.H. Pratt, A. Ron, and H.K. Tseng, Rev. Mod. Phys. **45**, 273 (1973).

[101] A. Dalgarno and A.L. Stewart, Proc. Phys. Soc. London **76**, 49 (1960).

[102] H.R. Sadeghpour and A. Dalgarno, Phys. Rev. A **47**, R2458 (1993) (See comment in Ref. 15 of this paper).

[103] J.A.R. Samson, C.H. Greene, and R.J. Bartlett, Phys. Rev. Lett. **71**, 201 (1993).

[104] M.Ya. Amusia and A.I. Mikhailov, J. Phys. B **28**, 1723 (1995); Phys. Lett. A **199**, 209 (1995).

[105] L.R. Andersson and J. Burgdörfer, Phys. Rev. A **50**, R2810 (1994).

[106] T. Surić, K. Pisk, B.A. Logan, and R.H. Pratt, Phys. Rev. Lett. **73**, 790 (1994).

[107] M.A. Kornberg and J.E. Miraglia, Phys. Rev. A **53**, R3709 (1996).

[108] P.M. Bergstrom, K. Hino, and J. Macek, Phys. Rev. A **51**, 3044 (1995).

[109] R. Wehlitz, R. Hentges, G. Prümper, A. Farhat, T. Buslaps, N. Berrah, J.C. Levin, I.A. Sellin, and U. Becker, Phys. Rev. A **53**, 3720 (1996).

[110] L. Spielberger, O. Jagutzki, B. Krässig, U. Meyer, Kh. Khayyat, V. Mergel, Th. Tschentscher, Th. Buslaps, H. Bräuning, R. Dörner, T. Vogt, M. Achler, J. Ullrich, D.S. Gemmell, and H. Schmidt-Böcking, Phys. Rev. Lett. **76**, 4685 (1996).

[111] V. Schmidt, Rep. Prog. Phys. **55**, 1483 (1992).

[112] J.C. Levin, D.W. Lindle, N. Keller, R.D. Miller, Y. Azuma, N. Berrah Mansour, H.G. Berry, and I.A. Sellin, Phys. Rev. Lett. **67**, 968 (1991).

[113] L. Spielberger, O. Jagutzki, R. Doörner, J. Ullrich, U. Meyer, V. Mergel, M. Unverzagt, M. Damrau, T. Vogt, I. Ali, Kh. Khayyat, D. Bahr, H.G. Schmidt, R. Frahm, and H. Schmidt-Böcking, **74**, 4615 (1995).

[114] R. Wehlitz, I.A. Sellin, O. Hemmers, S.B. Whitfield, P. Glans, H. Wang, D.W. Lindle, B. Langer, N. Berrah, J. Viefhaus, and U. Becker, J. Phys. B **30**, L51 (1997).

[115] R. Wehlitz, B. Langer, N. Berrah, S.B. Whitfield, J. Viefhaus, and U. Becker, J. Phys. B **26**, L783 (1993).

[116] D. Proulx and R. Shakeshaft, Phys. Rev. A **48**, R875 (1993).

[117] M. Pont and R. Shakeshaft, J. Phys. B **28**, L571 (1995).

[118] F. Maulbetsch, M. Pont, J.S. Briggs, and R. Shakeshaft, J. Phys. B **28**, L341 (1995).

[119] M. Pont and R. Shakeshaft, Phys. Rev. A **51**, R2676 (1995).

[120] O. Schwarzkopf, B. Krässig, J. Elmiger, and V. Schmidt, Phys. Rev. Lett. **70**, 3008 (1993); O. Schwarzkopf, B. Krässig, V. Schmidt, F. Maulbetsch, and J.S. Briggs, J. Phys. B **27**, L347 (1994).

[121] Z.-J. Teng and R. Shakeshaft, Phys. Rev. A **49**, 3597 (1994).

[122] M.A. Kornberg and J.E. Miraglia, Phys. Rev. A **49**, 5120 (1994).

[123] J.A.R. Samson, E.-M. Lee, and Y. Chung, J. Electron Spectroscopy **66**, 75 (1993).

[124] J.A.R. Samson and G.C. Angel, Phys. Rev. A **42**, 5328 (1990).

[125] C.H. Greene and L. Kim, Phys. Rev. A **38**, 5953 (1988).

[126] F. Robicheaux, R. Wood, and C.H. Greene, Phys. Rev. A **49**, 1866 (1994).

[127] M. Gailitis, Zh. Eksp. Teor. Phys. **44**, 1974 (1963) [Sov. Phys. JETP **17**, 1328 (1963)].

[128] M.J. Seaton, Rep. Prog. Phys. **46**, 167 (1983).

[129] V. Schmidt, N. Sander, H. Kuntzmüller, P. Dhez, F. Wuilleumier, and E. Källne, Phys. Rev. A **13**, 1748 (1976).

[130] G.R. Wight and M.J. Van der Wiel, J. Phys. B **9**, 1319 (1976).

[131] D.M.P. Holland, K. Codling, J.B. West, and G.V. Marr, J. Phys. B **12**, 2465 (1979).

[132] P. Lablanquie, K. Ito, P. Morin, I. Nenner, and J.H.D. Eland, Z. Phys. D **16**, 77 (1990).

[133] R.J. Bartlett, P. Walsch, Z.X. He, Y. Chung, E-M. Lee, and J.A.R. Samson, Phys. Rev. A **46**, 5574 (1992).

[134] C. Pan and H.P. Kelly, J. Phys. B **28**, 5001 (1995).

[135] A. Temkin, Phys. Rev. **126**, 130 (1962).

[136] R. Poet, J. Phys. B **11**, 3081 (1978).

[137] R. Poet, J. Phys. B **13**, 2995 (1980).

[138] J. Callaway and D.H. Oza, Phys. Rev. A **29**, 2416 (1984)

[139] R. Poet, J. Phys. B **14**, 91 (1981).

[140] D.H. Oza and J. Callaway, Phys. Rev. A **27**, 2840 (1983).

[141] M. Le Dourneuf, J.M. Launay, and P.G. Burke, J. Phys. B **23**, L559 (1990).

[142] I. Bray and A.T. Stelbovics, Phys. Rev. Lett. **69**, 53 (1992).

[143] D.A. Konovalov and I.E. McCarthy, J. Phys. B **27**, L407 (1994).

[144] I. Bray and A.T. Stelbovics, Atomic Data Nucl. Data Tables **58**, 67 (1994).

[145] H.R. Sadeghpour, C.H. Greene, and M. Cavagnero, Phys. Rev. A **45**, 1587 (1992).

[146] C.H. Greene and C. Jungen, Adv. At. Mol. Phys. **21**, 51 (1985).

[147] D.F. Gallaher, J. Phys. B **7**, 362 (1974).

[148] U. Fano, J. Opt. Soc. Am. **65**, 979 (1975); U. Fano, Phys. Rev. A **24**, 619 (1981).

[149] D.A. Harmin, Phys. Rev. A **26**,2656 (1982).

[150] M. Braun, W. Schweizer, and H. Herold, Phys. Rev. A **48**, 1916 (1993).

[151] J. Ackermann and J. Shertzer, Phys. Rev. A **54**, 365 (1996).

[152] J. Shertzer and J. Botero, Phys. Rev. A **49**, 3673 (1994).

[153] H.W. van der Hart, J. Phys. B **30**, 453 (1997).

[154] J.P. Burke, C.H. Greene, and B.D. Esry, Phys. Rev. A **54**, 3225 (1996).

[155] M.T. Jones and M.L. Patrick, Applied Numerical Mathematics **12**, 377 (1993).

[156] W.H. Press, B.P. Flannery, S.A. Teukolshy, and W.T. Vettering, *Numerical Recipes (FORTRAN)* (Cambridge University Press, Cambridge, 1989).

[157] E. Anderson, Z. Bai, C. Bischof, J. Demmel, J. Dongarra, J. Du Croz, A. Greenbaum, S. Hammarling, A. McKenney, S. Ostrouchov, and D. Sorensen, *LAPACK Users Guide* (SIAM, Philadelphia, 1992).

[158] J.C. Levin, G.B. Armen, and I.A. Sellin, Phys. Rev. Lett. **76**, 1220 (1996).

[159] A.G. Abrashkevich and M. Shapiro, Phys. Rev. A **50**, 1205 (1994), and references within.

[160] J.F. McCann and D.S. Crothers, J. Phys. B **19**, L399 (1986).

[161] G.W.F. Drake, in *Atomic, Molecular, and Optical Physics Handbook*, edited by G.W.F. Drake and N.E. Hedgecock (AIP, New York, 1996).

[162] J.A.R. Samson (to be published) (1997).

[163] H.R. Sadeghpour (private communication).

[164] R.C. Weast, in *Handbook of Chemistry and Physics* (1st student edition), edited by R.C. Weast (CRC Press, Inc., Boca Raton, Fl,1987).

[165] J.A.R. Samson, Z.X. He, L. Yin, and G.N. Haddad, J. Phys. B **27**, 887 (1994).

[166] T. Aberg, Phys. Rev. A **2**, 1726 (1970).

[167] M. Gailitis and R. Damburg, Proc. Phys. Soc. London **82**, 192 (1963).

[168] H.R. Sadeghpour and M. Cavagnero, J. Phys. B **26**, L271 (1993).

[169] X. Yang, C.G. Bao, and C.D. Lin, Phys. Rev. A **53**, 3934 (1996).

[170] C. Bloch, Nucl. Phys. **4**, 503 (1957).

[171] R.N. Zare, *Angular Momentum* (John Wiley and Sons, New York, 1988).

APPENDIX A

EQUIVALENCE OF DIPOLE OPERATOR FORMS IN A FINITE VOLUME

In an effort to understand the nature of the discrepancy between calculations using various forms of the dipole operator, we thoroughly explored the assumptions which were made in transforming from one form of the cross section to another. For example, the transformations given in Eqs. 14 and 15 of Chapter 2 have assumed that the Hamiltonian $\hat{H}$ is Hermitian. However, this is generally not true if the Hilbert space is restricted to a finite volume. This observation will now be illustrated with a simple example.

Consider the finite volume example of a one-dimensional square well. Given the matrix element $\langle\psi_2|\hat{x}|\psi_1\rangle$ which appears in the length form of the cross section, and choosing a closed (zero at outer boundary) wavefunction $\psi_1 = \sqrt{2/\pi}\sin(x)$ and an open (nonzero at outer boundary) wavefunction $\psi_2 = \sqrt{2/\pi}\sin(x/2)$ (see Fig. 25), the matrix element $\langle\psi_2|\hat{x}|\psi_1\rangle$ evaluates to -32/9π+8/3. According to the relation given by Eq. 14 (substituting $\hat{p}$ with its differential operator form $-i\hbar\frac{d}{dx}$ and using atomic units),

$$\langle\psi_2|\hat{x}|\psi_1\rangle \stackrel{?}{=} \frac{\langle\psi_2|\frac{d}{dx}|\psi_1\rangle}{E_2 - E_1}. \tag{56}$$

However, when the expression on the right hand side of this equation is evaluated, one obtains the value -32/9π, whereas the matrix element on the left hand side has the value -32/9π+8/3. We will show that the proper relationship between the length and velocity forms of the dipole operator is given by

$$\langle\psi_2|\hat{x}|\psi_1\rangle = \frac{\langle\psi_2|\frac{d}{dx}|\psi_1\rangle}{E_2 - E_1} + \frac{[\psi_2\psi_1 + \psi_2\hat{x}\frac{d\psi_1}{dx} - \frac{d\psi_2}{dx}\hat{x}\psi_1]|_{x_0}}{2(E_2 - E_1)}. \tag{57}$$

The only nonzero term in the second expression on the right hand side is the term involving the derivative of ψ_1, which evaluates to 8/3. For this simple example, the transformation

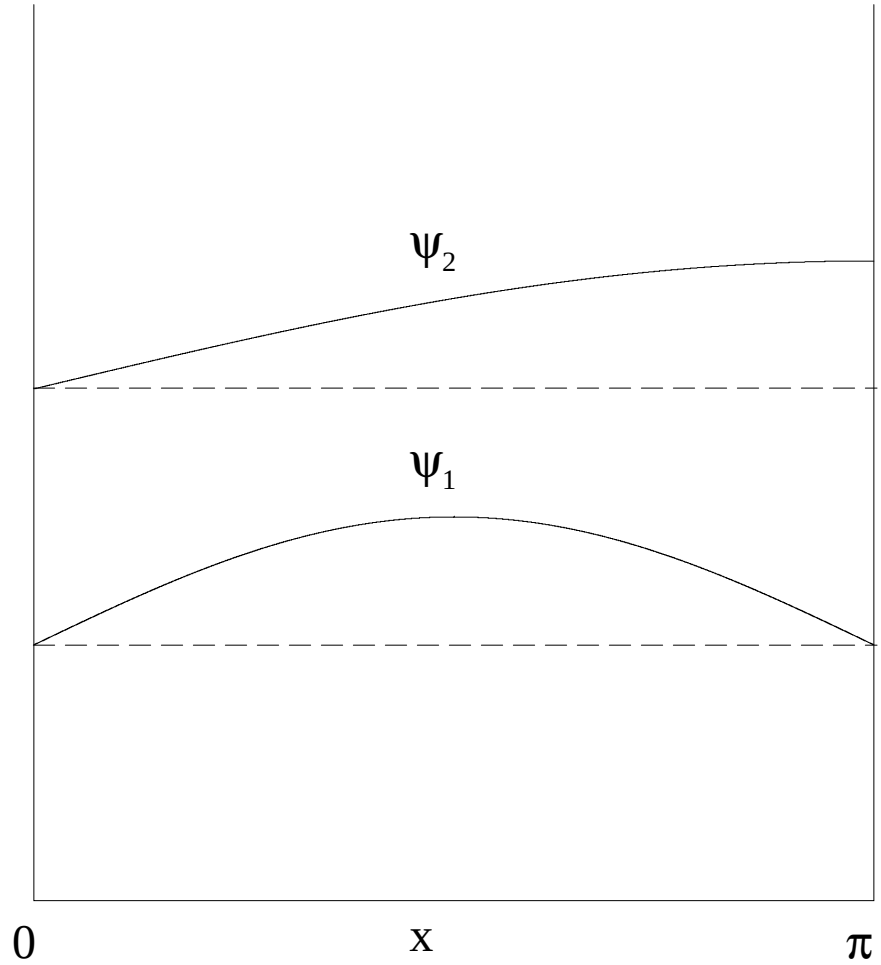

Figure 25. Consider the transformation of the dipole matrix element from length to velocity for wavefunctions confined to a finite volume. Let $\psi_1 = \sqrt{2/\pi}\sin(x)$ represent a closed wavefunction and $\psi_2 = \sqrt{2/\pi}\sin(x/2)$ represent an open wavefunction. For this simple case, the Hamiltonian is not Hermitian, since unlike the case for an infinite Hilbert space, the surface term (due to the nonzero derivative of ψ_1 and the nonzero value of ψ_2 on the outer boundary) no longer vanishes. Therefore, an additional term must be added in transforming from one dipole form to another for a finite volume Hilbert space.

given by Eq. 56 is not correct; the additional term on the right hand side of Eq. 57 must be added in order for the transformation to be valid.

As shown in the previous example, the Hamiltonian $\hat{H}$ is generally not Hermitian. We can however introduce an operator $\hat{\Gamma}$ which is Hermitian in a finite volume by adding an operator to the Hamiltonian; that is,

$$\hat{\Gamma} \equiv \hat{H} + \hat{L} \tag{58}$$

is Hermitian, where

$$\hat{L} \equiv \frac{1}{2r}\delta(r - r_0)\frac{\partial}{\partial r}r \tag{59}$$

is the Bloch operator [23, 170] in three dimensions (in this notation, the delta function effectively reduces the dimension of integration by one, leading to a "surface" term; the general integral form for the Bloch operator is given by $\frac{1}{2}\int_S \psi_2^* \frac{\partial}{\partial n}\psi_1 dS$, where $\partial/\partial n$ is the normal derivative). Therefore,

$$\hat{H}^\dagger = \hat{H} + (\hat{L} - \hat{L}^\dagger). \tag{60}$$

Using this identity to perform the transformation in Eq. 14, we obtain the expression

$$\langle\psi_2|\hat{\vec{r}}\,|\psi_1\rangle = \frac{i}{E_2 - E_1}\langle\psi_2|\hat{\vec{p}}\,|\psi_1\rangle + \frac{1}{E_2 - E_1}\langle\psi_2|(\hat{L} - \hat{L^\dagger})\hat{\vec{r}}\,|\psi_1\rangle. \tag{61}$$

Note that the term involving the Bloch operator vanishes if the wavefunction and first derivative of ψ_1 vanish on the surface, which are the boundary conditions normally adopted for describing a bound state wavefunction in an infinite Hilbert space. Eq. 57 was derived by simply using the form of Eq. 61 with the one dimensional Bloch operator $\frac{1}{2}\delta(x - x_0)\frac{d}{dx}$.

The transformations between the length, velocity, and acceleration dipole operators in one dimension can be summarized as follows:

$$d_L = d_V + C_{LV}, \quad d_V = d_A + C_{VA}, \tag{62}$$

where

$$d_L \equiv \langle\psi_2|\hat{x}|\psi_1\rangle, \tag{63}$$

$$d_V \equiv \frac{\langle\psi_2|-\frac{d}{dx}|\psi_1\rangle}{E_2-E_1} = \frac{1}{i}\frac{\langle\psi_2|\hat{p}|\psi_1\rangle}{(E_2-E_1)}, \tag{64}$$

$$d_A \equiv \frac{\langle\psi_2|\frac{dV}{dx}|\psi_1\rangle}{(E_2-E_1)^2}, \tag{65}$$

$$C_{LV} \equiv \frac{\left[\psi_2\psi_1 + \psi_2 x\frac{d\psi_1}{dx} - \frac{d\psi_2}{dx}x\psi_1\right]|_{x_0}}{2(E_2-E_1)}, \tag{66}$$

and

$$C_{VA} \equiv \frac{\left[\frac{d\psi_1}{dx}\frac{d\psi_2}{dx} - 2(V-E_1)\psi_1\psi_2\right]|_{x_0}}{2(E_2-E_1)^2}. \tag{67}$$

Schrödinger's equation was used to eliminate a term in the second derivative of ψ_1 in the expression for C_{VA}. Note that the "surface" term connecting the velocity and acceleration forms may be nonzero even if both wavefunctions vanish on the outer boundary.

We now develop the three-dimensional transformations and apply them to the test case of photoionization of hydrogen. In three dimensions, the dipole matrix is given by $\langle\psi_2|\hat{\epsilon}\cdot\hat{r}|\psi_1\rangle$. In the following derivation, we will make two assumptions: first, the light is taken to be polarized in the z-direction ($\hat{\epsilon} = \hat{r}\cos\theta - \hat{\theta}\sin\theta$), and second, the potential is assumed to be a function of the radial coordinate only. For photoionization of hydrogen, the ground state ψ_1 is in an s state ($\psi_1(\vec{r}) = \varphi_1(r)Y_{00}(\theta,\phi)$), which simplifies the form of the transformations; however, we derive the more general case here. The commutator of interest is now $[H, r\cos\theta]$. The resulting angular integral can be factored out of the dipole matrix, leaving a remaining integral in r. For convenience, we will introduce the scaled wavefunction $u(r)$, defined by $\varphi(r) = u(r)/r$. Note that when the three-dimensional form of the Bloch operator (Eq. 59) is evaluated in a matrix element involving the full wavefunctions, the matrix element is equivalent to the one formed by replacing the full wavefunctions by scaled wavefunctions and the three-dimensional form of the Bloch operator by the one-dimensional form. Applying the same approach used to obtain the one-dimensional results, the length form of the dipole matrix is

$$d_L \equiv \langle\psi_2|\hat{\epsilon}\cdot\hat{\vec{r}}|\psi_1\rangle = d_{LRAD}F_{ANG1} \tag{68}$$

where

$$d_{LRAD} \equiv \langle \varphi_2 | \hat{r} | \varphi_1 \rangle \tag{69}$$

and

$$F_{ANG1} \equiv \langle Y_{l_2,m} | \cos\theta | Y_{l_1,m} \rangle. \tag{70}$$

The relationship between length and velocity forms is given by

$$d_L = d_{VRAD}^{l_1 \neq 0} F_{ANG2} + [d_{VRAD} + C_{LV}] F_{ANG1}, \tag{71}$$

where

$$d_{VRAD}^{l_1 \neq 0} \equiv \frac{\langle \varphi_2 | \frac{1}{r} | \varphi_1 \rangle}{(E_2 - E_1)}, \tag{72}$$

$$F_{ANG2} \equiv \langle Y_{l_2,m} | \sin\theta \frac{\partial}{\partial\theta} | Y_{l_1,m} \rangle, \tag{73}$$

$$d_{VRAD} \equiv \frac{\langle \varphi_2 | - \frac{d}{dr} | \varphi_1 \rangle}{(E_2 - E_1)}, \tag{74}$$

and

$$C_{LV} \equiv \frac{\left[u_2 u_1 + u_2 r \frac{du_1}{dr} - \frac{du_2}{dr} r u_1 \right] |_{r=r_0}}{2(E_2 - E_1)}. \tag{75}$$

The superscript '$l_1 \neq 0$' denotes that the angular integral multiplying this term may only be nonzero if l_1 is nonzero. Note that for the case $l_1 = 0$, the radial correction form expressed in terms of the scaled wavefunctions is identical to the form for the one-dimensional case. The additional $l_1 \neq 0$ term arises from the additional component in the z-component of the angular momentum. Since the general form of the momentum is $\vec{p} = \hat{r}\frac{\partial}{\partial r} + \hat{\theta}\frac{1}{r}\frac{\partial}{\partial\theta} + \hat{\phi}\frac{1}{r\sin\theta}\frac{\partial}{\partial\phi}$, when dotted into the polarization vector, p_z will have a term involving the derivative with respect to θ, which can contribute for $l_1 \neq 0$. The transformation between the length and acceleration form is given by

$$d_L = [d_{ARAD} + C_{LV} + C_{VA}] F_{ANG1} + C_{VA}^{l_1 \neq 0} F_{ANG2}, \tag{76}$$

where

$$d_{ARAD} \equiv \frac{\langle \varphi_2 | \frac{dV}{dr} | \varphi_1 \rangle}{(E_2 - E_1)^2}, \tag{77}$$

$$C_{VA} \equiv \frac{\left[-\left(\frac{1}{r^2}\right) u_2 u_1 + \left(\frac{1}{r}\right) u_2 \frac{du_1}{dr} - u_2 \frac{d^2 u_1}{dr^2} - \left(\frac{1}{r}\right) \frac{du_2}{dr} u_1 + \frac{du_2}{dr} \frac{du_1}{dr}\right] |_{r=r_0}}{2(E_2 - E_1)^2}, \tag{78}$$

and

$$C_{VA}^{l_1 \neq 0} \equiv \frac{\left[-\left(\frac{1}{r^2}\right) u_2 u_1 - \left(\frac{1}{r}\right) \frac{du_2}{dr} u_1 + \left(\frac{1}{r}\right) u_2 \frac{du_1}{dr}\right] |_{r=r_0}}{2(E_2 - E_1)^2}. \tag{79}$$

Note that the form of C_{VA} is no longer the same as for the one-dimensional case, due to the complications with the momentum operator operating on a scaled wavefunction. The expression d^2u_1/dr^2 appearing in this term can be replaced by $2[V(r) - E_1 + (l(l+1))/2r^2]u_1$ using the Schrödinger equation.

We applied the above equations for the case of photoionization of the ground state of hydrogen. For hydrogen, the potential is given by $V(r) = -1/r$, so dV/dr in the expression d_{ARAD} is replaced by $1/r^2$. For small enough box sizes ($\approx$10 a.u.), the need for correction terms to obtain equivalence of the different forms of the cross section was quite apparent. Additional numerical tests were performed for the case $l_1 = 0$ to verify that all of the terms in Eqs. 75 and 78 are indeed correct. For our study of hydrogen photoionization, we found that the correction terms decreased roughly exponentially with increasing box size, reflecting the exponential decay of our ground state wavefunction near the edge of the box.

This analysis was eventually extended to the case of helium double photoionization. For this case, the Bloch operator becomes the sum of two operators of the form given in Eq. 59, one for each of the independent particle radial coordinates. The equations for the two-electron system are very similar to the one-electron equations given above, so will not be included here. One of the assumptions made in deriving the above equations was that the potential was a central potential. However, for the case of helium there is additional angular dependence in the $1/r_{12}$ term. As explained in Section 2.1, this term does not contribute to the correction terms between various dipole forms. The correction terms were included in our helium double photoionization computer code, but no significant difference in our cross section values were observed in comparison to our original values. Nonetheless, it is

informative to understand the assumptions made in transforming from one dipole form to another.

APPENDIX B

DETAILS OF OUR FINITE ELEMENT IMPLEMENTATION

In implementing our finite element approach, we had to overcome many difficulties encountered with imposing the antisymmetrization operator $\mathcal{A}$, as it appears in Eqs. 40 and 41. Also, since our approach differs from the approach outlined in Ref. [152], we will discuss a few of the details of our implementation. In applying the antisymmetrization operator, the general form of our spatial two-electron wavefunction is given by

$$\begin{aligned} \psi(\vec{r}_1,\vec{r}_2) &= \frac{1}{\sqrt{2(1+\delta_{n_1 n_2}\delta_{l_1 l_2})}} \\ &\quad [g_{l_1 l_2}(r_1,r_2)\mathcal{Y}^{LM}_{l_1 l_2}(\hat{r}_1,\hat{r}_2) + (-1)^S g_{l_1 l_2}(r_2,r_1)\mathcal{Y}^{LM}_{l_1 l_2}(\hat{r}_2,\hat{r}_1)]. \end{aligned} \tag{80}$$

We also require that the spatial permutation operator $P_{12}^{spatial}$ acting on the wavefunction satisfies the following relation:

$$P_{12}^{spatial}|\psi\rangle = (-1)^S|\psi\rangle. \tag{81}$$

In the applications considered in this work, we only consider singlet states (S=0), for which case the spacial wavefunction is symmetric. Using the identity [171]

$$\mathcal{Y}^{LM}_{l_1 l_2}(\hat{r}_2,\hat{r}_1) = (-1)^{l_1+l_2+L}\mathcal{Y}^{LM}_{l_2 l_1}(\hat{r}_1,\hat{r}_2), \tag{82}$$

for the ground state of helium ($L = S = 0$, which implies $l_1 = l_2$), the coupled spherical harmonic can be factored out of Eq. 81. Comparison of Eqs. 81 and 81 then implies $g_{l_1 l_2}(r_1,r_2) = g_{l_1 l_2}(r_2,r_1)$. That is, for the ground state of helium, antisymmetry of the total wavefunction requires that the two-electron radial wavefunction is symmetric about the line $r_1 = r_2$; similarly, for triplet $L = 0$ states, the two-electron radial wavefunction is antisymmetric about the line $r_1 = r_2$.

As a consequence of the conditions imposed by the antisymmetry operator for the ground state of helium, it is sufficient to solve the Schrödinger equation in the half-plane $r_1 \geq r_2$ or $r_1 \leq r_2$. This is the approach adopted in Ref. [152]. By imposing the boundary condition along the line $r_1 = r_2$ of a zero derivative of the radial wavefunction in the direction perpendicular to this line, singlet wavefunctions are completely determined by solving in the half-plane. Similarly, triplet states are obtained by solving the Schrödinger equation in the half-plane with the boundary conditions that the wavefunction vanishes along the line $r_1 = r_2$. Although Shertzer and Botero use a finite element grid of rectangular sectors, they impose these additional boundary conditions in those sectors where the points $r_1 = r_2$ are located. A more straightforward approach would be to directly impose boundary conditions along the line $r_1 = r_2$ using a finite element grid of triangular sectors; however, one would then have to deal with the complications of using triangular sectors.

To determine the ground state wavefunction in our implementation, we solve the Schrödinger equation directly over both regions $r_1 \geq r_2$ and $r_1 \leq r_2$ without imposing any boundary conditions along the line $r_1 = r_2$. The only boundary conditions imposed are that the wavefunction vanish along the lines $r_1 = 0$, $r_2 = 0$, $r_1 = r_0$, and $r_2 = r_0$, where r_0 is the radius of our reaction volume. A Lanczos iterative algorithm is used to partially diagonalize our Hamiltonian and obtain the first few lowest energy eigenvalues. The corresponding eigenstates include both singlet and triplet states. Our method of solving for the ground state in the full $r_1 - r_2$ reaction volume space without imposing boundary conditions along the line $r_1 = r_2$ is not as computationally efficient as the method used in Ref. [152]. However, since the determination of our initial state required very little computational time in comparison to the rest of our calculation, we chose to adopt a method based on simplicity of implementation rather than numerical efficiency.

For the $L = 1$ final state wavefunction, we no longer have $l_1 = l_2$, so the coupled spherical harmonics cannot be factored out of Eq. 81. However, again using the identity

given in Eq. 82 and comparing the resulting expressions in Eqs. 81 and 81, we obtain the condition $g_{l_1 l_2}(r_2, r_1) = g_{l_2 l_1}(r_1, r_2)$. So, for example, if we determined the radial wavefunction $g_{01}(r_2, r_1)$ in the region $r_1 \geq r_2$, then we have simultaneously determined the radial wavefunction $g_{10}(r_1, r_2)$ in the region $r_1 \geq r_2$. In the method implemented in Ref. [152], separate matrices are formed for each ordering of angular configuration (*e.g.*, one matrix for $|l_1 = 0, l_2 = 1\rangle$ and one matrix for $|l_1 = 1, l_2 = 0\rangle$), but only over half-plane regions. For example, the matrix for the $|01\rangle$ angular configuration might be formed in the region $r_1 \leq r_2$, while the $|10\rangle$ angular configuration would be formed in the corresponding region $r_1 \geq r_2$. In our implementation, a single matrix contains the information for the wavefunctions $g_{l_1 l_2}(r_2, r_1)$ and $g_{l_2 l_1}(r_1, r_2)$ over the entire $r_1 - r_2$ region inside our reaction volume.

In addition to differences in our approach to antisymmetrization, the numbering scheme for the ordering of our nodes was originally different than the approach adopted in Ref. [152]. The term 'nodes' refers to the points within each sector where the boundary conditions of our Hermite interpolating polynomials (see Fig. 14) are enforced; in our case, there are nine nodes for each sector; four at the corners of each sector, four at the midpoints of the sides of each sector, and one at the center of each sector. Our original numbering scheme resulted in matrices with large bandwidths, which were not suitable for factorization methods. We eventually adopted the numbering scheme of Shertzer and Botero, and so were able to make our computer code significantly more efficient.

Another important detail in our manipulation of finite element matrices was the adoption of a sparse symmetric storage scheme. For the final state wavefunction, the Hamiltonian is not Hermitian (see Appendix A), so is represented by a nonsymmetrical matrix. However, the operator $\hat{\Gamma}$ introduced in Eq. 58 of Appendix A is Hermitian. To avoid nonsymmetric matrices, we always store the sum of the Hamiltonian and Bloch operators, which is symmetric, rather than the nonsymmetric Hamiltonian and Bloch matrices separately.